Univerzita Karlova v Praze
Matematicko-fyzikální fakulta

DIPLOMOVÁ PRÁCE

Ondřej Tkáč

Fotodisociace molekul ve volných nanočásticích

Katedra chemické fyziky a optiky

Vedoucí diplomové práce: Doc. RNDr. Juraj Dian, CSc.

Studijní program: Biofyzika a chemická fyzika, teorie molekulárních systémů

2010

Acknowledgments

Primarily, I would like to thank my supervisor Michal Fárník for providing me with the opportunity to write a diploma thesis at J. Heyrovský Institute of Physical Chemistry, for his very kind and stimulative guiding, and his many of suggestions which helped me to improve my thesis. In addition, I am grateful to him for the corrections of my English and provided pictures. I am also obliged to him for ensuring my research stay at the Univerzity of Georg August in Göttingen, and my participation in the Symposium on Atomic, Cluster and Surface Physics 2010. Both helped me to gain an insight into the scientific community, stimulate my ambition, and let me practically apply my skills acquired during my studies at MFF UK.

Viktoriya Poterya taught me the principles of measurement and helped me with data processing, and I really appreciate it.

Additional acknowledgment belongs to my formal supervisor Juraj Dian for his kind guidance and to my colleagues – Juraj Fedor and Andriy Pysanenko - for various pieces of advice and support, and to Jan kotek for his help with hydroiodic acid preparation.

I would also like to thank Jack Morgan for carefully reading my thesis and for improving my English, especially in the use of articles and commas.

Last, but not least, I give thanks to my family for financial and moral support during all the studies, and to my girlfriend for creation of a comfortable environment for writing.

This Thesis was also supported by the student´s grant, VACUUM Prague.

Prohlašuji, že jsem svou diplomovou práci napsal samostatně a výhradně s použitím citovaných pramenů. Souhlasím se zapůjčováním práce a jejím zveřejňováním.

V Praze dne: 14. 4. 2010 Ondřej Tkáč

Content

Název práce: Fotodisociace molekul ve volných nanočásticích
Autor: Ondřej Tkáč
Katedra (Ústav): Katedra chemické fyziky a optiky
Vedoucí diplomové práce: Doc. RNDr. Juraj Dian, CSc.
E-mail vedoucího: Juraj.Dian@mff.cuni.cz
Konzultant: Mgr. Michal Fárník, Ph.D., AV ČR, Ústav fyzikální chemie Jaroslava Heyrovského, oddělení fotochemie, spektroskopie a iontové chemie, Dolejškova 3, Praha 8

Abstrakt: Na aparatuře s molekulovými paprsky bylo provedeno několik experimentů s různými klastry. (1) Byly změřeny rychlosti klastrů vzácných plynů a vody za různých expanzních podmínek, abychom se učili o supersonické expanzi a procesech tvorby klastrů. (2) Fotodisociace klastrů $(HBr)_n$ byla změřena kvůli kalibraci. (3) Hmotová spektroskopie klastrů malých biomolekul imidazolu, pyrazolu a pyrolu byla zkoumána. Byla odhalena stabilizace těchto molekul, které jsou vázany vodíkovými vazbami, přenosem vodíku, což je relevantní ke stabilitě biomolekul obecně. (4) Konečně, fotodisociace molekuly HI na klastrech vody $(H_2O)_n$ byla studována a porovnána s fotodisociací na klastrech argonu $(Ar)_n$. Bylo ukázáno, že molekula HI podléhá acidické disociaci na $(H_2O)_n$ za tvorby obojetného ionu $H_3O^+ I^-(H_2O)_{n-1}$, který je následně excitován do biradikálového stavu s neutrální molekulou H_3O.

Klíčová slova: Fotodisociace, klastry a molekulové paprsky, hmotová spektroskopie, fotostabilita, atmosférická chemie

Title: Laser photodissociation of molecules in free nanoparticles
Author: Ondřej Tkáč
Department: Department of Chemical Physics and Optics
Supervisor: Doc. RNDr. Juraj Dian, CSc.
Supervisor´s e-mail adress: Juraj.Dian@mff.cuni.cz
Consultant: Mgr. Michal Fárník, Ph.D., AS CR, J. Heyrovský Institute of Physical Chemistry, Department of fotochemistry, spectroscopy and ion chemistry, Dolejškova 3, Prague 8

Abstract: Several experiments with various clusters were performed on a molecular beam apparatus. (1) The beam velocities were measured for rare gases and water clusters under various expansion conditions to learn about the supersonic expansions and cluster generation processes. (2) The photodissociation of $(HBr)_n$ clusters was measured for calibration purposes. (3) The mass spectrometry of clusters of small biomolecules imidazole, pyrazole and pyrrole was investigated. The stabilization of these hydrogen bonded species in the excited states by hydrogen transfer process was revealed, relevant to the stability of biomolecules in general. (4) Finally, the photodissociation of an HI molecule on water clusters $(H_2O)_n$ was studied and compared to the photodissociation on $(Ar)_n$ clusters. It was shown that HI molecules acidically dissociate on $(H_2O)_n$ and generate zwitterionic species $H_3O^+ I^-(H_2O)_{n-1}$, which are then excited into biradical states with the neutral hydronium molecule H_3O.

Keywords: Photodissociation, clusters and molecular beam, mass spectroscopy, photostability, atmospheric chemistry

1. Overview

There are two main topics in this thesis, specifically mass spectrometry of pyrrole, imidazole and pyrazole clusters (Section 4.3), and photodissociation of an HI molecule on water clusters $(H_2O)_n$ (Section 5.1). In the former, the differences between the various methods of cluster ionization, namely subsequent multiphoton and single photon ionization, as well as electron ionization are discussed. Another subject of interest is the differences between the ionization of imidazole and pyrazole clusters on one side, and pyrrole clusters on the other. These clusters differ in their hydrogen bonding motifs. The reason for studying this topic is given in section 2.3, where the constituents of biomolecules (pyrrole, imidazole and pyrazole) are introduced, and the possible causes of biomolecular damage are discussed. The different ionization methods are described in section 3.4, while the Willey McLaren time – of – flight and quadrupole mass spectrometer used for recording mass spectra, are described in sections 3.3 and 3.5, respectively. These results have already been published in the International Journal of Mass Spectrometry [1]. This publication can be found in the appendix A.

The reason for studying photodissociation of HI molecules on water clusters $(H_2O)_n$ is to verify the proposed mechanism of hydronium molecule H_3O formation in the previous experiment with HBr and HCl on water clusters $(H_2O)_n$ [2, 3]. These two molecules, as well as water clusters (nanoparticles), play an important role in atmospheric chemistry. Therefore, a brief introduction to atmospheric chemistry is given in section 2.2. Photodissociation process of molecules in clusters is described in section 2.4. Before we proceeded to study photodissociation of HI molecules on water clusters $(H_2O)_n$, a calibration measurement of photodissociation in $(HBr)_n$ clusters was performed. This experiment is described in section 4.2. The spectra were recorded by the Willey McLaren time – of – flight spectrometer in low field mode.

A similar experiment was performed with HNO_3 molecules on water clusters $(H_2O)_n$. The idea was to verify if a similar process, as in the case of photodissociation experiment with hydrogen halides on water clusters, occurs with other acids present in the polar stratospheric clouds. However, the H-fragment signal was never detected. Therefore, this experiment is only briefly mentioned in the section 5.2.

The third topic of this thesis, velocities measurement of the rare gases and water clusters, is described in section 4.1.2. The purpose of this experiment was to gain more information about the supersonic expansions and cluster generation processes in our experiment. The method of the velocity measurement is described in the section 3.2, while a theoretical introduction is given in the section 4.1, where the relation for the velocity of clusters is derived, and also in section 4.1.1, where the formation of clusters is described.

In addition, the other parts of our experimental apparatus are described in chapter 3, such as the laser and vacuum systems. In section 2.1 the molecular beams and clusters are introduced, to which we can proceed right now.

2. Theoretical background

2.1 Molecular beams and clusters

Molecular beams are produced by a gas expanding through a small orifice from a higher pressure system into an evacuated chamber. Under certain conditions, a beam of particles (atoms, molecules and clusters) is generated, which moves at approximately equal velocities with essentially no collisions between the particles along straight line in the vacuum, as was shown by Dunnoyer (1911) [4]. This phenomenon - called molecular beams – is widely exploited for fundamental research in many areas of physics and chemistry. More recently, it has also been extended into biological research and even technological applications.

Otto Stern was the first scientist who devoted himself to the systematic study of molecular beams. They provided the first experimental proof of the kinetic theory of gases by measuring their maxwellian speed distribution [5]. Another example of molecular beam importance were the demonstration of spatial orientation quantization of an atom in a magnetic field – Stern-Gerlach experiment [6], the evidence for the wave nature of heavy particles and experimental verification of the equation for the de Broglie wavelength [7]. The scientific community gained fundamental insights into the mechanisms and dynamics of chemical reactions in the gas phase and on solid surfaces by employing the molecular beam method. A Nobel Prize for the study of elementary chemical processes using this method was awarded to D. R. Herschbach, Y. T. Lee and J. C. Polanyi in 1986.

Great scientific breakthroughs were also achieved with cluster beams [8] in the 1950´s. It was recognized that molecules tend to condense in supersonic expansions and generate clusters in molecular beams. Clusters are aggregates of atoms or molecules of various sizes, ranging from groups of two up to a million, or even more. Clusters represent the „transition state“ between a single atom or molecule and the bulk. However, clusters have also some unique properties which distinguish them from the isolated molecules, as well as the bulk:

- One of the important properties of free clusters in molecular beams in a vacuum is the large number of internal degrees of freedom, which make them a very efficient heat bath with the ability to keep a constant low temperature due to the fast evaporation of particles from the cluster surface. The internal temperature of these clusters can be very low (for example, helium clusters of more than 100 atoms can achieve 0,37 K [9]).

- Clusters have a large surface-to-volume ratio; however their volume readily approaches bulk behavior. Therefore, the clusters can provide bulk-like conditions and at the same time, because of their finite size, it is possible to measure some observables inaccessible in the bulk (e.g. fragments of a molecule after the photodissociation are usually trapped in the bulk but they can escape and be detected if photodissociation proceeds in the cluster).

Molecular clusters and rare gases clusters, which are the scope of our investigations, are held together by bonds of a noncovalent nature, such as van der Waals interactions or hydrogen bonds (some clusters, however, can also be bound by covalent bonds, e.g. metal clusters). The energy of these weak intermolecular interactions is around 0,1 eV or even less, which means that these bonds can dissociate when irradiated by infrared light. On the other hand, the energy of covalent bonds in molecules reaches several electronvolts and dissociation of these bonds takes place in ultraviolet region. Since the typical physical size of a molecule is around 1Å = 10^{-10} m, clusters containing more than about 10 molecules have dimensions of nanometers, therefore they can be called nanoparticles.

Clusters are not only of great interest for fundamental research, but also for many areas of physics, chemistry and biology. They have applications in astrophysics, atmospheric chemistry, material sciences and even in technology. In our laboratory, we are mainly interested in two topics – atmospheric chemistry and biomolecules. A brief description of these topics as well as the reasons of our attention on these topics will be given in the two following subsections.

2.2 Atmospheric chemistry and nanoparticles

One practical importance of clusters is their role in atmospheric chemistry. Examples of clusters in the atmosphere are ice nanoparticles. They are formed in the polar regions of the stratosphere during the cold winter and they participate in the ozone depletion process. The stratosphere is the layer of atmosphere located about 15– 50 km above sea level and it is quite cold (185 – 275 K) and dry (2 – 6 ppm water vapor) [10]. The stratospheric ozone layer was an early consequence of oxygen production by life on Earth and through its shielding against harmful ultraviolet (UV) radiation from the sun it strongly influenced life’s development and is still responsible for its continuous protection. Natural and anthropogenic threats to the ozone layer have received increased attention over the past three decades [11].

Since the discovery of a hole in the ozone above the Antarctic in 1985, it has been postulated that a heterogeneous chemistry on the surfaces and in the bulk of liquid water and solid ice particles in polar stratospheric clouds (PSCs) play a key role in the ozone depletion process. Pollutant gas molecules (e.g. HOClO, HCl) react on the surface of ice particles in the PSC. These reactions convert relatively inactive and for ozone harmless molecules, e.g. HCl, to the active species such as Cl_2, which is readily dissociated by UV radiation into $Cl^{\cdot}$ radicals. The $Cl^{\cdot}$ radicals participate in a chain reaction leading to ozone depletion:

$$Cl^{\cdot} + O_3 \rightarrow ClO + O_2$$

$$ClO + O \rightarrow Cl^{\cdot} + O_2$$

Thus, one ozone molecule (O_3) and one oxygen atom (O) are transformed into two oxygen molecules (O_2) and the $Cl^{\cdot}$ radical is set free to repeat the reaction and destroy additional ozone molecules. In a similar way bromine atoms react.

HCl molecules can also be directly dissociated by UV radiation into $Cl^{\cdot}$ radicals, but the actinic photon flux at 50 km altitude in the absorption range of HCl (around 150 nm) is about five orders of magnitude smaller than in the absorption range of Cl_2 (around 320 nm). Consequently, considering the differences between the absorption cross sections of HCl and Cl_2 and the actinic flux in the stratosphere, it can be calculated that significantly less than 1% of $Cl^{\cdot}$ originates directly from HCl. Thus the direct HCl dissociation is neglected as a source of Cl radicals in the current atmospheric chemistry models and the PSC particles are involved mainly as catalyst to convert the reservoir species (HCl) to the active ones (Cl_2). However, if other processes on the PSC particle surface are considered, much larger $Cl^{\cdot}$ radical yields can be obtained directly from the UV irradiated particles, as has been shown in recent publications from our laboratory [3].

The stratosphere is not easily predisposed to cloud formation because of its dryness, and clouds are formed only during the extremely cold conditions of the polar winter. That is the reason why the ozone hole is generated above Antarctica, where also other meteorological conditions (e.g. a strong polar vortex of cold air) lead to PSC generation. Cloud particles strongly influence atmospheric chemistry via the activation of halogen species. The main role of PSCs in atmospheric chemistry is to provide a catalytic surface for various reactions.

In our lab we can mimic these atmospheric processes [2, 3, 12]. The role of ice nanoparticles in the atmosphere is represented by ice nanoparticles (water clusters) in our experiments. Water clusters can be doped with various pollutants, such as HCl. These species are subsequently subjected to the action of a UV laser pulse, which simulates the action of solar radiation.

2.3 The constituents of biomolecules in clusters

Biomolecules are the chemical compounds found in living organisms, where they perform important functions and are the building blocks of life. Biomolecules can be damaged by radiation either through direct interaction with photons (they can react in an excited state, fragment, or ionize) or indirectly: photons can ionize water, which forms an H_2O^+ ion and free electron. The H_2O^+ ion can react with more water molecules to form H_3O^+ and an $OH^\cdot$ radical. Consequently, biomolecules can be damaged by these $OH^\cdot$ radicals or by free electrons that have some kinetic energy. Therefore, photostability and resistance against electron impact of biomolecules is one of the conditions for the existence of life. In order to understand the photostability of these rather complex species at a detailed molecular level, we have to investigate the photochemistry of their simpler constituent molecules, namely of the UV chromophores such as the heterocyclic compounds – pyrrole, imidazole and pyrazole studied in this work. Schematic structure of these molecules is shown in Fig. 1.

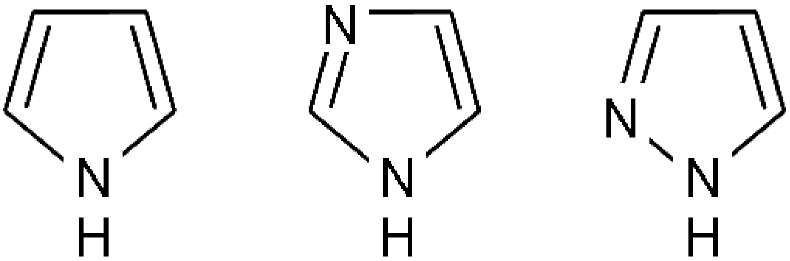

Pyrrole Imidazole Pyrazole

Figure 1. The schematic structure of heterocyclic nitrogen containing molecules.

The heterocyclic nitrogen containing molecules, pyrrole and imidazole, represent important constituents in many biomolecules. The pyrrole structure is present in hems and chlorophylls, which can be seen in Fig. 2(a). The imidazole structure can be found in purine, which is a skeletal building block of the nucleic acid bases adenine (see Fig. 2(b)) and guanine.

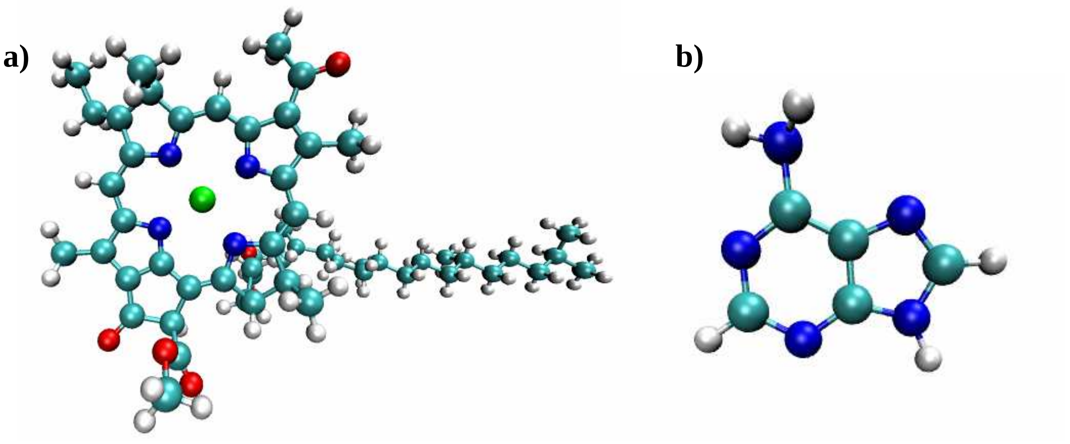

Figure 2. The model of chlorophyll with four pyrrole rings (a) and adenine with one five-membered pyrazole ring (b).

However, the study of the isolated constituent molecules in their gas phase does not necessarily provide a complete picture of the photochemistry of more complex biological systems, where the solvent can play an essential role. Therefore, to take a further step towards unraveling the photochemistry of biomolecules, we must study the photochemistry of the smaller constituent species solvated in clusters. This way the effects of the solvent on the photochemistry can be revealed.

In this thesis we present a study on dissociative electron ionization and photoionization of pyrrole, imidazole and pyrazole molecules in clusters, which are closely related to the question of stability of these species in a solvent environment. Pyrazole is studied, even though it is rare in nature. Due to the different position of nitrogen atoms in its heteroatomic ring, it forms hydrogen bonds different from those in imidazole and pyrrole. All three molecules, although structurally very similar, generate clusters with quite different bonding motifs, as illustrated in Fig. 3 for dimers. In pyrrole clusters, the N-H bond of one molecule binds to the π-electron cloud of the heteroaromatic ring of the neighboring molecule, forming a pattern of hydrogen bond N-H···π. In the imidazole clusters the N-H···N hydrogen bond is observed, and in the pyrazole clusters a double bond is presented similar to the DNA base pairs bonding motif. Thus, in pyrrole the chromophore does not react with the solvent while in imidazole and pyrazole, the hydrogen atom of the donor molecule can migrate to the acceptor molecule upon excitation and new phenomena can occur, e.g. hydrogen or proton transfer.

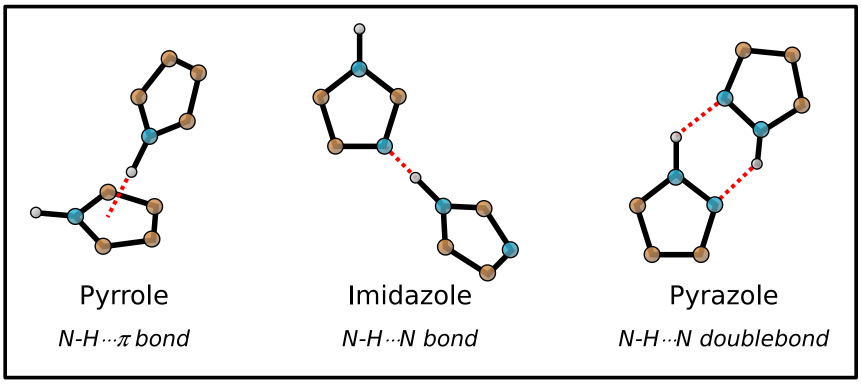

Figure 3. Schematic picture of different hydrogen bonding motifs of pyrrole, imidazole and pyrazole dimers. Hydrogen bonds are indicated by red dashed lines.

2.4 Photodissociation in clusters

In general, we investigate the influence of the environment on photoinduced processes, namely photodissociation and photoionization. It has been shown above that photodissociation in a macroscopic environment of condensed phase is very important, e.g. in biological systems. However, it is very difficult to investigate this process at the molecular level in the bulk. Therefore clusters represent the ideal environment for the investigation of photodissociation in a solvent.

Let us first consider the photodissociation of an isolated molecule. Photodissociation is the fragmentation of a bound molecule through photon absorption. The electromagnetic energy of a light beam is converted into internal energy of a molecule, and if this energy exceeds the binding energy of the weakest bond, the molecule can irreversibly break apart. We can write a photodissociation process of a molecule AB into products A and B as:

$$\mathrm{AB} + N\,\hbar\omega \;\; \text{—>} \; (\mathrm{AB})^{*} \; \text{—>} \; \mathrm{A}(\alpha) + \mathrm{B}(\beta), \qquad (1)$$

where N is the number of absorbed photons with energy $\hbar\omega$ ($\hbar$ is the Planck constant and ω angular velocity). The intermediate state $(\mathrm{AB})^{*}$ represents the excited state before it breaks apart, and the labels α and β denote the internal quantum states of the products A and B, respectively. The first step denotes absorption of the photons by the molecule AB and the second step represents the fragmentation of the excited complex.

Fig. 4(a) illustrates this process in terms of potential energy curves. Depicted there is a schematic potential energy curves (black lines) of the ground, and dissociative excited states (denoted by asterisk) of a diatomic molecule AB. In a general case of polyatomic molecules, multidimensional potential energy surfaces (PES) are obtained. They can be derived from the well known Schrödinger equation after application of the Born-Oppenheimer approximation. The PES represents the electronic energy *E* as a function of various atomic coordinates. The important point of the molecule AB ground state PES is the local minimum (in Fig. 4 denoted by Min.), which represents the stable conformation of the molecule AB. The molecule is excited by interaction with photon from the ground state to the excited state AB^*, the PES of which is repulsive, i.e. it has no local minimum. Therefore, this molecule AB in the gas phase has to dissociate to the corresponding fragments A(α) and B(β) (see Fig. 4(a)).

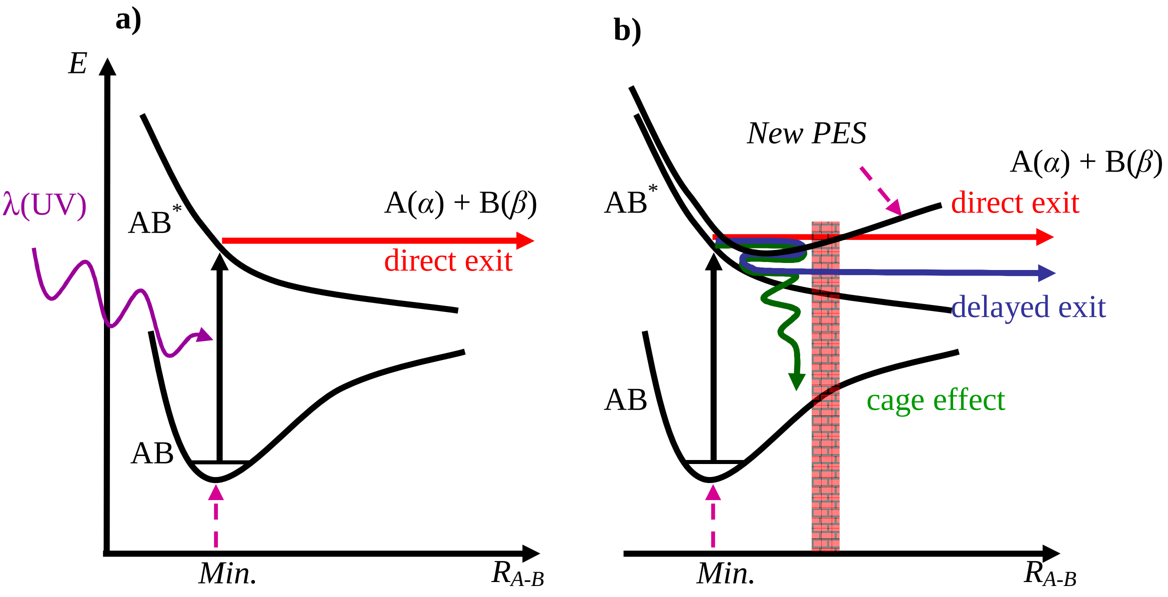

Figure 4. Diagram of the dissociation of the molecule AB alone (a), and in the presence of cluster (b).

Now, let us compare the dissociation process of an isolated molecule with the photodissociation process, which takes place in clusters. The presence of solvent molecules in the cluster is schematically represented in Fig. 4(b) as a wall, because the cluster species can encompass the molecule AB and influence the dissociation process. The solvent influences the photodissociation process of the molecule in the cluster in several distinguishable ways:

- The fragment passes through the barrier without any change in its energy through interactions with the atoms or molecules of a cluster. It should be noted that the wall is a quantum object and tunneling effect can occur. This is called a *direct cage exit.*

- The fragment collides with atoms or molecules in the cluster, loses part of its kinetic energy, and then dissociates. This is known as a *delayed cage exit.*

- Alternatively, the fragment loses all its kinetic energy in the interactions with the atoms or molecules of the cluster. This is called the *cage effect*, and it yields fragments with zero kinetic energy. The low energy fragments can also eventually recombine into the original molecule AB, quenched into its electronic ground state. This ground state is usually vibrationaly hot and can eventually predissociate, also yielding very low kinetic energy fragments.

- In addition, a fragment of the dissociated molecule, AB, can react with an atom or molecule of the cluster and new products can be created in *chemical reactions*.

- It also ought to be mentioned that the wall representation of the solvent is rather simplified schematic picture. Since the interaction of the species with an electronic structure must be considered, *electronic interaction* with a solvent can completely change the potential energy surfaces (the curve denoted as “New PES” in Fig. 4(b)) and close some dissociation or reaction channel, or open new ones.

Let us consider the photodissociation process in a cluster environment from the point of view of the *energy balance*:

$$\hbar\omega + E_{int}\,(\mathrm{AB}) = D_o + E_{int}\,(\mathrm{A}) + E_{int}\,(\mathrm{B}) + E_{kin}\,(\mathrm{A}) + E_{kin}\,(\mathrm{B}) + E_{clu}, \tag{2}$$

where $\hbar\omega$ is the energy of laser pulse, D_o is dissociation energy of the molecule AB (these two quantities are generally known), E_{kin} (A) and E_{kin} (B) are the kinetic energies of fragments A and B, respectively. E_{int} (A) and E_{int} (B) are excitation energies of the states α and β of the fragments A and B, respectively. In our case, one of these fragments, i.e. A is hydrogen atom H and therefore E_{int} (A) = 0 (there is not usually enough energy available to reach the first excited state of the hydrogen atom in our experiments). Finally, E_{int} (AB) is the initial excitation energy of the molecule AB, and the influence of the cluster is represented by the term E_{clu}, which expresses a continuous energy loss of the A-fragment caused by collisions and capturing processes by the cluster cage. Kinetic energy E_{kin} (AB) of the molecule AB can be taken as zero, since the photodissociation process is seen from the centre of mass of the molecule AB. In our experiments, we measure E_{kin} (A) and since all the other quantities are known (E_{kin} (B) is derived from the momentum conservation), we can determine the continuous energy loss E_{clu}, of the A-fragment in the interactions with the cluster, which in turn tells us the details of the dissociation in the cluster environment. For *direct cage exit* the energy loss by the cluster in equation (2) is zero, E_{clu} = 0.

3. Experimental apparatus

The experimental apparatus for the photodissociation of molecules in clusters was built and used at Max-Planck Institute in Göttingen [13]. The apparatus has been moved to J. Heyrovský Institute of Physical Chemistry in Prague in 2005.

The apparatus is composed of the vacuum system and laser system. The vacuum system consists of six vacuum chambers, where the various components of the experiment are placed. These parts are the molecular beam sources, pick-up cell, velocity selector, and pseudo-random chopper, Wiley-McLaren time-of-flight spectrometer, and quadrupole mass spectrometer. Fig. 5 shows an overview photograph of the experimental apparatus with its many components.

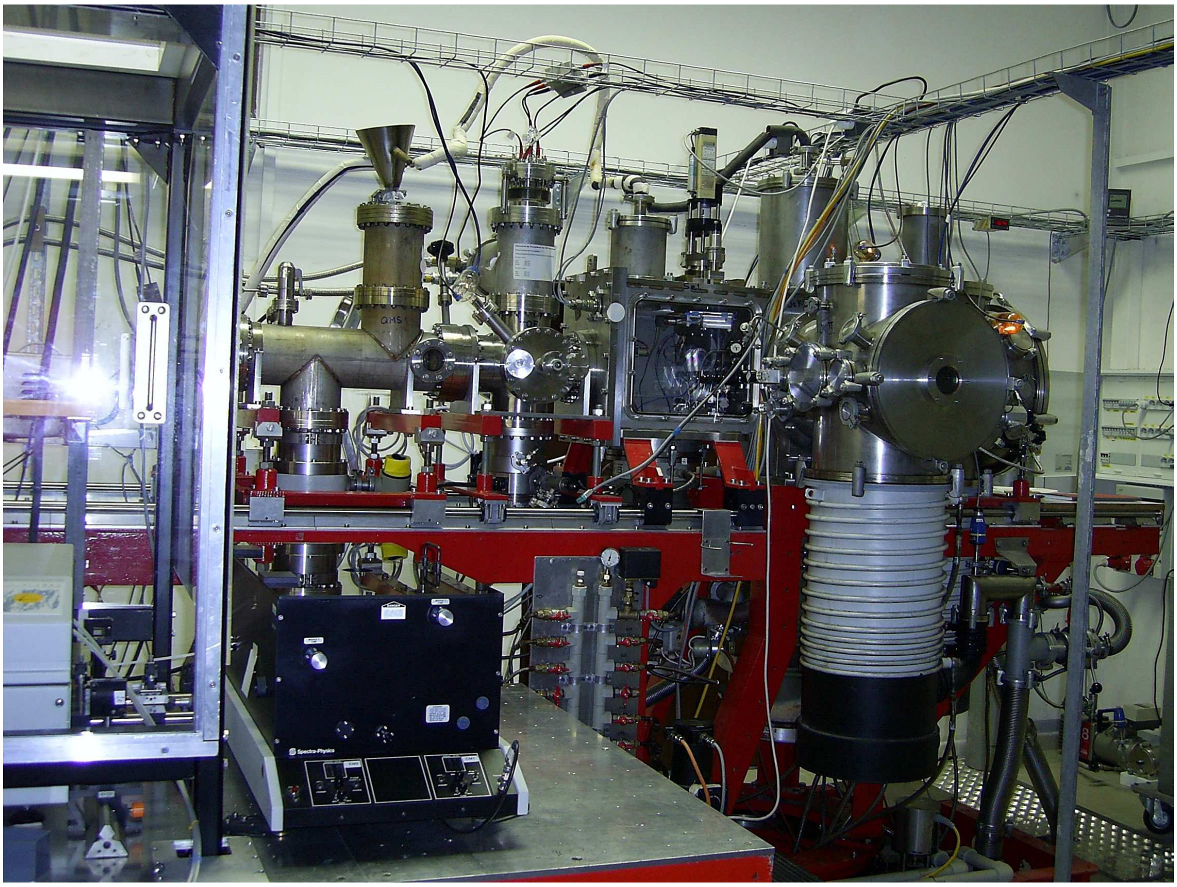

Figure 5. Photograph of the experimental apparatus

Fig. 6 schematically depicts the principle of the experiment. This crossed beam machine consists of a beam production assembly (chambers 1-3), the intermediate chamber 4, and the detection unit (chambers 5-6). The molecular beam with clusters is produced by a supersonic expansion into the vacuum through a divergent conical nozzle in the source chamber (CI). After passing through the skimmer (a cone shaped orifice), which shapes the supersonic expansion to the molecular beam, the beam enters the differentially pumped scattering chamber (SC). In this chamber, the cluster beam can be exposed to a secondary atomic beam of rare gas from the CII chamber arranged perpendicularly to the source chamber (CI). The elastic collisions of the clusters with the rare gas (He) atoms allow selecting the neutral clusters according to their size [14].

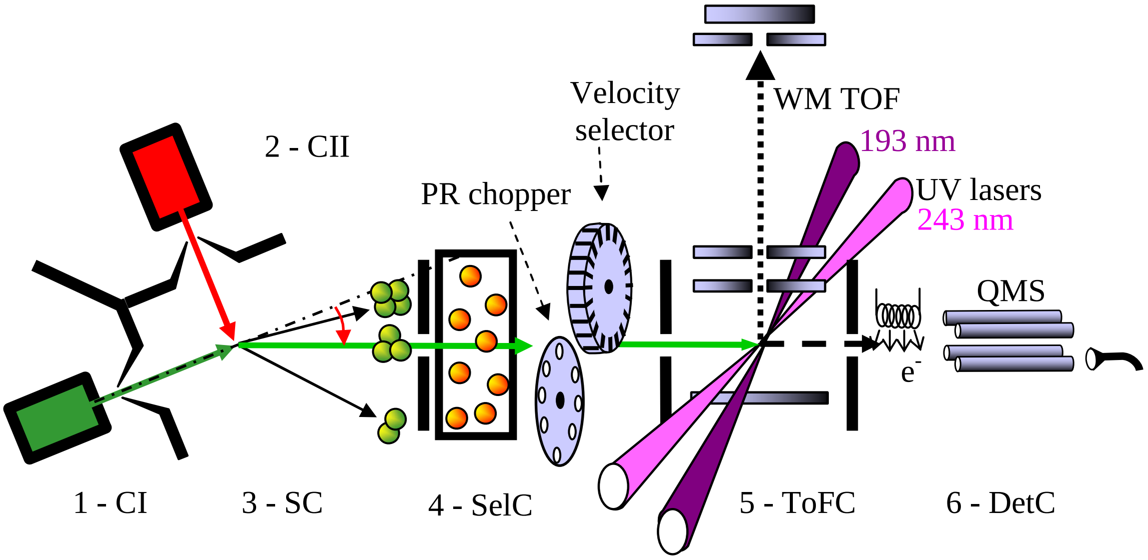

Figure 6. The scheme of experimental apparatus. Shown here are the chambers for producing cluster beams CI (1) and secondary molecular beam CII (2). The scattering chamber SC (3) is connected with selector chamber SelC (4) by flexible bellows. Finally, the time-of-flight (5) and quadrupole mass spectrometer (6) are pictured.

The clusters then enter the selector chamber, which contains a pick-up cell filled with a molecular gas. The molecules of this gas can be absorbed into the surface of the clusters [15]. The number of captured molecules depends on the pressure of the molecular gas. In some cases, the molecules can be also placed inside the cluster through co-expansion with the carrier gas. A velocity selector and pseudo-random chopper for analyzing cluster velocities are also placed in the selector chamber. Using velocity selector it is possible to only choose the clusters with a desired velocity, which directly corresponds to a single cluster size. However, the selector was not used in the present work. The pseudorandom chopper method, as described in section 3.2, serves to measure the cluster velocities. The clusters then enter the detection chamber (ToFC) which contains a two-stage Wiley-

McLaren time-of-flight spectrometer (WMTOF). In our photodissociation experiment, the molecules in cluster are dissociated by a laser beam at 193 nm or 243 nm, and the H-fragments are ionized via one-color resonance enhanced multi – photon ionization (REMPI) at 243 nm (see section 3.4).

The photodissociation products are extracted by a low electric field and their time of flight spectra are recorded. This means that we measure the amount of time which the fragments need to reach the detector. This time corresponds to the fragment velocity, i.e. the initial energy the fragment gained in the photodissociation process minus the energy the fragment lost in the interactions with the cluster. Thus, the TOF spectra can be converted into the H-fragments kinetic energy distributions, which provide detailed information about the photodissociation process.

The geometry in ToFC is as follows: The axis of the WMTOF spectrometer, 193 nm laser beam and molecular beam are mutually perpendicular. The 243 nm laser beam lies in the plane of the molecular beam and the 193 nm laser beam. The intersecting laser beams form an angle of 17,5°.

Alternatively, the cluster beam can directly enter the detection chamber which contains a quadrupole mass spectrometer, where the clusters are ionized by electrons and their composition can be analyzed.

The individual parts of the apparatus will be further described in the next several subsections.

3.1 Vacuum and vacuum pumps

For our experiments it is necessary to achieve a very good vacuum along the whole trajectory of the molecular beam (which is about 3m in length), due to the large cluster cross section, which can cause it to capture molecules (hydrocarbons) from the background. Another important condition, which has to be fulfilled, is that the mean free path *l* must be larger than the trajectory of the cluster in the apparatus. The mean free path *l* can be calculated as follows:

$$l = \frac{1}{\sqrt{2} \cdot n \cdot \sigma}, \qquad (3)$$

where n is the number of particles per unit volume and $\sigma = 4\pi.r^2$ is the effective cross sectional area for collision, r is the diameter of a particle.

By the way of example, the mean free path of an argon cluster can be calculated. The van der Waals diameter of an argon atom is $r = 1{,}81.10^{-10}$ m and it follows that the effective cross sectional area for the argon atom is $\sigma = \pi.r^2 = 0{,}41\,\mathrm{nm}^2$. The number of particles per unit volume n can be evaluated from the equation of state, which reads, after simple modification, $n = \frac{p}{k_B T}$. For the pressure p = 10^{-6} mbar, it follows that n = $2{,}4.10^{16}$ m^3. Finally, mean free path l of the argon atom from (3) is 72 m. Provided that the clusters of argon are spherical, the diameter of clusters increases with the third root of the number of particles in the cluster. Therefore the mean free path l for the clusters of about 120 atoms is longer than the whole trajectory in apparatus (3 m). Therefore if we want to produce and study argon clusters of several hundreds of atoms, the vacuum along the beam path has to be better than 10^{-6} mbar.

The vacuum chambers of the apparatus are kept at pressures from 10^{-4} to 10^{-9} mbar during the experiment. The chambers are evacuated by primary (rotary) pumps and high vacuum pumps (oil diffusion or turbomolecular pumps). In the case of source chambers (CI and CII) an additional intermediate pumping stage is added, using roots pumps to increase the pumping speed. The background vacuum is also improved by capturing residual molecules on the cold traps, cooled to 77 K by liquid nitrogen, in the quadrupole and selector chambers, and in the case of ToF chamber, trap is cooled by a liquid helium cold-head to 8 K.

Pressure values, which are obtained in the particular chambers without molecular beams p_0 and with molecular beams and molecules in pick-up chamber p are listed in Tab. 1. There are also listed vacuum pumps and their nominal pumping speeds. The presence of a molecular beam decreases the pressure noticeably in the first chamber (CI) and in the detection chamber (DetC). The molecular beams are produced in the CI chamber through the conical nozzle. Most of the expanding molecules actually do not form the molecular beam and remain in this chamber and the pressure increases. In addition, the molecular beams crash into the wall in the last chamber (DetC), therefore it results in the pressure increase in this chamber. In the rest of the chamber, the passing molecular beam influences the pressure only insignificantly through the particles which leave the molecular beam. The pressure in the SelC chamber increase, when the molecules are added into the pick-up chamber.

Table 1: Vacuum pumps, their type, pumping speed and cooling in particular chambers and the pressures in the chambers: without molecular beams p_0 and with molecular beams and molecules in pick-up chamber p.

Chamber	Forepump	Intermediate pumping stage	High-vacuum pump	Cold trap	p_0 [mbar]	p [mbar]
CI	Rotary Edwards E2M 175 175 $m^3.h^{-1}$	Roots Pfeiffer WKP 1000 1000 $m^3.h^{-1}$	Diffusion Leybold DI 6000 6000 $l.s^{-1}$	Liquid nitrogen	10^{-6}	10^{-4}
CII	Rotary Edwards E1M 175 175 $m^3.h^{-1}$	Roots Leybold WS 500 500 $m^3.h^{-1}$	Diffusion Leybold DI 6000 E 6000 $l.s^{-1}$	Liquid nitrogen	10^{-7}-10^{-6}	
SC	Rotary Alcatel T2033 30 $m^3.h^{-1}$		Diffusion Varian VHS 6 2700 $l.s^{-1}$	Liquid nitrogen	10^{-7}-10^{-6}	
SelC	Rotary Alcatel T2033 30 $m^3.h^{-1}$		Diffusion Varian VHS 6 2700 $l.s^{-1}$	Liquid nitrogen	10^{-7}	10^{-6}
ToFC	Rotary Leybold D16B 16 $m^3.h^{-1}$		Turbomolecular Leybold Turbovac 361 400 $l.s^{-1}$	Liquid helium Cold-head Leybold RGD 1245	10^{-9}-10^{-8}	
DetC	Rotary Edwards E2M 18 18 $m^3.h^{-1}$		Turbomolecular Balzers TPU 520 500 $l.s^{-1}$	Liquid nitrogen	10^{-10}	10^{-9}

3.2 Pseudorandom chopper - velocity measurements

In experiments with the molecular beam, the time-of-flight methods are widely used for velocity measurement. The basic idea is simple: to determine the speed of the particle *v*, while time *t*, which a particle needs to travel over a distance *L*, is measured:

$$v = \frac{L}{t}. \tag{4}$$

The problem is that the starting time of the measurement is impossible to determine by sensing when a particle enters the flight path, because there is not available such a high-efficiency nonionizing detector. That is the reason why the pseudorandom chopper method is used. The chopping of the beam is used to mark the zero of time. Hence, the measurement of time *t* can be done experimentally by letting the beam through a narrow slit and measuring the time it takes for the narrow pulse of particles to reach the detector. The particles of different velocities disperse in time of arrival at the detector. The flight-time distribution, *g*(*t*), would be measured with a single slit. The transmission of such slit would be infinitesimally small if a high resolution would be required. Therefore, it is experimentally realized by a chopper wheel with a sequence of slits. In other words, the beam is modulated by a pseudorandom sequence (it is equal to one in the case when the beam can pass, or zero, when the beam is blocked). When the sequence is such that the beam is blocked only half of the time, the corresponding transmission is 50%. The measured quantity is the time response function, *I*(*t*), which is the convolution of the pseudorandom sequence, *S*(*t*), and the distribution of flight times, *g*(*t*) [16]:

$$I(t) = \int_0^t S(t-\tau) g(\tau) d\tau = (S * g)(t). \tag{5}$$

The distribution of flight times, *g*(*t*), can be derived from the cross-correlation function of time response function, *I*(*t*), with the modulation function, *S*(*t*). The method is based on the fact that the autocorrelation function of a random function is a delta function. Since *S*(*t*) must vary from 0 to 1, we define random function *R*(*t*) that varies from -1 to 1:

$$S(t) = \frac{R(t)+1}{2}. \tag{6}$$

Consequently, a cross-correlation function of $I(t)$ with $R(t)$ is given by [16]:

$$C_{IR}(t) = \int_{-\infty}^{+\infty} I(t+\tau)R(\tau)d\tau = \int_{-\infty}^{+\infty}\int_{0}^{\infty} S(t+\tau-\lambda)g(\lambda)d\lambda R(\tau)d\tau\,. \tag{7}$$

Exchanging the order of integration:

$$C_{IR}(t) = \int_{0}^{+\infty}\int_{-\infty}^{\infty} S(t+\tau-\lambda)R(\tau)d\tau g(\lambda)d\lambda \tag{8}$$

and using the fact that the autocorrelation $R(t)$ is a delta function, we get the distribution of flight times, $g(t)$:

$$= \int_{0}^{+\infty}\int_{-\infty}^{\infty} S(t+\tau-\lambda)R(\tau)d\tau g(\lambda)d\lambda = \int_{0}^{+\infty} \delta(t-\lambda)g(\lambda)d\lambda = g(t)\,. \tag{9}$$

From the flight times, $g(t)$, may be calculated required velocity distributions, $f(v)$. The Jacobian of the transformation from velocity to the time space of the detector can be evaluated from (4):

$$dv = -\frac{L}{t^2}dt\,. \tag{10}$$

The desired velocity distribution is given by:

$$f(v) = g(t)\frac{dt}{dv} = -\frac{t^2}{L}g(t)\,. \tag{11}$$

Typically measured velocity distribution is shown in Sec. 4.1.2 (see Fig. 14).

The velocity measurement proceeds as follows. The beam of particles is modulated by a rotating chopper with two identical pseudorandom sequences of 127 slits in each semicircle of its circumference, which generate pseudorandom sequence of the ones and the zeros $S(t)$. The frequency of the chopper rotation is typically 492,1 Hz, which corresponds to the time resolution of 4 μs (in principle, any resolution can be used, since our program measures the frequency of the chopper rotation). As a slit in the chopper rotates over beam and allows the passage of a narrow bunch of particles. First, a distribution of particles in a space is released by the chopper gating function. Later this bunch spreads out according to the speed distribution of the beam and faster particles arrive to the detector earlier than the slower ones. The velocity distribution is evaluated from the measured function by the cross-correlation mathematical method outlined above.

3.3 Willey McLaren time – of – flight spectrometer

The Wiley-McLaren time-of-flight spectrometer (WMTOF) [17] is positioned in the detection chamber (ToFC). Photodissociation and photoionization take place in the extraction part of this TOF spectrometer, which is used in two different ways in our experiment:

1) As a mass spectrometer with a high accelerating voltage – more than 1 kV („high-field-mode“). It is desirable to reduce all structure of the TOF peaks to a δ-function corresponding to a particular ion mass, in the ideal case of the infinite mass resolution.
2) In the so-called low-field-mode. It means that the electric field accelerating ions towards the detector is small enough (~1-10 $V.cm^{-1}$) to preserve the information in the TOF peak shape about the kinetic energy which the fragments gained in the photodissociation process and eventually lost in the interactions with the cluster. Only one (typically proton) mass peak is detected in this mode and its structure is analyzed. This mode is used in the photodissociation experiments.

The TOF spectrometer is schematically illustrated in Fig. 7. It consists of two acceleration regions (two stage TOF spectrometer), with electric fields E_s and E_b, and a flight tube without any electric field, $E_D = 0$. As shown in Fig. 7, b = 1,1 cm is the distance between the repeller plate and the extraction grid, and the length of the second acceleration region is the same. D = 32,03 cm is the length of the field free drift region. Finally, s indicates the ionization position measured from the extraction grid. The repeller and extraction grid are connected with the voltage U_a and U_b, respectively.

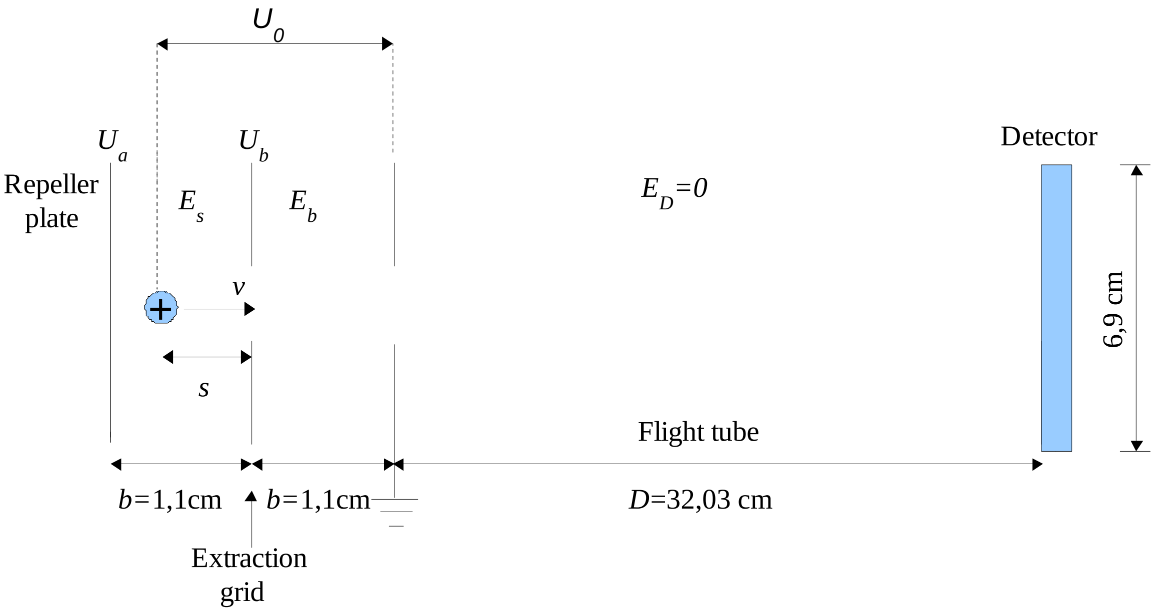

Figure 7. An illustration of the Wiley-McLaren time-of-flight spectrometer.

A brief description of the WMTOF application in mass spectrometry will be given below. The detection of ions of different masses proceeds on the basis of measurements of their time-of-flight, from the ion source to the detector t. Molecules are ionized by laser in the E_s field and the ion immediately begins to move toward and through the extraction grid. The ion enters the E_b field, which is 4,8 times stronger, and is accelerated into the field free flight tube that is vacuum enclosure and free of electrical fields ($E_D = 0$). Since all the ions achieved the same energy in the ion source (assuming the same starting point and initial velocity), the light ions attain higher speeds, travel faster and reach the detector earlier than the heavy ones. Given sufficient path length, ions become separated into individual packets according to their mass. For an ion with mass m and charge z, the total flight time to detector is given by $t = t_s + t_b + t_D$, where the indices designate the different parts of the total path. The different flight times can be derived directly from equation of motion [18]:

$$t_s = \sqrt{\frac{2ms}{zE_s}},$$
$$t_b = \frac{\sqrt{2m}}{zE_b}\left[\sqrt{U_0} - \sqrt{szE_s}\right], \qquad (12)$$
$$t_D = \frac{D\sqrt{2m}}{2\sqrt{U_0}}.$$

zU_0 is the total energy obtained after acceleration according to:

$$U_0 = szE_s + bzE_b = sz\frac{(U_a - U_b)}{b} + zU_b. \qquad (13)$$

The mass resolution $m/\Delta m$ depends on the finite ionization time (temporal effect), initial velocity distribution of neutral particles, e.g. thermal velocity distribution (can be separated into initial temporal and initial spatial contribution), and on the size of ionization volume (spatial effect). The influence of the temporal effect on the resolution can be reduced by increasing the length of the free drift region, *D*, (increasing the time of flight). To minimalize spatial effects on the resolution, a two-stage ion source was introduced, which separates ionization volume from the acceleration region. The influence of the ionization volume can be treated as follows. Total time *t* is a function of the ionization position *s*. Provided that ions are formed between $s = s_0 + \Delta s$ and $s = s_0 - \Delta s$, the time flight, $t(s)$, at $s = s_0$ may be expanded into Taylor series:

$$t(s_0 \pm \Delta s) = t(s_0) \pm \left(\frac{dt}{ds}\right)\Delta s + \frac{1}{2}\left(\frac{d^2 t}{ds^2}\right)(\Delta s)^2 \pm \ldots \tag{14}$$

The first derivatives vanishes at the position s_0 (for given operation conditions of the ion source) and a first order spatial focusing is obtained. This yields:

$$D = \frac{2 s_0 E_s}{E_b}\left(1 + \frac{b}{s_0}\frac{E_b}{E_s}\right)\left[1 + \left(1 - \frac{E_b}{E_s}\right)\sqrt{1 + \frac{b}{s_0}\frac{E_b}{E_s}}\right]. \tag{15}$$

Hence, for a given geometry of the TOF spectrometer (s_0, *d*, *D*), the position of the spatial focus can be adjusted by a suitable choice of the ratio E_b/E_s, such that it coincides with the position of the detector at the end of the TOF spectrometer. This ratio is ensured by a proper choice of voltages on the repeller and extraction grids. We used predominantly ratio U_a/U_b = 1250/1033 V in the mass spectrometry mode, and U_a/U_b = 50/41,34 V in the low field mode. Alternatively, a ratio U_a/U_b = 100/82,68 V can be used to increase the magnitude of the signal, but unfortunately also the total background signal).

As mentioned above, the TOF spectrometer is used in two different ways in our experiment, and some simplification of the equations (12) is possible:

- In the mass spectrometry applications, the E_s field is very large (specifically several hundreds V.cm^{-1}) compared to initial kinetic energy of an ion zU_0, which can be neglected. Consequently, simple relation instead of (12) is obtained, in which mass *m* is proportional to the square root of the time t_c, $m \approx \sqrt{t_c}$.
- In the so-called low-field-mode used in the photodissociation experiments, initial kinetic energy of an ion zU_0 is not negligible in comparison with the small applied

field E_s. And initial kinetic energy of an ion zU_0 can be calculated from the measurement of the time t.

As the ion detector, a multichannel plate (MCP) in chevron ordering is used. MCPs consist of a large number of closely packed channels with an identical diameter. The inner surface of the channels is coated with a lead-oxide (PbO) glass that produces secondary electrons when strucked by a charged particle. The electrons are accelerated through the channels by an applied potential difference, in our case from 1,1 to 1,7 kV. Each channel acts as an independent multiplier with amplification factor of the order of 5.10^4. Higher amplification factors can be achieved by combining more MCPs together. Hence, the chevron design of MCPs is used in our experiment. It consists of two MCP wafers stacked onto each other with opposing tilt directions.

The fast digital oscilloscope (Tektronix TDS 520, 500MHz) is used to record and save the measured signal, because of its high scanning frequencies. Signal originating from one laser pulse is superimposed over a high statistical noise from the background. To improve the signal-to-noise ratio, the signal is averaged over typically 10^4 laser pulses (which corresponds to a measurement time of about 20 minutes). The starting signal of the measurement is determined by laser pulse sensing using a fast photodiode.

3.4 Different ionization methods

A key process, which we have not discussed so far in the above section about TOF spectrometer, is the production of the ions from neutral clusters, which are recorded by the MCP detector. Photoionization is a physical process, in which the molecule or atom is excited above its ionization limit and the incident photon(s) ejects one or more electrons e^- from the atom or molecule AB:

$$\mathrm{AB} + N\cdot\hbar\omega \rightarrow \mathrm{AB}^* \rightarrow \mathrm{AB}^+ + e^- \qquad (16)$$

The molecule can dissociate during this process into two or more fragments and dissociative ionization can also occur:

$$\mathrm{AB} + N\cdot\hbar\omega \rightarrow \mathrm{AB}^* \rightarrow \mathrm{A}^+ + \mathrm{B} + e^- \qquad (17)$$

Alternatively, excitation to ion-pair state may also be important [19]:

$$\mathrm{AB} + N\cdot\hbar\omega \rightarrow \mathrm{AB}^* \rightarrow \mathrm{A}^+ + \mathrm{B}^- \qquad (18)$$

We can distinguish between several types of photoionization processes: from the point of view of the number of absorbed photons, from the point of view of the photon energies and their correspondence to the energy levels of the ionized species etc.

1) Single-photon ionization: (N =1), only one photon participates in this process, and it is necessary that it has enough energy for the molecule to overcome the ionization limit. The scheme of this process is depicted in Fig. 8(a). Since the typical ionization potentials of most molecules exceed 10 eV, such processes require high energy photons available primarily from synchrotron sources and similar extreme ultraviolet sources (from 10 to 120 nm). Since these photon sources were not exploited in our experiments, we have to use the multiphoton ionization method explained below.

2) Multi-photon ionization (Fig. 8(b)): (N >1), in this case, more than one photon is necessary to excite the species into the ionization continuum. Generally, the probability of such a process decreases dramatically with the number of photons required to overcome the ionization potential. Thus, two-photon ionization is typically more than an order of magnitude less probable than a single-photon ionization of the same species. This is due to the fact that the two (or more) photons have to be absorbed simultaneously to ionize the molecule. This is only possible at very high photon flux densities, i.e. with intense laser beams.

   The probability of such a process is enhanced if the species, after the absorption of the first (or first few) photon(s), can remain in some excited state where they can await the arrival of the next photon(s), which excite them further into the ionization continuum. An example of such a process is called resonance enhanced multiphoton ionization (REMPI), which will be discussed below. Another example treated in this thesis is a non-resonant multiphoton ionization in clusters, as discussed in Sec. 4.3. In this case, the molecule in a cluster can be excited into a dissociative state. It can then be caged by the cluster, and before it relaxes into a ground state, it can absorb another subsequently (with some delay) arriving photon(s), which can ionize the molecule. Further details of such processes specific to the clusters and their dynamics, will be discussed in Sec. 4.3.

3) Resonance Enhanced Multiphoton Ionization (REMPI) is a special type of multiphoton ionization, which is also possible for a molecule or atom. If an intermediate electronic state exists for the specie, in which it can be excited by the first (or first few) photon(s) and await the arrival of the next (delayed) ionizing

photon(s), the ionization probability can increase orders of magnitude compared to the non-resonant multiphoton ionization. Fig. 8(c) illustrates such three-photon process: the first two photons arriving simultaneously excite the specie into an electronic state and the third photon excites it further into the ionization continuum.

An example of such process, used in our experiments to detect H-fragments, is the 2+1 REMPI ionization of the H atom. The first two photons excite the 2s←1s transition in hydrogen (Lyman-α line), and the third one ionizes it. All three photons are of the same wavelength 243,07 nm – so called one-color excitation. In principle, different wavelengths can be used, e.g. a two color excitation scheme 1+1’ REMPI of hydrogen, where the first photon has 121,5 nm one and the second one has 364,5 nm wavelength (The 121,5 nm is produced by tripling the 364,5 nm, which is XeCl excimer laser).

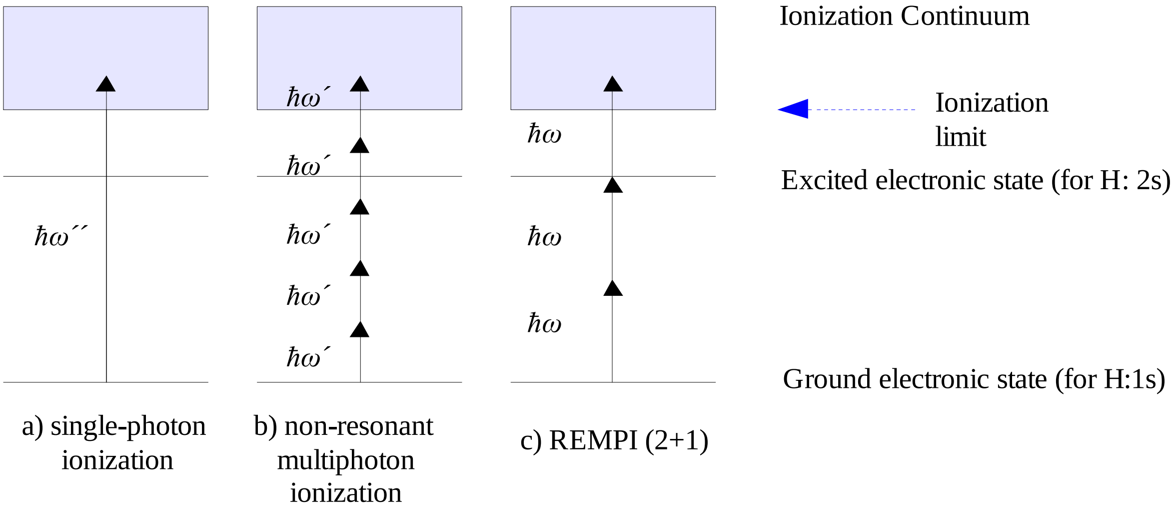

Figure 8. Scheme of different kinds of photoionization methods.

In addition, in the next section we will discuss another type of mass spectrometric device used in our experiment: the quadrupole mass spectrometer. Here, too, the clusters have to be ionized in order to be mass selected and detected. A different kind of ionization – electron ionization - is exploited here. Electron ionization (EI) is an ionization method in which an energetic electron interacts with an atom or molecule AB to produce an ion and another electron:

$$AB + e^- \rightarrow AB^+ + 2e^- \qquad (19)$$

$$AB + e^- \rightarrow A^+ + B + 2e^- \qquad (20)$$

Again, non-dissociative (19) and dissociative (20) processes are possible. It ought to be mentioned that the clusters fragment substantially upon the electron ionization [1] and the measured mass spectra by no means reflect the neutral cluster size distributions.

In our quadrupole mass spectrometer electrons are produced through thermionic emission by heating a wire filament that has electric current running through it. The efficiency of ionization depends on the type of molecule or atom and on the energy of electrons. The electrons have typical energies of 70 eV and the de Broglie wavelength of such electrons (0,147 nm) matches the length of typical bond in organic compounds (C-C: 0,154 nm; C-N: 0,147 – 0,210 nm), therefore energy transfer to a molecule is maximized and the strongest ionization and fragmentation occur.

3.5 Quadrupole mass spectrometer

The quadrupole mass spectrometer serves to measure the mass spectra after the electron ionization of the clusters, from which we can analyze the cluster composition. A schematic picture of the quadrupole mass spectrometer is shown in Fig. 9.

The quadrupole mass spectrometer consists of three main parts:

- *Ion source*: in our case, the ions are produced by a high efficiency electron ionizer. The energy of these ionizing electrons is typically 50 - 70 eV. The nascent ions are then directed to the entrance of the quadrupole mass analyzer by a three element einzel-lens.

- *Quadrupole mass analyzer*: it consists of 4 circular metal rods - electrodes (Extranuclear Laboratories, model 162-5, length: 12,7 cm), set perfectly parallel to each other. Each opposite pair of rods is connected together by direct current (DC) and radio frequency (RF) voltage is applied between each one pair of rods (typically a constant RF frequency, 700 kHz – a few MHz). The electric fields between the rods guide the ions of appropriate mass-to-charge ratios through the device to the detector.

- *Detector of ions*: the separated ions produce an electric signal that can be measured and interpreted. As a detector, we use a channeltron Galileo Model 4840G (single channel electron multiplier).

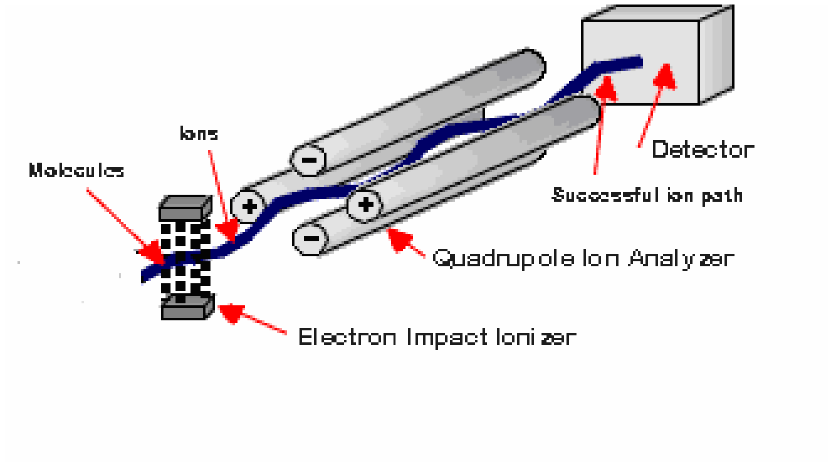

Figure 9. Schematic picture of the quadrupole mass spectrometer [20].

In the following, we will describe the working principle of the quadrupole mass analyzer [21]. The treatment of quadrupole theory starts with derivation of the Mathieu equation from Newton law: $F = m.a_0$. The final version of the Mathieu equation with the parametric substitution reads:

$$\frac{d^2 w}{d\xi^2} + (a - 2q\cos 2\xi)w = 0 \text{, where } a = \frac{8zU}{mr_0^2\Omega^2}, \; q = \frac{4zV}{mr_0^2\Omega^2}, \; \xi = \frac{\Omega t}{2}. \tag{21}$$

The w represents a position along the coordinate axes (x or y), z is the charge, U is applied DC voltage, V is applied zero-to-peak RF voltage, m is the mass of an ion, r_0 is the effective radius between electrodes, and finally Ω is the applied RF frequency. Through rigorous analytical solution of this equation ion trajectories can be found [21]. It is acceptable to consider ion trajectories as infinite sums of sine and cosine functions, each successive term has smaller amplitude and higher frequency. It means that motion, in each of the x and y directions, is sinusoidal.

We are interested if the ion have stable trajectory at the given voltages. For this purpose, the solution of the Mathieu equation can be treated graphically. The families of solution boundaries for the Mathieu equation, which have stable trajectories and lie near the origin, are shown in Fig. 10(a). There are four distinct regions of stable trajectories for ions moving through the quadrupole. The traditional operating region for quadrupole mass analyzer is denoted by A, and this first stability region is plotted in Fig. 10(b). The shape of this first stability region depends on the m/z ratio of given ions. The magnitude of parameter a depends on the applied DC voltage, while the parameter q on the applied RF voltage. The RF and DC voltages are scanned through the values along the linear scan line plotted in Fig. 10(b). For the given ratio of DC and RF voltages (a/q = const.) could be read directly from this figure, if ions of m/z would have stable trajectory. The shaded area represents voltages with stable trajectories, while the region outside of this area represents unstable trajectories. Hence, ions have stable trajectories for q between q_1 and q_2. The peaks width increases geometrically with increasing mass-to-charge ratio in the case of linear scan line. To avoid this, a scan line must be a curve with an increase in the DC to RF voltage ratio as mass increases.

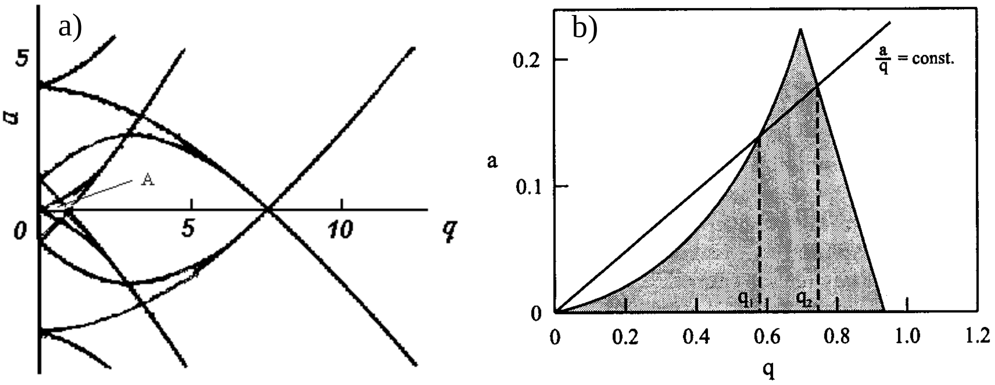

Figure 10. (a) The Mathieu stability diagram- the first region stability is denoted by A. (b) A magnified view of the region A [21].

The amplitude of the voltages determines which masses have stable trajectories in the quadrupole mass analyzer. Ions travel between the rods, and only ions with a certain mass-to-charge ratio m/z reach the detector for a given ratio of voltages. Other ions, having unstable trajectories, are neutralized by striking the quadrupole electrodes. This allows selection of an ion with a particular m/z by varying the voltages.

3.6 Laser system

The laser systems are in principle used for two kinds of experiments:

- One-color experiments, where the photodissociation of molecules, as well as subsequent photoionization of H atoms by REMPI process in a 2+1 excitation scheme (section 3.4) is performed using the same wavelength of 243 nm.
- Two-color experiments, where the molecules are photodissociated at 193 nm, and the subsequent photoionization of H atoms is performed by the wavelength of 243 nm.

Two different lasers are available in our laboratory: an excimer laser and a tunable laser system. A brief description of these two laser systems, which both operate in the ultraviolet range, will be given in the following two subsections.

3.6.1 Tunable ultraviolet laser

The tunable ultraviolet laser system consists of a Nd:YAG laser (Quanta Ray GCR-5), dye laser (LAS, LDL 20505) and wavelength extender (WEX). The scheme of this system is represented in Fig. 11. This tunable ultraviolet laser can operate in the UV range between 217 nm and 437 nm by tuning the wavelength of dye laser and exchanging the mixing crystals in the WEX. However, in the present experiments, it is used at the constant wavelength of 243,07 nm for REMPI of H-fragments. This wavelength is achieved by a complicated process, which starts in the Nd:YAG laser.

This laser emits a pulse with a wavelength of 1064 nm, which is doubled by KDP 58° (Potassium Dihydrogen Phosphate) to generate a wavelength of 532 nm. This process, called the second harmonic generation (SHG), is a nonlinear process, in which photons interacting with an optically nonlinear material (KDP) are combined to form new photons with twice the energy. Therefore, their wavelength corresponds to the half of the wavelength of the initial photons. This beam at 532 nm enters the dye laser (green line in Fig. 11), while the original beam at 1064 nm (dark red line in Fig. 11) goes around the dye laser and will participate in a sum frequency mixing (see below).

Our dye laser uses as a lasing medium organic dye DCM dissolved in methanol with range of wavelength between 604 – 672 nm and maximum at 642 nm. The doubled frequency laser beam from the Nd:YAG laser at 532 nm is used to pump the dye. For the generation of the 243 nm UV light at the end of the system, the dye laser is tuned to 630,3 nm. This beam passes through a telescope (formed by two lenses), and enters the WEX, where it undergoes frequency doubling by another non-linear crystal KD^*P resulting in a wavelength of 315 nm.

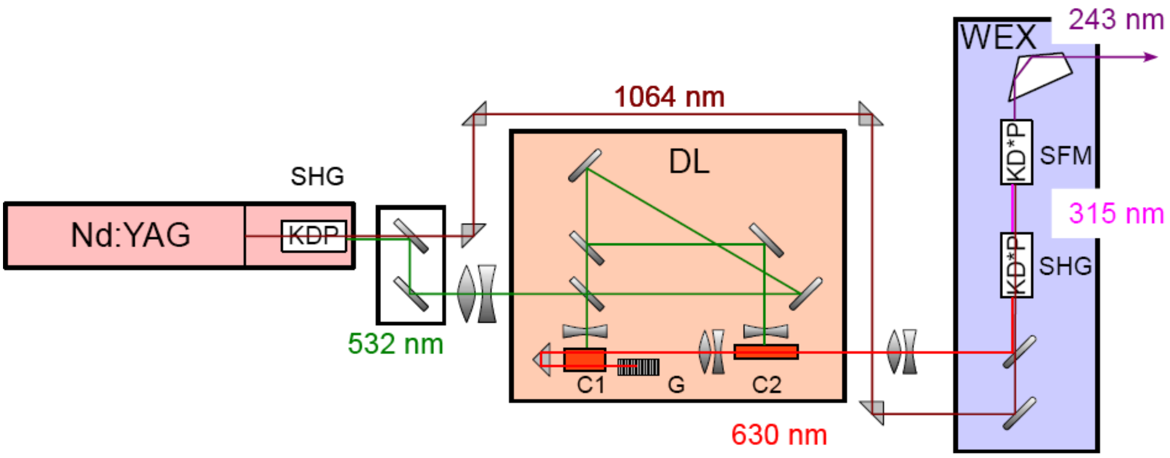

Figure 11. Tunable UV laser: SHG-second harmonic generation, SFM-sum frequency mixing, WEX- wavelength extender, KDP (Potassium Dihydrogen Phosphate) and KD*P (Potassium Dideuterium Phosphate) – crystals for second harmonic generation and sum frequency mixing, C_1 – oscillator and pre-amplifier (dye cell) C_2 – main amplifier (Bethune cell), G - grid.

In the second crystal KD*P 68° of the WEX unit the original pulse at 1064 nm is combined with the other laser pulse at 315 nm in a process called sum frequency mixing (SFM). Sum frequency mixing is a second order non-linear process, in which two photons with wavelength λ_1 and λ_2 are annihilated while, simultaneously, a new photon with wavelength λ_3 is generated. It follows from the law of momentum conservation that:

$$\frac{1}{\lambda_1}+\frac{1}{\lambda_2}=\frac{1}{\lambda_3}. \tag{22}$$

Since λ_1 = 1064 nm and λ_2 = 315 nm, it follows from the relation (22) that the wavelength of the nascent radiation is λ_3 = 243 nm. The typical energies of a laser pulse after individual processes are listed in Tab. 2, from which continuous decrease can be seen in the energy of the laser pulse.

Table 2. Energies of laser pulses at individual stages of laser system

λ [nm]	532	1064	630	315	243
Energy [mJ/pulse]	~800	~1000	~180	~20	~3

As has been already mentioned, the main utilization of this laser pulse at 243,07 nm is for the (2+1) REMPI process of hydrogen atom, but it can be used also for photodissociation.

The energy corresponding to the wavelength 243 nm is 5,1 eV. The typical energy of this resulting laser pulse is about 3 mJ and duration of these pulses is about 5 ns. The repetition frequency of the pulses is 10 Hz.

The laser beam is focused into the detector chamber by a 400 nm quartz lens to a point of 14 μm radius in the intersection point of the WMTOF axis and cluster beam. The polarization angle of the linearly polarized laser beam can be turned perpendicular (90°) or parallel (0°) with respect to the WMTOF axis by passing the beam through a series of 90° turning prisms. A photograph of our tunable ultraviolet system is shown in Fig. 12.

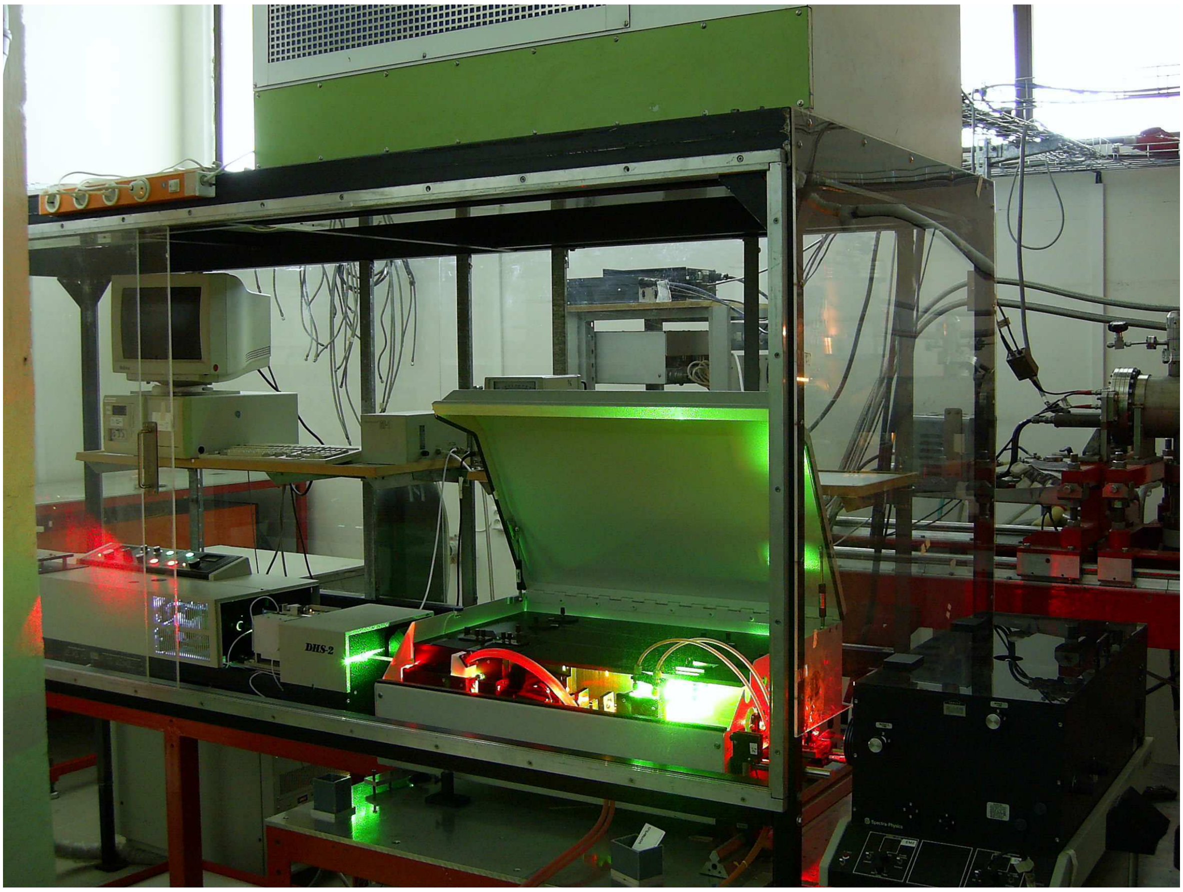

Figure 12. Tunable ultraviolet laser system.

3.6.2 Excimer laser

An ArF/F_2 –Excimer laser (Lambda Physics: LFP 202) operates at a wavelength of 193 nm. It generates laser pulses with energy up to 200 mJ with duration about 20 ns. The repeating frequency of the pulses is 10 Hz. This laser is used to dissociate molecules. The energy corresponding to a wavelength of 193 nm is 6,41 eV.

The emitted unpolarized light can be polarized by a thin film polarizer. The laser light polarization can also be changed from 0° to 90° polarization angle with respect to the WMTOF axis by the rotation of the thin film polarizer. However, the use of the thin film polarizer lowers the intensity of the laser beam by more than an order of magnitude.

The laser beam at 193 nm is focused into the chamber by a 366 nm LiF lens. It is confined in the plane of the molecular beam and the 243 nm laser beam. Both laser beams form an angle of 17,5°. The 193 nm beam is oriented perpendicularly to both the cluster beam and the WMTOF axis.

In the two-color experiment, the two laser pulses have to be synchronized. The 193 nm pulse has to dissociate the molecules first and the ionization laser pulse at 243 nm has to arrive about 5 – 20 ns after the first one. Time synchronization of the two laser pulses is achieved by externally triggering the excimer laser by Nd:YAG laser trigger through a pulse delay generator (Standford Research: DG 535).

The laser beams are focused into the chamber into a tight spot of 10 μm. The excimer laser beam is of a rectangular shape and slightly divergent, therefore it cannot be focused into a spot by circularly symmetric optics. However, the spatial overlap of the two laser beams is crucial for intensity and spectra-shape reasons. In addition, the intersection point has to coincide with the molecular beam, and also with the center of the WMTOF extraction region for the same reasons. This demanding condition on overlaps was adjusted on the intensity and symmetric shape of the measured time-of-flight spectrum of the $(HBr)_n$ system (section 4.2).

4. Experiments and results

4.1 Supersonic expansions and velocity measurements

Molecular beams are prepared by an expansion of gas into a vacuum through a conical nozzle. The expansion can be characterized by the Knudsen number:

$$K_n = \frac{\lambda}{d}, \tag{23}$$

where λ is the mean free path and d is the diameter of the nozzle. For more than forty years after Dunnoyer´s first molecular beam experiment, the effusion of gases from sources was the only method for producing the thermal energy of molecular beams. This effusion beam, which is characterized by slower velocity molecules with a broad distribution, can be found in the region of the Knudsen number $K_n > 1$. In this case, the mean free path of particles λ is larger than the diameter of the nozzle d, hence the particles move through the nozzle almost without collisions.

Kantrowitz and Grey (1951) suggested use of dynamic gas expansion through the nozzle, instead of effusive flow, for formation of the beam. Because of a large number of collisions during the dynamic expansion, the speed distribution is narrow and its maximum is shifted towards higher velocities. These beams are characterized by higher density of the particles. For Knudsen number holds $K_n << 1$, it means that particle mean free path is much smaller than the nozzle diameter. Therefore, there are many collisions during the expansion. In this case we are talking about supersonic expansion, which is used for preparing molecular beams in our experiment. The particles of the gas are accelerated towards the orifice of the nozzle by the difference between the pressure of the background in vacuum p_b and the pressure of the gas in the nozzle p_0. Before leaving the nozzle thermal energy of the gas is changed into the steady flow of particles with a velocity u during this acceleration by collisions of particles. During these collisions, clusters can be formed. The expansion cools the vapor, which becomes supersaturated, and clusters condense. The particles reach the local sonic speed at the orifice (in our special case of the divergent conical nozzle it is at its beginning– at the minimum cross-sectional area of beam). The cross-sectional area of the beam is further increasing and as follows from (3.28) in [18], for velocity of beam u bigger than local sonic speed, this velocity of beam u is increasing as cross-sectional area increases. The supersonic speed of the beam is achieved at the nozzle throat. The decrease of sonic speed as temperature decreases contributes to achieve supersonic speed.

In a thermodynamic picture, supersonic expansion can be described as an adiabatic process. This means that particle-wall interactions are neglected during the expansion. The general relation follows from the energy conservation for the flow velocity u_1 of a collimated molecular beam:

$$U_0 + p_0 V_0 + \frac{N_A m}{2} u_0^2 = U_1 + p_1 V_1 + \frac{N_A m}{2} u_1^2 = E\,, \tag{24}$$

where total molar energy E is a sum of the internal molar energy U, describing the random translational and internal motions of the particles, the pressure-volume work pV, caused by the change in volume V occurring at pressure p, and the kinetic energy $\frac{N_A m}{2} u^2$ of N_A particles in the direction of beam movement by the velocity u. This energy balance (24) does not take into account the condensation energy released during cluster formation, and is thus valid exactly only for the molecular beams in which clusters are not produced. This equation assumes that all particles have the same mass m and the same velocity u_0. N_A is the Avogadro constant, and the index 0 marks the state of particles within the reservoir before expansion, while the index 1 denotes terminal state of the molecular beam. The necessary condition for any practical application of the equation (24) is a thermal equilibrium between the particles and the reservoir walls and the nozzle, allowing the assignment of the nozzle temperature T_N as the temperature of particles T_0 before leaving the nozzle. It is equivalent to the assumption that the thermal exchange between the nozzle and the particles is very fast and effective, or that the majority of particles remains in the nozzle for a long enough time before expanding, which is satisfied.

The simplification of the equation (24) requires another assumption: provided that the center-of-mass motion of the particles within the reservoir can be neglected, thus $u_0 \approx 0$. Then the total energy of the particles within the reservoir (before leaving the nozzle) is identical to its enthalpy: $E = H_0 = U_0 + p_0 V_0$ and the equation (24) is reduced to:

$$H_0 = H_1 + \frac{N_A m}{2} u_1^2, \tag{25}$$

where $H_1 = U_1 + p_1 V_1$. The assumption that the center-of-mass motion $u_0 \approx 0$ is equivalent to the requirement, that a sufficiently small flux of the particles leaving the volume and the disturbance of the thermodynamic equilibrium within the reservoir is insignificant.

Because the enthalpies are difficult to access, it is frequent to use the expression:

$$H_0 - H_1 = \int_{T}^{T_0} c_p dT^{'} = c_p (T_0 - T\ ) , \tag{26}$$

where T_0 denotes the temperature of the particles before leaving the nozzle, T is an equilibrium temperature of the gas after expansion, and c_p is the heat capacity at constant pressure. However, the relation (26) is valid only for a heat capacity c_p independent of the temperature. This is a severe simplification, due to the large change of temperature achieved in a supersonic jet expansion. The heat capacity c_p changes by a factor of four in the temperature range 3-300 K for helium [22], which is usually considered as an ideal gas. Therefore (26) is rigorously valid only for the model representation of an ideal gas, for which the heat capacity is temperature independent, while for any real system it is an approximation. However, despite of this approximation, it gives results in a very good agreement with the experiment as will be shown in section 4.1.2.

From equations (25) and (26), the relation follows for the flow velocity u_1 of the molecular beam:

$$u_1(T_0, T) = \sqrt{\frac{2c_p}{N_A m}(T_0 - T)} . \tag{27}$$

Local temperature T, characterizing thermal movement of molecules, is falling during expansion. Let us assume a case where the entire initial enthalpy, H_0, is transformed into the kinetic energy of molecules in the direction of the beam movement. For this case, the temperature, which corresponds to no thermal movement, will be T = 0 K at the end of expansion. Therefore the velocity of the molecular beam will reach its maximal value (in principle this value would be reached in infinity, where the temperature T would decrease to zero):

$$u_{\max}(T_0) = \sqrt{\frac{2c_p T_0}{N_A m}} . \tag{28}$$

It is possible to avoid the extremely problematic occurrence of the isobaric heat capacity c_p in the expression (28) by introducing:

$$c_p = R\frac{\gamma}{\gamma - 1}, \tag{29}$$

where $\gamma = \frac{c_p}{c_V}$ is the heat capacity ratio. γ = 5/3 for a monatomic gas, γ = 7/5 for a diatomic gas and γ = 4/3 for polyatomic gas. R is the gas constant and c_V is the heat capacity at constant volume.

Assuming ideal gas properties, the maximal flow velocity, u_{max}, can be expressed as:

$$u_{\max}(T_0) = \sqrt{\frac{2k_B T_0}{m}\frac{\gamma}{\gamma - 1}}, \tag{30}$$

where $k_B = \frac{R}{N_A}$ is the Boltzmann constant. For the ideal gas, the flow velocity depends on the temperature, but not on the pressure. On the other hand, for any real system the density of the gas influences the mutual particle interactions and therefore results in a pressure dependent heat capacity ratio $\gamma(T_0, p_0)$. This is true even for rare gases such as neon or argon. To model the dependence of the flow velocity on the stagnation pressure, the equation (30) is often generalized [23, 24]:

$$u_{\max}(T_0, p_0) = \sqrt{\frac{2k_B T_0}{m}\frac{\gamma(T_0, p_0)}{\gamma(T_0, p_0) - 1}}, \tag{31}$$

where the temperature and pressure independent heat capacity ratio γ is, otherwise, replaced with a more realistic function $\gamma(T_0, p_0)$, which can be calculated from tabulated values of the heat capacities $c_p(T_0, p_0)$ and $c_V(T_0, p_0)$. However, equation (30) was derived assuming temperature independent heat capacities, therefore the implementation of the temperature dependent capacity ratio into equation (31) is rather an empirical correction to account for the pressure dependence of the flow velocity. To rigorously explain the dependence of the flow velocity on the stagnation pressure, the approximation (26) cannot be used and the flow velocity u has to be calculated directly from the enthalpies:

$$u(H_0, H_1) = \sqrt{\frac{2N_A}{m}\left[H_0 - H_1\right]}. \tag{32}$$

Unfortunately, the enthalpies are difficult to access.

The assumption of the equation (15) was that the initial stagnation enthalpy H_0 of the gas is completely converted into the forward motion. In reality, the molecules keep some finite thermal velocity α, which corresponds to the Boltzmann distribution at the residual translational temperature T, even at the end of expansion:

$$\alpha = \sqrt{\frac{2k_B T}{m}} \, . \tag{33}$$

Thermal movement α can be assigned as the velocity dispersion, which is a measure of the random molecular motion.

The expansion quality can be represented by the speed ratio S:

$$S = \frac{u_{\max}}{\alpha} \, . \tag{34}$$

It can be shown that the speed ratio S can be experimentally determined from the measured velocity distribution according to the expression:

$$S \approx 2\sqrt{\ln 2}\,\frac{v}{\Delta v} \, , \tag{35}$$

where v is the experimentally measured mean velocity of particles and Δv is full width at the half maximum of the velocity distribution. Typical values of S range from 10 to 100, which mean that the directional velocity of particles in the beam, u_{max}, is about one or two orders of magnitude larger than the random thermal molecular motion α.

Molecular clusters are often prepared by so-called seeded expansions. This method is generally used for achieving a high speed ratio of both clusters as well as molecules. The particles, which should form the clusters, are added in small concentrations c (<10%) to the expansion of a buffer gas, typically rare gases atoms (He, Ar), or small molecules such as N_2. The velocity and speed ratio is determined by the dominant component in the mixture, i.e. the buffer gas. By this method, it is possible to reach a high velocity of particles u and it results in a high speed ratio S, which denotes high-quality expansion.

If the molecular beam is prepared by the seeded expansion, then the mass m in the relation (30) has to be replaced by the mean mass of particles in the beam:

$$m = cm_c + (1-c)m_b \, , \tag{36}$$

where m_c is the mass of particles that would have formed the clusters and m_b is the mass of the buffer gas particles. For the mean velocity of both the buffer gas and admixed molecules in the beam, holds:

$$v(m) = \sqrt{\frac{m_b}{m}} v(m_b) \,, \tag{37}$$

where $v(m_b)$ is the mean velocity of the buffer gas without the admixed molecules.

4.1.1 Cluster formation and condensation

In this section, the formation of the clusters during supersonic expansion will be described in both a macroscopic and microscopic picture. A schematic p-T phase diagram (see Fig. 13 [18]) can be used for the explanation of the macroscopic description. The point A represents the start of the adiabatic expansion of the real gas with the stagnation conditions p_0, T_0 in the source. Consequently, the gas expands along the isentrope up to point B, where it crosses the vapor pressure curve $p_D(T)$. p_D is the vapor pressure of a plane liquid surface. The expansion continues along the isentrope up into the liquid phase region. Hence, supersaturation occurs until finally, at the point C, the gradual formation of clusters leads to the breakdown of the supersaturated state. The expansion curve returns to the equilibrium vapor pressure curve $p_D(T)$, since the expansion is heated by the released condensation.

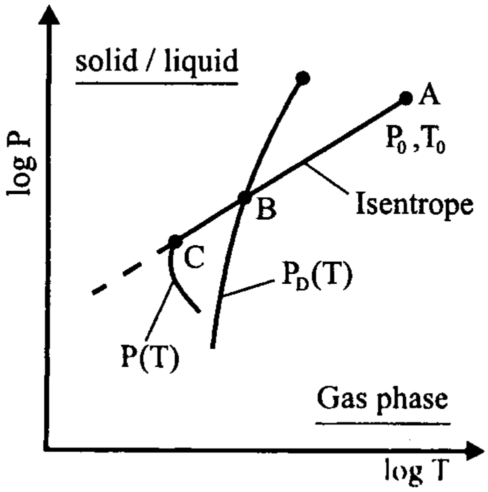

Figure 13. A schematic p-T phase diagram. $p(T)$ is the expansion curve and $p_D(T)$ is the vapor pressure curve [18].

The starting point for condensation in a microscopic picture is the dimer formation at the beginning of the supersonic expansion. Dimers, as well as larger aggregates, may already exist under the equilibrium conditions in the source. The energies of molecules at equilibrium are distributed around the average value. However, a small fraction of molecules have energies much higher than this average value. Through collisions, these molecules can participate in some processes which are unavailable for molecules with average thermal energy, such as dimer formation. During expansion, some of the collisions of two molecules (with the participation of a third molecule, for reasons of energy and momentum conservation) can lead to the dimer formation. Consequently, the dimers serve as condensation nuclei for further cluster growth. As long as the cluster number density is much smaller than monomer number density, monomer – cluster collisions mainly occur and growth of clusters results from successive accumulation of monomers. With increasing cluster number density, cluster – cluster collisions are more important for the cluster growth. Cluster formation ceases when the vapor density is too low, typically beyond a few nozzle diameters from the nozzle exit. The average cluster size and number of clusters increase with increasing stagnation pressure p_0 and aperture cross-section, but they decrease with increasing temperature T_0.

Supersonic expansion can be treated by dividing it into tree regimes [18]. However, this division is not rigorous. The first regime occurs near to the nozzle and is connected with the high pressure region of viscous flow. The collision frequencies are very high and therefore the thermodynamic equilibrium is always guaranteed. For modeling of this regime, the equation of the ideal gas can be used. The final regime of molecular flow, where only few collisions occur, is reached by rarefaction. An intermediate regime can be defined between these two regimes, where the number of collisions is still high enough to ensure translational cooling, but thermodynamic equilibrium is not guaranteed. Throughout the first two regimes, two- and many- body collisions occur and it leads to cooling, condensation, and dissociation of clusters. The increase in many-body collisions is responsible for the enhanced generation of clusters during the expansion. On the other hand, the increase in the two-body collisions helps to cool and stabilize them, because it leads to more efficient conversion of enthalpy to forward motion [25]. In other words, the two-body collisions decrease the residual translational temperature T and increase the speed ratio S. On the other hand, during the many-body collisions, which lead to the cluster formation, the condensation energy is released. This condensation energy is transferred to the random motion of all particles in the frame of the propagating beam, thus lowering the speed ratio and increasing the residual translational temperature T, while increasing the average beam velocity [25, 26].

The total number of two-body collisions Z_2, which a molecule at a centerline point ξ is going to undergo during the expansion can be estimated from:

$$Z_2(\xi) \approx \frac{\sigma(T_0) p_0 d}{T_0}. \tag{38}$$

Where $\sigma(T_0)$ is the temperature dependent cross section and d is the nozzle diameter, and it is proportional to the ratio of pressure p_0 and temperature T_0.

On the other hand, the total number of three-body collisions Z_3 is proportional to the square of the ratio of pressure p_0 and temperature T_0:

$$Z_3(\xi) \approx \frac{[\sigma(T_0)]^{5/2} p_0^2 d}{T_0^2} \tag{39}$$

The full relation for Z_2 and Z_3 can be found in [18], equations (3.104) and (3.106).

Generally, it is believed that clusters are formed during the early stages of the expansion where the pressures are still high enough. Typically, there have occurred several hundred two-body collisions and approximately ten three-body collisions after a distance of only two orifice diameters [27] in the expansion, and relatively few collisions occur afterwards. The newly born clusters formed through the many-body collisions quickly leave the region in which they were formed and continue as free particles, which can be detected and analyzed using molecular beam techniques described in [18].

The mean size of rare gases clusters can be determined from the empirical formula [28]:

$$\overline{n} = 38{,}4 \cdot \left(\frac{p_0[mbar] \cdot d_{eq}^{0{,}85}[\mu m]}{T_0^{2{,}2875}[K]} K_{ch} \right)^{\zeta} \tag{40}$$

The constant K_{ch} is characteristic for the given rare gas and is listed in Tab. 3. The exponent ζ is equal to 1,64 for rare gases expansions. The conical nozzle with the angle of divergence β = 30° and with the throat diameter d = 50 μm was used for the velocity measurements of rare gases. The equivalent nozzle diameter is given by $d_{eq} = 0{,}74 \cdot \frac{d}{tg\beta/2}$.

Table 3. The constant K_{ch} for various rare gases

Rare gas	Neon	Argon	Krypton
K_{ch} [$\mathrm{K}^{2,2875}\mathrm{mbar}^{-1}\mu\mathrm{m}^{0,85}$]	185	1646	2980

A similar empirical relation was found for the mean size of water clusters [29]:

$$\bar{n} = 11{,}6 \cdot \left(\frac{p_0[bar] \cdot d_{eq}^{0,634}[\mu m]}{10000.k_B.T_0^{2,366}[K].T_R[K].K_{ch}} \right)^{1,886} \quad (41)$$

The constant K_{ch} = 3,8417.10^{13} J^{-1}K$^{-2,366}$bar.µm$^{-0,634}$. The conical nozzle with the angle of divergence β = 30° and with the throat diameter d = 75 µm was used for the velocity measurements of water clusters. Note that the mean size $\bar{n}$ of water clusters depends also on the temperature of reservoir T_R.

At present, no rigorous theory for the description of clusters growth and prediction of the onset of condensation exist, because theoretical treatment of cluster formation is rather complicated, although several models were developed [18, 26]. Cluster growth has to take into account both the creation as well as destruction of clusters in the expansion. These processes depend on the velocity distribution in the beam, the particle density, and the collision cross-section. The achieved velocity distribution in the beam is a complex process involving numerous collisions. Probably the best conditions for studying the microscopic kinetics of homogenous nucleation are provided by free jet expansions. The measured velocity distribution and the speed ratio can tell us something about the collisions in beam and the nucleation. This topic will be the subject of the next section.

4.1.2 Velocity measurements of rare gases and water clusters

In this section, the velocity measurements of water and rare gas clusters will be introduced. It has to be mentioned that two different sources of clusters were employed. The one for producing water clusters consists of a reservoir and nozzle with independent heating. The nozzle temperature T_N was always kept at a higher value than the reservoir temperature T_R to prevent the condensation of the water molecules at the nozzle. The reservoir was filled with distilled water and heated so that water vapor filled the space above the water sheet to the nozzle. On the other hand, the cluster source for rare gases consists only of a nozzle, which can be electrically heated or cooled by liquid nitrogen, and the gas flows directly through a 6 mm swagelock tube to the nozzle.

The method of measurement is described in Sec. 3.2. The experimentally measured velocity distribution is shown in Fig. 14 for water clusters in supersonic expansion (black squares). Experimental conditions are listed in Tab. 4. This distribution is compared with the Maxwell – Boltzmann distribution of speeds at the temperature T_N = 433 K. Assuming that the nozzle and the gas are in thermal equilibrium, the nozzle temperature T_N can be made equal to the temperature of the molecules before leaving the nozzle T_0, thus the Maxwell – Boltzmann distribution is shown as:

$$f(v) = 4\pi v^2 \left(\frac{m}{2\pi k_B T_N} \right)^{3/2} \exp\left\{ -\frac{mv^2}{2k_B T_N} \right\}, \tag{42}$$

where m is the mass of the water molecule and k_B is the Boltzmann constant. The velocity corresponding to the Maxwell – Boltzmann distribution maximum v_{MB} (the most probable speed) can be derived by putting first derivative of (42) with respect to the velocity equal zero:

$$v_{MB} = \sqrt{\frac{2k_B T_N}{m}}\ . \tag{43}$$

Note that the theoretical maximal value of the supersonic expansion distribution of speeds $u_{\max}$ is twice the maximum of the Maxwell – Boltzmann distribution v_{MB} (maxima are listed in Tab. 4). It can be understood by comparing (30) and (43):

$$u_{\max} = \sqrt{\frac{\gamma}{\gamma - 1}} \cdot v_{MB} = 2 \cdot v_{MB}\,. \tag{44}$$

This conclusion holds true for each polyatomic gas, where $\gamma = 4/3$. The factor 2 in the eq. (44) change to the values 1,87 for a diatomic gas ($\gamma = 7/5$) and 1,58 for a monoatomic gas ($\gamma = 5/3$). The equation (44) holds exact for theoretical velocities of supersonic expansion $u_{\max}$ not for the experimental ones v. Nevertheless, it is worth noting that in the present case of water expansion v/v_{MB}= 2.05 and the relation (44) is very well satisfied for the experimentally measured velocity.

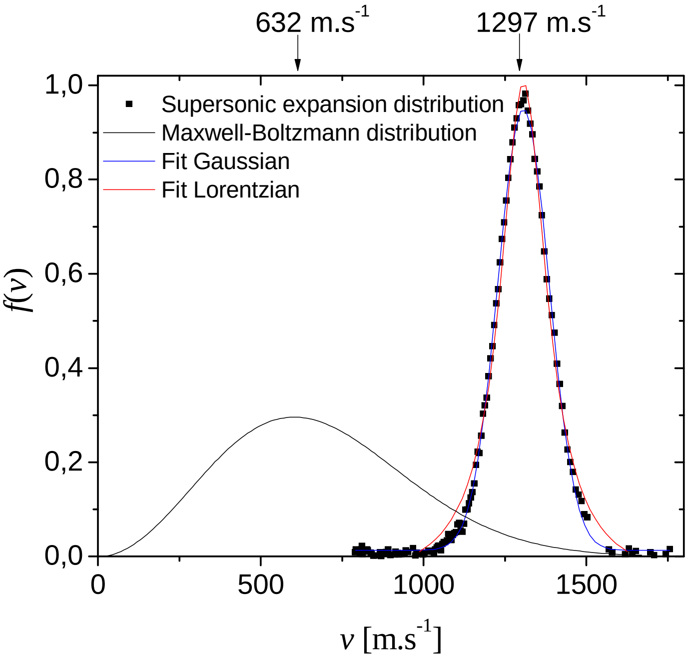

Figure 14. Comparison of the calculated thermal Maxwell – Boltzmann velocity distribution and the measured velocity distribution in a supersonic expansion of water vapor at the same temperature of 433 K. In the case of supersonic expansion, this corresponds to the temperature of the nozzle. The arrows at the top indicate the maximum of the corresponding distribution. The velocity distributions are normalized on the same area.

The full width at half maximum (FWHM) for supersonic expansion is $\Delta v = 180$ m.s^{-1}, while the FWHM for the Maxwell – Boltzmann distribution is around 700 m.s^{-1}. Because the distribution of speeds in a supersonic expansion is very narrow, we can say that the speeds of the molecules are approximately equal (at least in comparison with their Maxwell – Boltzmann distribution). The experimentally measured velocity distribution was fitted by Gaussian (blue line) and Lorentzian (red line) functions. Note, that Gaussian function more accurately fits the measured points in comparison with Lorentzian function, especially in the region of velocities around 1100 m.s^{-1}, and also around 1500 m.s^{-1}. Thus, the velocity distribution of the supersonic expansion exhibits the shape of a Gaussian distribution.

Table 4. Shows the expansion conditions of water molecules: T_N is the temperature of the nozzle, T_R is the temperature of reservoir, $u_{\max}$ is the theoretical velocity counted from (30), v is the experimental velocity established as the velocity corresponding to the maximum of supersonic expansion distribution, v_{MB} is the velocity corresponding to the maximum of the Maxwell – Boltzmann distribution calculated from (43), and S is the speed ratio evaluated from (35). T is the residual temperature corresponding to the thermal motion of the water molecules in the molecular beam calculated from (33) and (34).

T_N [K]	T_R [K]	$u_{\max}$ [m.s^{-1}]	v [m.s^{-1}]	v_{MB} [m.s^{-1}]	S	T [K]
433	393	1264	1297	632	12	13

The flow velocities of neon, argon, krypton and water clusters measured at different nozzle temperatures T_N are plotted in Fig. 15. These flow velocities correspond to the maximum of the speed distribution, similar to that one pictured at Fig. 14 (black squares). The expansion pressure for velocity measurements of all rare gases was $p_0 = 4$ bar, while for water the pressure p_0 depends on the reservoir temperature T_R. For comparison, the corresponding theoretical dependences (lines) calculated according to the relation (30) are shown. The line is solid if the rare gas or water is in the gas phase and dashed if it is below the normal boiling point T_B. The values are also listed in Tab. 5. The relation (30) should be valid for rare gases far away from the critical point, where the value $\gamma = 5/3$ for ideal monatomic gas is almost the same as the temperature and pressure dependent capacity ratio $\gamma(T_0, p_0)$. In Tab. 5 the critical temperatures T_c and pressures p_c are also listed and it has to be mentioned that our measurement takes place far away from critical point, especially $p_0 \ll p_c$.

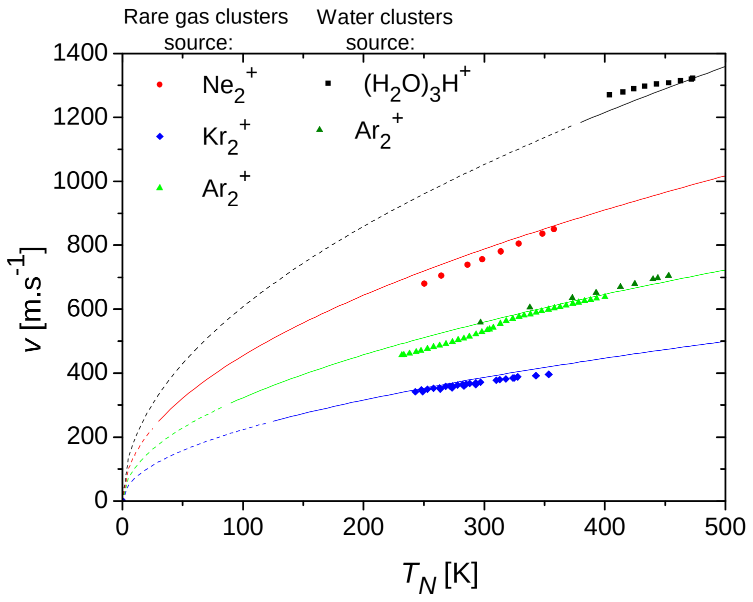

Figure 15. Terminal maximal flow velocities of argon, neon, krypton and water (scatters) and appropriate theoretical dependences (lines) calculated according to the relation (30). The line is solid if the rare gas or water is in the gas phase, and dashed if it is below the normal boiling point T_B.

Note that we detected rare gases dimer and water clusters trimer. However, these fragments originate from much larger neutral clusters (mean cluster size $\overline{n}$ = 40 – 120 for water clusters). The velocities correspond to the neutral clusters and the ionized fragments arise after electron ionization just before the quadrupole.

Table 5. Properties of critical points and normal boiling point of water and rare gases

	Ne	Ar	Kr	Water
Critical temperature T_c [K]	44,5	150, 7	209,5	647,1
Critical pressure p_c [bar]	26,8	48,6	55,3	220,6
Normal boiling point T_B [K]	27,1	87,3	119,7	373,1

The experimental velocities of neon, argon and krypton produced from source of rare gas clusters are somewhat lower than the theoretical velocities across the entire temperature range. On the other hand, the experimental velocities of water clusters produced from the water cluster source are higher than corresponding theoretical ones. Therefore, the velocity measurement of argon clusters was also performed with the water cluster source for comparison (dark green triangle in Fig. 15). These experimental velocities lie also slightly above their theoretical values. This might suggest that a part of the discrepancy between the theoretical and experimental velocities could be caused by the properties of the cluster sources (e.g. the nozzle diameter, the temperature calibration). However, it will rather be shown that the property of water expansion causes velocities that are above the theoretical ones, as opposed to rare gas expansions. The discrepancy between argon cluster velocities produced from the two different sources could be probably caused by different temperature calibrations of these two sources. It seems that the calibration of temperature between these two sources is shifted by about 20 K. This number can be achieved, if we require agreement between argon cluster velocities produced from a water cluster source and a rare gas source. However, yet another effect can play a role in the explanation of this discrepancy between argon clusters velocities produced from two different sources.

The conical nozzle diameter of the water cluster source was 75 μm, while the one of the rare gas cluster source was only 50 μm. In the section 4.1.1, it was noted that the average cluster size and the number of clusters increases with increasing aperture cross-section. Therefore, more condensation energy is released and this energy can increase the forward velocity of the clusters. This condensation energy released during expansion from a water cluster source can cause the argon clusters to reach higher velocities than those from the rare gas source. The mean cluster sizes $\bar{n}$ of argon clusters at various nozzle temperatures for two nozzle diameters (50 μm and 75 μm) is depicted in Fig. 16.

The fact that the experimental velocities of rare gases lie below the theoretical is in agreement with the assumption that the initial stagnation enthalpy H_0 of the gas is completely converted into directed translational motion, which was used for deriving the equation (30). In other words, theoretical velocities are the maximal ones, which can be achieved only if the entire initial enthalpy H_0 is changed into the kinetic energy. However, some energy remains in the random molecular motion, which can be characterized by velocity dispersion α or by translational temperature T. Therefore the maximal velocities cannot be reached without any additional (e.g. condensation) energy, which is released during the formation of clusters.

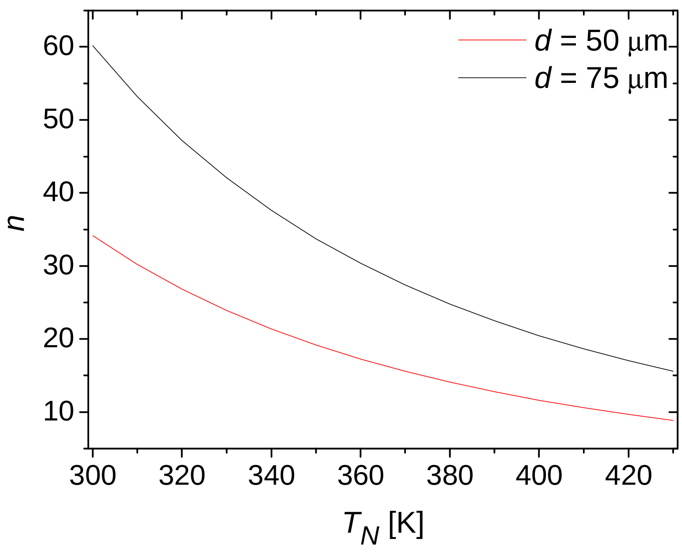

Figure 16. The mean cluster sizes $\overline{n}$ of argon clusters at various nozzle temperatures for two nozzle diameters 50 µm (the rare gas cluster source) and 75 µm (the water cluster source).

Even if the temperature calibration is taken into account, the water velocities, at least below a nozzle temperature of 460 K still lie above the theoretical values. This fact is depicted in Fig. 17, where is shown the measured velocities (black circles) and the same velocities shifted about 20 K (blue circles). This shift of velocities is depicted there for illustration and it is not claimed that the shift of 20 K is correct. Moreover, the value 20 K was achieved, provided that the temperature calibration of rare gases cluster source was correct. It can be clearly seen from Fig. 18 that below the temperature of 460 K bigger clusters are formed than those at higher temperature. In other words, the mean cluster size is larger for smaller nozzle temperatures T_N. Therefore, more condensation energy is released and this energy can increase the forward velocity of the water clusters. This condensation energy is not involved in the energy balance (24), and hence this energy can cause the experimental velocities of water clusters to lie above the theoretical ones.

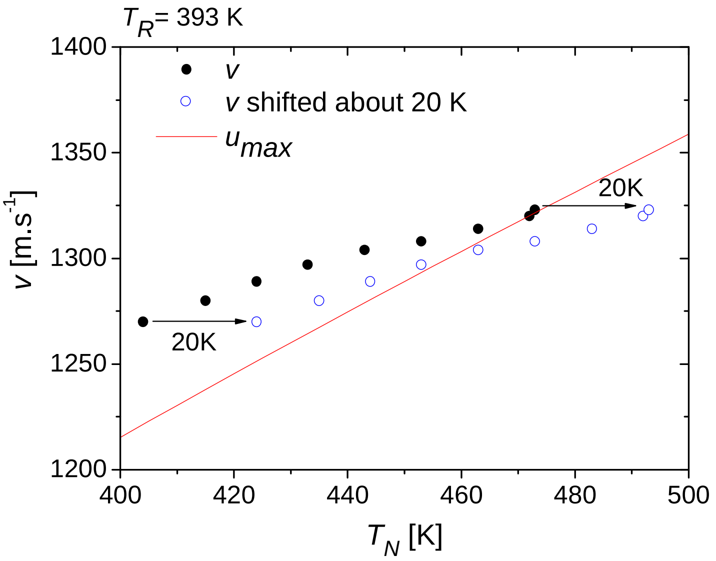

Figure 17. The water velocities at various nozzle temperatures T_N (black circles) and the same velocities shifted to higher temperature about 20 K (blue circles). The reservoir temperature was kept at constant value (T_R = 393 K), which corresponds to the pressure p_0 = 1,9 bar.

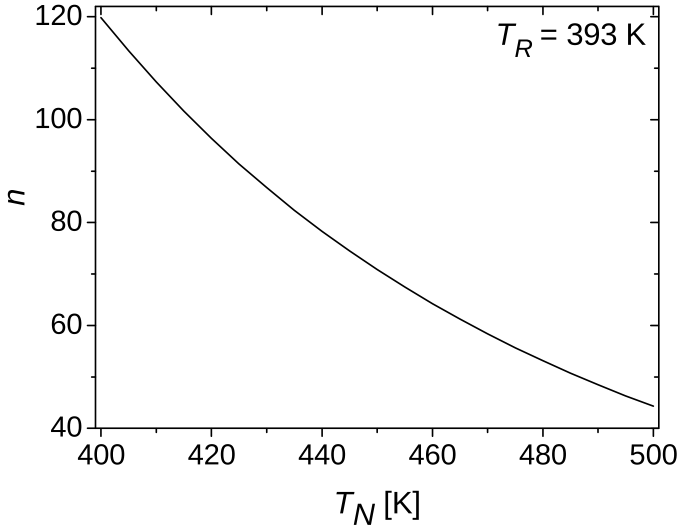

Figure 18. Mean cluster size $\overline{n}$ calculated from eq. (41) at various nozzle temperatures T_N and a constant reservoir temperature T_R.

In the case of the water cluster source, the nozzle temperature T_N was kept constant, and only the reservoir temperature T_R was varied. These experimental velocities, compared to the theoretical ones, are depicted in Fig. 19. The experimental velocities v of water clusters are not constant as should correspond to their theoretical velocities $u_{max}(T_N)$, but instead lie above these theoretical values and exhibit an upward trend as the reservoir temperature T_R increases. It has to be stressed that this dependence represents only about 7% of the measured values over the entire measured temperature region ($\Delta T_R = 30$ K). It can be easily understood by noting that the mean cluster size $\bar{n}$ increases as the reservoir temperature T_R goes up (Fig. 20). This is true in spite of the fact that there is a reciprocal proportion between the mean cluster size $\bar{n}$ and the reservoir temperature T_R, which appears in the eq. (41) through the equation of state to evaluate the density of particles. However, an increasing value the reservoir temperature T_R increases the pressure p_0 and consequently the mean cluster size $\bar{n}$. Therefore, more condensation energy is released into the forward velocity of the water clusters, and it is justified that the experimental velocities of the water clusters lie above the theoretical ones.

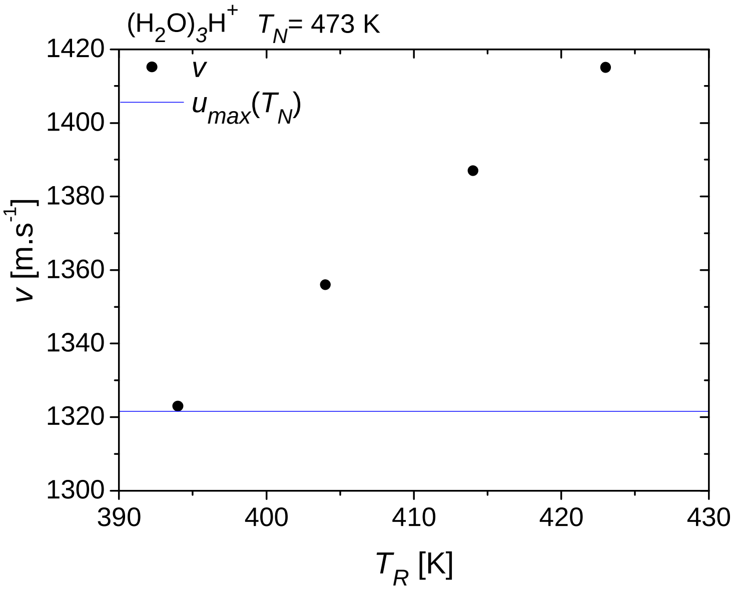

Figure 19. Dependence of water cluster velocities on the temperature of the reservoir T_R. The theoretical velocity $u_{max}(T_N)$ supposes that $T_0 = T_N$ in the eq. (30).

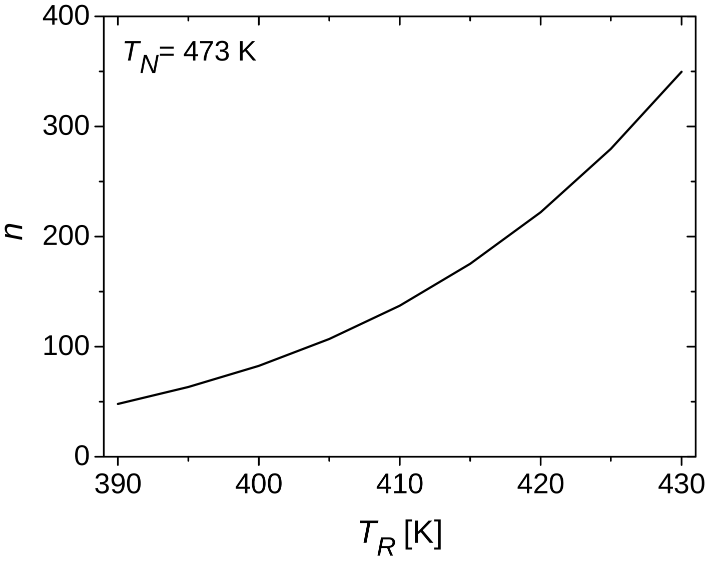

Figure 20. Mean cluster size $\overline{n}$ calculated from eq. (41) at various reservoir temperatures T_R and a constant nozzle temperature T_N.

The dependence of pressure p_0 and mean cluster size $\overline{n}$ on the reservoir temperature T_R is also listed for four experimental velocities in Tab. 6. Note that mean cluster size $\overline{n}$ decreases as the nozzle temperature T_N increases (Fig. 18), but is increasing as the reservoir temperatures T_R increases (Fig. 20).

Table 6. Pressure p_0 and mean cluster size $\overline{n}$ at four reservoir temperatures T_R corresponding to the experimental velocities depicted in Fig. 19.

T_R [K]	p_0 [bar]	$\overline{n}$
394	2,0	60
404	2,7	102
414	3,6	167
423	4,6	255

The explanation of the water clusters velocities in dependence on the reservoir temperatures T_R given above is supported by the measurement of the argon cluster velocities with respect to the reservoir temperatures T_R. It can be clearly seen from Tab. 7

that the argon cluster velocities do not depends on the reservoir temperature T_R within the experimental error. It is in agreement with the fact that pressure p_0 of argon does not depend on the reservoir temperature T_R, since argon flows through the reservoir while water is closed in this reservoir and the saturated vapor pressure depends on the temperature.

Table 7. Experimental velocities of argon clusters at various reservoir temperatures T_R.

T_R [K]	v [m.s^{-1}]
278	704
393	706
402	705
412	706
423	705

Another important element which can influence the quality of expansion, and thus the cluster velocity, is the nozzle-skimmer distance. The dependencies of the velocity v, speed ratio S of argon clusters at constant pressure, and temperature on the nozzle-skimmer distance are shown in Fig. 21. This measurement was done using the rare gas cluster source. Note that there is a region of the nozzle-skimmer distances, from about 30 to 45 mm, where the velocity v of argon clusters reaches maximal values. The best quality expansion is also achieved in this region, since the speed ratio S exhibits its highest values here. The velocity v and speed ratio S decrease as the nozzle-skimmer distance becomes shorter below 30 mm as well as larger than 45 mm. When the nozzle-skimmer distance decreases, the particles in the beam collide with much more of the reflected particles from the skimmer. They are slowed down by these collisions, which are in an agreement with the decreasing velocity for decreasing nozzle-skimmer distance in Fig. 21. Since each particle undergoes a different number of collisions, and they lose different amount of energy, the particles become dispersed. Consequently, the full width at half maximum Δv of the velocity distribution grows. Therefore, the speed ratio S rapidly decreases as the nozzle-skimmer distance decreases. On the other hand, a different explanation has to be given for the decreasing speed ratio and velocity at higher nozzle-skimmer distances, which is as follows: the path, which the particles in the beam have to overcome, gets larger as the nozzle-skimmer distance increases. Particles undergo more collisions with background molecules during this longer distance, and therefore the velocity, as well as speed ratio, decreases with increasing nozzle-skimmer distance.

The velocity measurement of rare gases was performed at the nozzle-skimmer distance of 24 mm. The velocity at this position is about 1,5% lower than the maximal value. The best expansion quality was reached at a nozzle-skimmer distance of 40 mm, where the speed ratio S reaches its maximal value 15,1. It is in coincidence with the maximal velocity value.

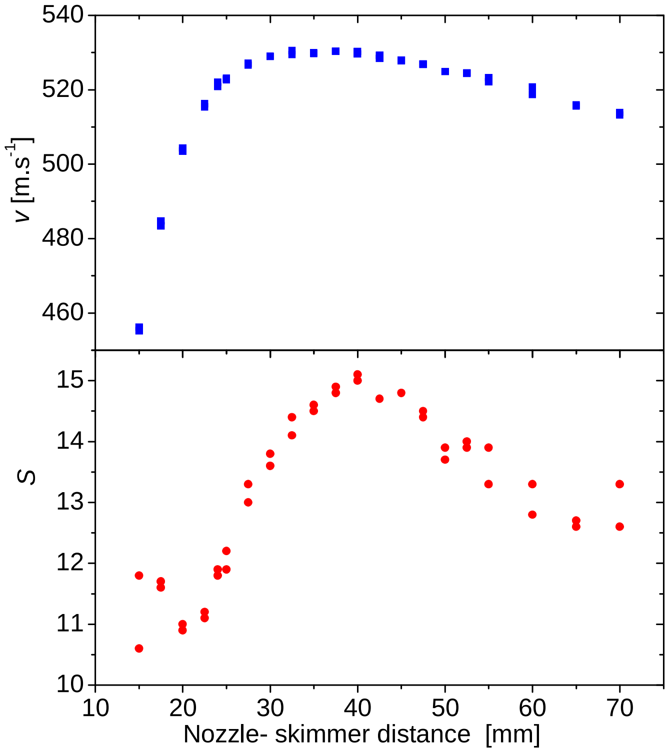

Figure 21. Velocity v and speed ratio S of argon dimers at a constant pressure and temperature for different nozzle-skimmer distances.

The experimental, as well as theoretical velocities, of neon, argon and krypton clusters are shown again in Fig. 22(a). There are also shown the deviation of the experimental velocities v from the theoretical $u_{\max}$ (b), speed ratio S (c) and residual temperature T (d) calculated from equations (33) and (34). It ought to be mentioned that these results are not fully understood yet. However, several remarks can be made.

The relative errors between the experimental and theoretical velocities of neon, argon and krypton reach values 1,2 - 5,7 %, 0,7 - 7 % and 0,7 – 3,8 %, respectively. Note also, that in the case of argon, the relative errors are only about 1% at higher temperatures than 320 K. On the other hand, they reach 5-7% below 300 K. Larger deviations between experimental and theoretical velocities correspond to lower values of the speed ratio *S*, and the smaller deviations correspond to higher values of the speed ratio *S*. In other words, the higher quality expansion (characterized by high *S*) leads to better agreement between the experimental and theoretical velocities. This fact also holds true for krypton. However, it disagrees with the velocity measurements of neon clusters. This distinction between argon and krypton on one side, and neon on the other could be rationalized by different mean cluster sizes $\bar{n}$. They are depicted in Fig. 23 for the temperature region corresponding to the velocity measurement of the given rare gas. Note that the mean cluster size $\bar{n}$ for argon and krypton are in the tens or even hundreds, while it is below three for neon.

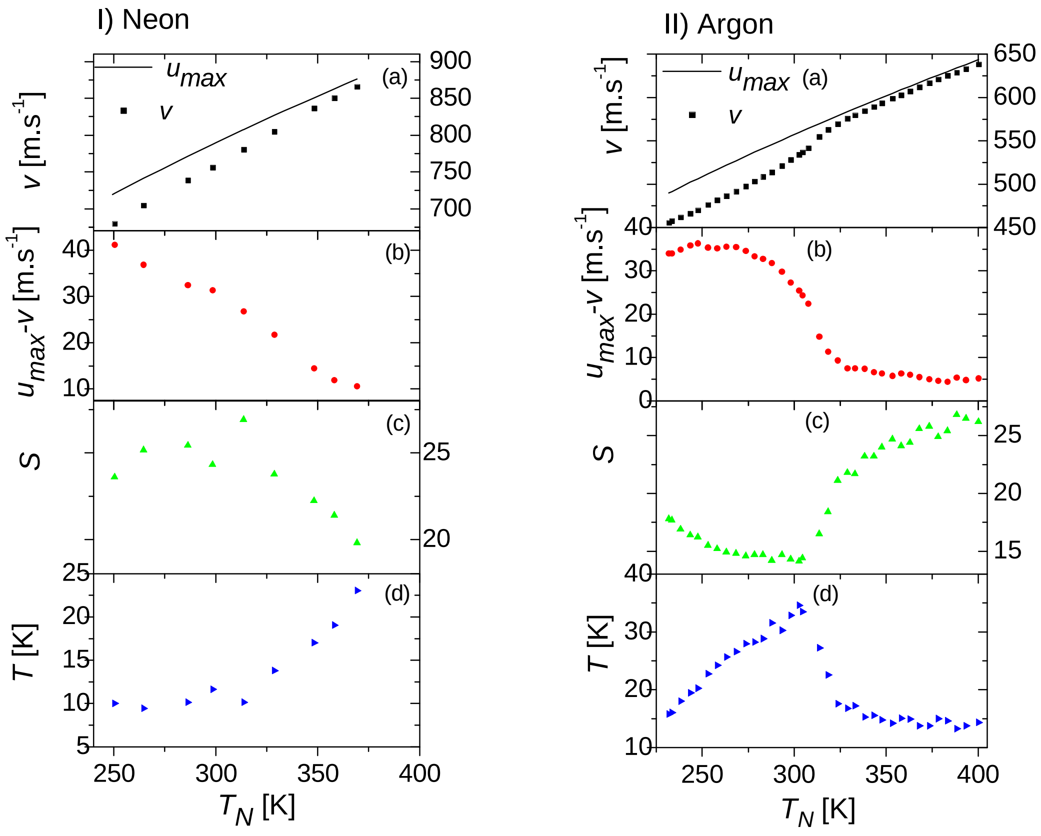

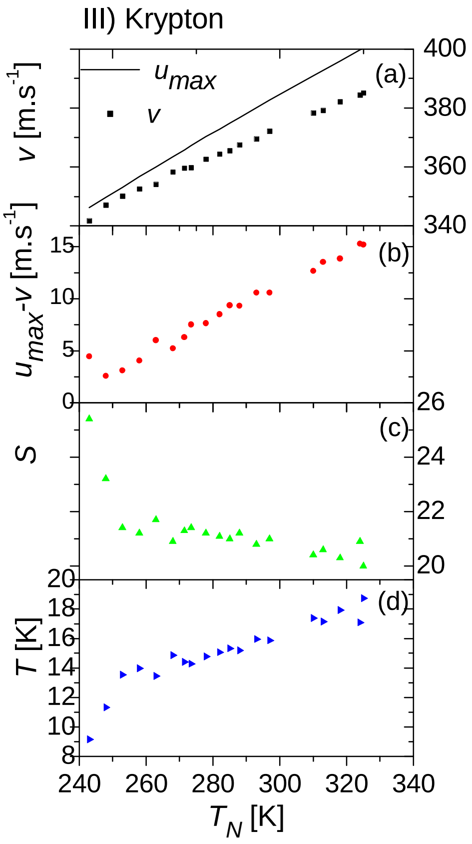

Figure 22. The experimental and theoretical velocities of neon (I), argon (II), and krypton (III) clusters (a). The deviation of the experimental velocities from theoretical ones (b), the speed ratio S (c) and residual temperature T (d).

It can be also seen from Fig. 22(IId) that a residual translational temperature T steadily increases at first with the increasing nozzle temperature T_N. This increase can be explained by the many-body cluster forming collisions. The condensation energy which increases the residual temperature T is released during these collisions. The residual translational temperature T reaches its maximal value around 300 K, then decreases and remains approximately constant above 350 K. This decrease could be caused by the two-body collisions, the effect of which dominates in this region since the number of two-body collisions is indirectly proportional to the stagnation temperature T_0 (in equilibrium $T_0 = T_N$) according to the eq. (38). There are no similar maxima in the residual temperature T in the case of neon or krypton. It seems that this maximum could be found outside the investigated temperature region.

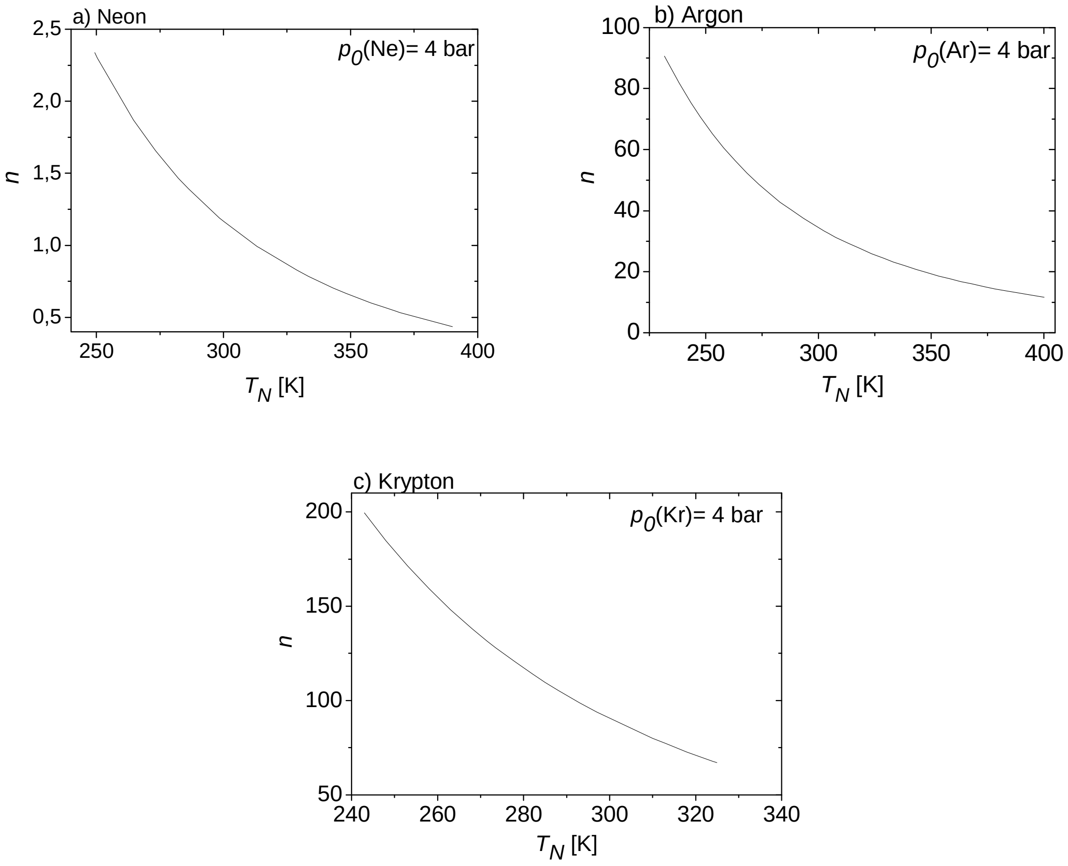

Figure 23. Mean cluster sizes $\bar{n}$ calculated from eq. (40) as a function of the nozzle temperature T_N at the constant pressure $p_0 = 4$ bar for neon (a), argon (b) and krypton (c).

The dependence of the argon cluster velocity on the stagnation pressure has also been measured. The results are depicted in Fig. 24 at a constant stagnation temperature of T_N = 248 K. The mean cluster sizes $\bar{n}$ at corresponding pressures are depicted in Fig. 25. Note that up to stagnation pressures of p_0 = 2 bar, the velocity decreases with increasing stagnation pressure. Christen and Rademann [23, 30] explain this decline by the drop of temperature- and mainly pressure- dependent heat capacity ratio $\gamma(T_0, p_0)$. This fact can be true. However, there is a need to derive right equation for the temperature- and pressure-dependent heat capacity ratio $\gamma(T_0, p_0)$ instead of equation (31). Above the stagnation pressure of p_0 = 2 bar, the argon velocity, as well as speed ratio, increase monotonically with increasing pressure. This can be rationalized in terms of the condensation. With increasing stagnation pressure, the particle density and thus the number of two-body collisions increases. It leads to a more efficient conversion of enthalpy to forward motion and thus to the increasing velocity. Also the monotonic increase of the speed ratio S can be a consequence of the increased number of two-body collisions [25].

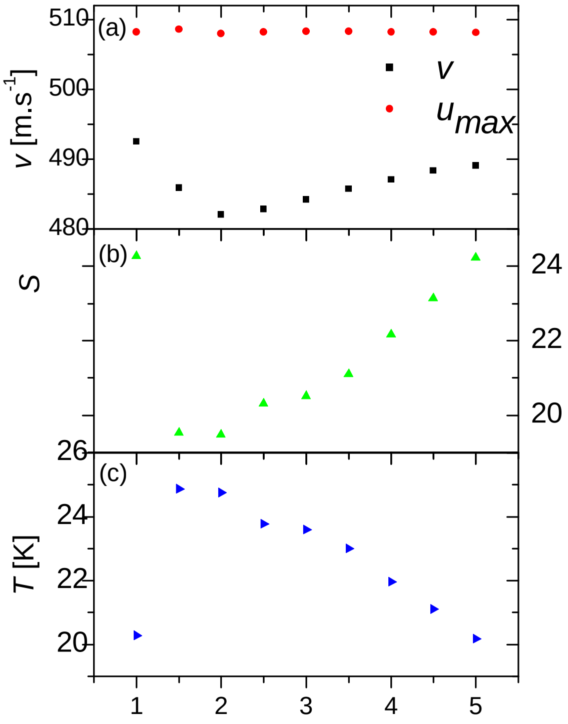

Figure 24. Velocity of a supersonic beam at a constant nozzle temperature (T_N = 248 K) for the argon clusters in dependence on the argon pressure p_0 (a). Speed ratio S (b) and translational temperature (c) at various stagnation pressures p_0.

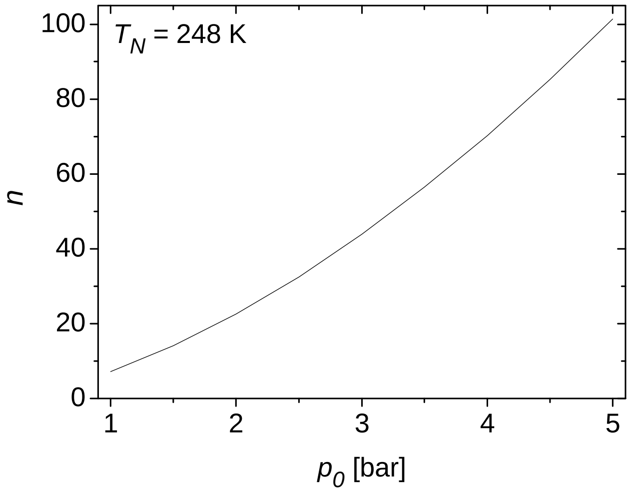

Figure 25. Mean cluster size $\overline{n}$ calculated from the eq. (40) at various stagnation pressures p_0 and a constant nozzle temperature T_N for argon.

To summarize this discussion about rare gas cluster velocities, several notes should be made. The fact that the experimental velocities of rare gases lie below the theoretical is in agreement with assumption that the initial stagnation enthalpy H_0 of the gas is completely converted into directed translational motion used for deriving the equation (30). This assumption is not satisfied, since some residual temperature T always remains.

In spite of this fact and another simplification (specifically, a heat capacity c_p is independent of the temperature during deriving the equation (30)), this equation gives the velocities of rare gases correctly within 0,7 – 7 % from the experimental values. Moreover, it even describes the velocity of water clusters correctly within 1- 4 % despite the fact that water can be hardly considered as an ideal gas. This demands the assumption of temperature independent heat capacity c_p. This agreement is satisfactory for most purposes in our experiments, and therefore the velocity measurements are not always necessary

It ought to be mentioned that the requirement of complete conversion of the initial stagnation enthalpy H_0 of the gas into directed translational motion overestimates the theoretical velocities u_{max}. On the other hand, the condensation energy, which is not involved in the energy balance (24) during deriving equation (30), caused that theoretical values u_{max} are underestimated. Thus, these two facts can counterbalance each other to a large extent, and therefore the equation (30) describes the actual velocities correctly within a few percent.

4.2. Photodissociation in $(HBr)_n$ clusters

The photodissociation process of individual molecules and molecules in clusters has been already generally discussed in the section 2.4. The investigation of the photodissociation in cluster environments is the major experiment on our apparatus. Here, it will be first illustrated on a well studied example of $(HBr)_n$ cluster photodissociation. Further in Sec. 5.1 and 5.2, the photodissociation of HI and HNO_3 molecules on large water clusters will be discussed.

The photodissociation of $(HBr)_n$ clusters was previously studied on our apparatus in great detail [12, 13, 31]. Therefore the measurement of $(HBr)_n$ clusters serves for calibration purposes of the apparatus, which mainly consist of laser alignment to intersect the molecular beam in the right position with the two laser beams and for overall verification of the correct function of the particular parts of the apparatus. This calibration with $(HBr)_n$ clusters was repeated several times before all the results in this work were achieved.

Besides, the principle of the photodissociation experiment can be well understood and nicely explained with the example of $(HBr)_n$ cluster photodissociation. The typical spectra are shown and explained here.

The $(HBr)_n$ clusters were prepared by seeded expansion (Sec. 4.1) with 5% of HBr in the argon buffer gas through the conical nozzle. The expansion conditions are listed in Tab. 8. To increase the cluster formation, the nozzle was cooled down to 258 K. The mean size of these clusters has been determined earlier in a scattering study [13] and for our expansion conditions it is approximately $\overline{n} \approx 4$.

Table 8. Expansion conditions

Nozzle diameter d [μm]	60
Opening angle β [°]	30
Nozzle temperature T_N [K]	258
Expansion pressure p_0 [bar]	1,5
Laser intensity – 243nm [J/pulse]	2,9
Laser intensity – 193nm [J/pulse]	90
U_a/U_b [V]	50/41,34
WMTOF extraction field E_s [V.cm^{-1}]	7,9
Mean cluster size $\overline{n}$	≈ 4

Fig. 26 shows the time-of-flight spectra of an H-fragment (a) with 243 nm laser pulses and (b) with 193 nm laser pulses. In the case of the photodissociation at 243 nm (Fig. 26(a)), the black arrows indicate the H-fragments flight times corresponding to the photodissociation of HBr to the ground state of Br (full lines) and to the excited state of Br^* (dashed lines). These peaks are also present in the photodissociation with 193 nm laser pulses in Fig. 26(b) since the laser pulse at 243 nm was used for (2+1) REMPI of H-fragments that is necessary for the detection of the H atoms. Moreover, the peaks corresponding to the photodissocition at 193 nm are present in Fig. 26(b); they are denoted by blue arrows. Thus both lasers are present in the interaction region and part of the clusters is dissociated by the 243 nm laser and part by the 193 nm. All these peaks correspond to the *direct cage exit* of the H-fragments, which did not lose any kinetic energy in the collisions with other molecules of $(HBr)_n$ cluster.

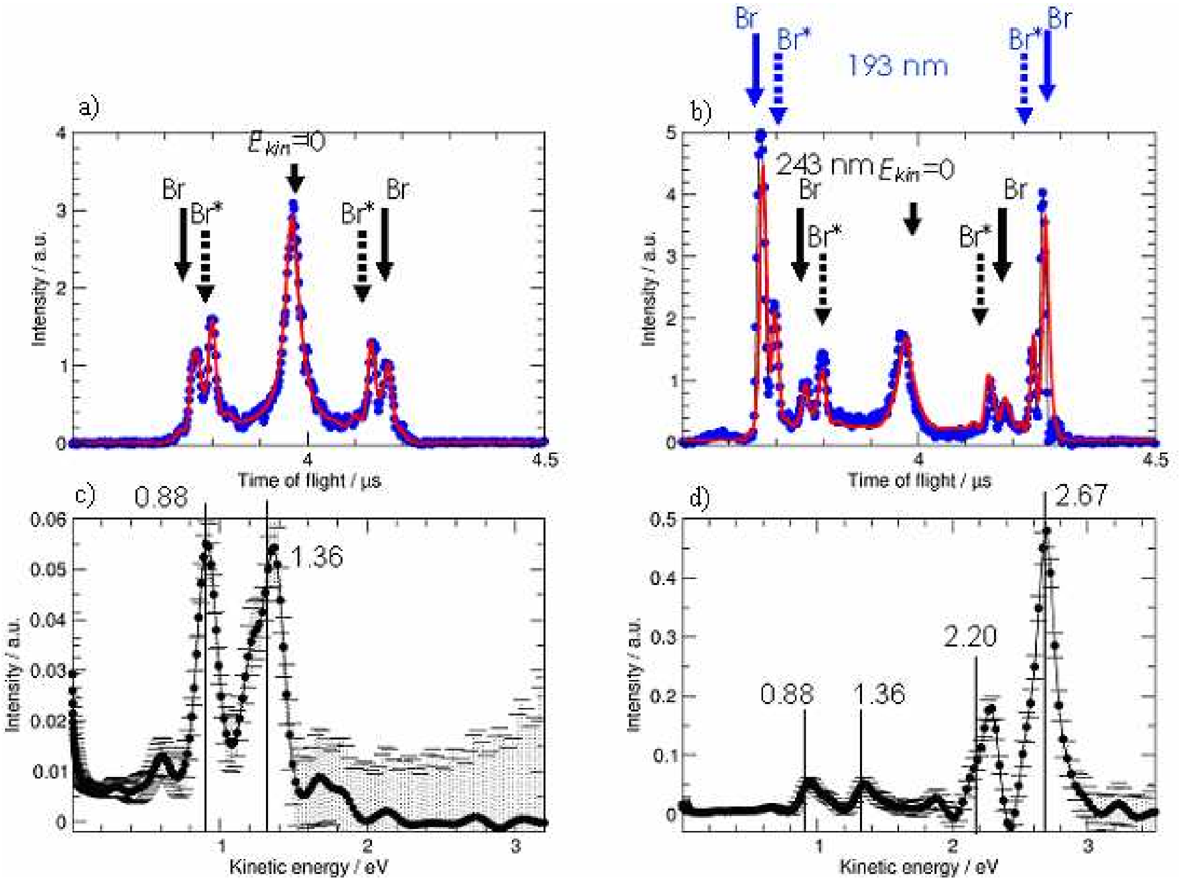

Figure 26. Time-of-flight spectra of the measured H-fragments from photodissociation of $(HBr)_n$ (a) with 243 nm laser pulses and (b) with 193 nm laser pulses. The arrows indicate the positions of the peaks corresponding to the photodissociation of HBr to the ground state of Br (full lines) and to the excited state of Br^* (dashed lines) at 193 nm (blue arrows) and at 243 nm (black arrows). The middle arrow indicates peak corresponding to H-fragments with zero kinetic energy. Below each of these, TOF spectra are plotted appropriate kinetic energy distributions of H-fragments (c, d). The lines indicate theoretically calculated positions of the appropriate peaks. The polarization of the laser was 0°.

Note that there are always two peaks corresponding to the photodissociation of HBr to the ground state of Br ($^2P_{3/2}$) and other two peaks corresponding to the excited state of Br^* ($^2P_{1/2}$). The reason of the appearance of these double peaks will be explained on the basis of Fig. 27. There is schematically shown a picture of the photodissociation of HBr molecule in the WMTOF spectrometer and corresponding schematic TOF spectra. With a linearly polarized light with the polarization vector parallel to the WMTOF axis, and for molecular excitation, with the transition moment parallel to the molecular axis, the HBr molecule can be dissociated in two orientations: with H atom pointing towards the detector (Fig. 27(a)) or in the opposite direction (Fig. 27(b)). If the H-fragment starts in the direction towards the detector, it arrives earlier than the fragment starting in the other direction, which has to be turned around (after ionization) by the weak electric field. Thus the two hydrogen atoms starting in opposite directions result in the two peaks in the TOF spectrum. The time (distance) between the two peaks corresponds to the energy released in the photodissociation process.

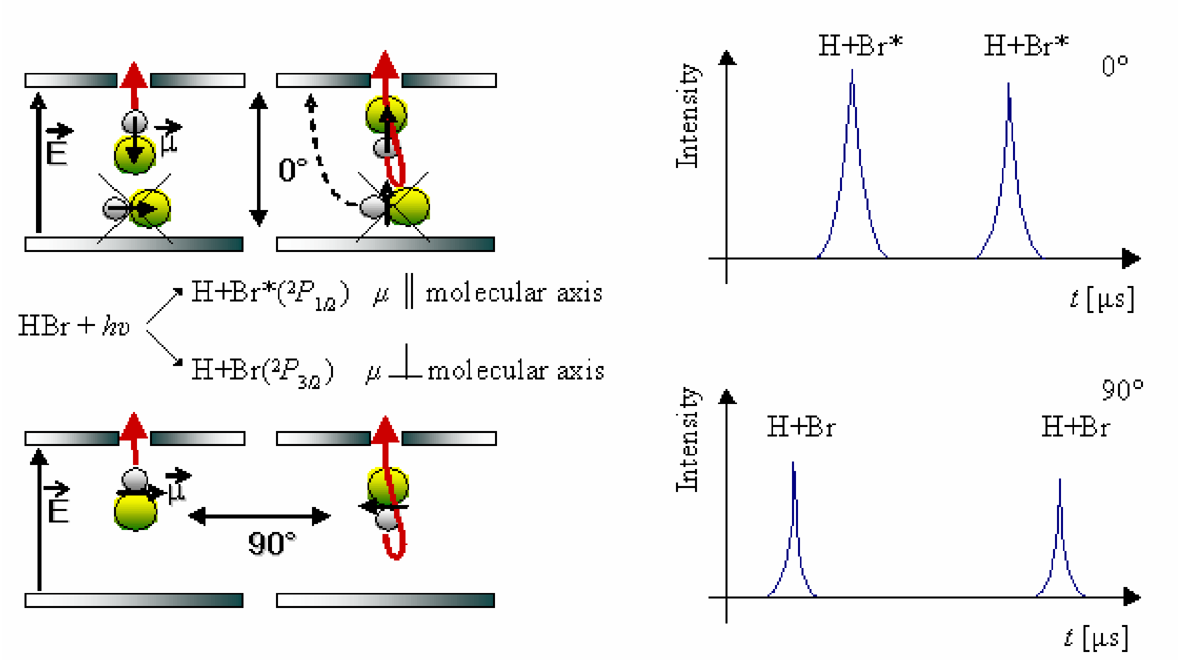

Figure 27. The schematic picture of the photodissociation of an HBr molecule in the WMTOF spectrometer (left) and corresponding schematic TOF spectra (right), which could be obtained for the bare molecule.

As has been already mentioned, the HBr molecule has two photodissociation channels. One channel corresponds to the formation of Br in the excited spin – orbit state Br^* ($^2P_{1/2}$), the other one to the ground state Br ($^2P_{3/2}$). The transition moment μ is parallel (perpendicular) with the axis of the molecule for the excitation to the states correlating with the dissociation into Br^* (Br). Therefore, if the laser is oriented parallel (0°) to the axis of WMTOF spectrometer, then H-fragments from molecules, which were oriented parallel to the axis of the WMTOF spectrometer, and their excited states, to which the transition proceeds have the parallel transition moment μ, will arrive to the detector. Thus the products of the channel, upon formation of Br^*, will be detected. On the other hand, the molecules oriented perpendicular to the axis of the WMTOF spectrometer and leading to the excited state with parallel transition moment μ will not be dissociated at the given laser polarization. The molecules oriented perpendicular to the axis of the WMTOF and leading to the excited state with the perpendicular transition moment μ can be dissociated, but do not reach the detector because they have the component of the velocity perpendicular to the axis of the WMTOF. At the perpendicular laser polarization (90°), the H-fragment from HBr leading to the excited state with transition moment μ perpendicular to the axis of the molecule will be detected, e.g. the products of the channel leading to the Br fragments.

The peaks denoted by Br^* correspond to the generation of the spin orbit excited state of a Br atom. Thus a part of the available energy goes into the Br spin orbit excitation, and therefore less energy remains for H-atom kinetic energy. Thus the peaks in the TOF spectrum are closer together than the peaks for the Br ground state.

The arrows in the middle of each TOF spectra in Fig. 26 indicate *cage effect,* i.e., the H-fragments which have been stopped after the dissociation by the solvent molecules to zero kinetic energy and then extracted by the field towards the detector. Thus this peak can be present only for the dissociation in the clusters. The H-fragments with part of their initial kinetic energy can be found between the zero kinetic energy peak and peaks corresponding to *direct cage exit*. These H-fragments correspond to *delayed cage exit* (see section 2.4).

In the 193 nm spectrum (Fig. 26(a)) nearly all of the structure originates from the dissociation with 243 nm laser pulse (Fig. 26(b)), which was used for detection of the hydrogen atoms, except for the peaks corresponding to the *direct cage exit* channel denoted by blue arrows. These processes dominate the spectrum and maximum intensity appears at the position corresponding to the generation of Br in its ground state. Note that peaks corresponding to the photodissociation of HBr into the ground state of Br are lower than the one corresponding to the formation of the Br^* at the laser wavelength 243 nm. The reason is that the laser at 243 nm was polarized in the parallel direction (0°). At this wavelength and polarization orientation the photodissociation channel into the spin- orbit state Br^* ($^2P_{1/2}$) dominates. Actually, there could not be detected any H-fragments corresponding to the photodissociation into the ground state Br ($^2P_{3/2}$) in the bare molecule, although they are still dissociated. These H-fragments do not reach the detector, because they have the component of the velocity perpendicular to the axis of the WMTOF. However, these H-fragments can be detected in the cluster environment, because they can be directed to the detector by elastic collisions with the components of clusters. Therefore, there are peaks in Fig. 26(a) corresponding to the photodissociation into the ground state Br ($^2P_{3/2}$). On the other hand, the peaks corresponding to the formation of the ground state Br ($^2P_{3/2}$) are higher than peaks corresponding to the Br^* ($^2P_{1/2}$) at 193 nm, because the laser at 193 nm is unpolarized and the branching ratio [Br*]/[Br]~0.15-0.20.

The TOF spectra can be converted into the kinetic energy distributions (KED) of the hydrogen atoms. These KED spectra are plotted below corresponding TOF spectra in Fig. 26(c, d). This conversion includes the simulation of the particle trajectories, which was carried out considering the molecular beam data, the WMTOF geometry, parameters of the photodissociation process, the finite interaction volume etc. The Monte Carlo simulation program is a part of the standard evaluation procedure of our experiment. It should be noted that the detection probability of slow fragments is significantly higher than the detection probability of the fast ones, which can more easily escape the angular acceptance of our detector. That is the reason why the detection probability is a steep function of the fragment kinetic energy, and high zero kinetic energy peak in the TOF spectra is much less pronounced in the corresponding KED (see the region near zero kinetic energy in KED).

The theoretical positions of peaks corresponding to *direct cage exit* can be calculated from equation (2) for the HBr molecule. For *direct cage exit* it holds that $E_{clu} = 0$. The internal energy of H atoms E_{int} (H) = 0 for the reasons discussed in section 2.4. As was mentioned in section 2.1, the clusters are an efficient heat bath and all rotational and vibrational energy of HBr is taken away by the argon atoms of the buffer gas, therefore E_{int} (HBr) = 0 and finally, E_{kin} (Br) ~ 0 follows from momentum conservation, because the Br atom is much heavier than H. Calculated kinetic energies of H-fragments are listed in Tab. 9. These energies are also labeled in Fig. 26(c, d) and they correspond to the peak positions within the experimental errors.

Table 9. Calculated kinetic energy of H-fragments corresponding to the dissociation of HBr to the Br ground state E_{kin}(H) and to the Br^* excited state E_{kin}^*(H) for two laser energies corresponding to wavelengths at 243 nm and at 193 nm. The meaning of the symbols is clear from the text below the equation (2).

D_o (HBr) = 3,745 eV	Br (243 nm): E_{kin} (H) = $\hbar\omega_1 - D_o$ (HBr) = **1,36** eV
E_{int} (Br^*) = 0,475 eV	Br^*(243 nm): E_{kin}^* (H) = $\hbar\omega_1 - D_o$ (HBr) - E_{int} (Br^*)= **0,88** eV
$\hbar\omega_1$ (243,07 nm) = 5,1 eV	Br (193 nm): E_{kin} (H) = $\hbar\omega_2 - D_o$ (HBr) = **2,67** eV
$\hbar\omega_2$ (193,3 nm) = 6,4 eV	Br^* (193 nm): E_{kin}^* (H) = $\hbar\omega_2 - D_o$ (HBr) - E_{int} (Br) = **2,20** eV

The two outer peaks in Fig. 26(a), denoted by Br, get converted in the one higher energy peak in KED (Fig. 26(c)) at theoretical position E_{kin} (H) = 1,36 eV and the two inner peaks corresponding to Br* excited state get transformed into the lower kinetic energy peak in

KED at E_{kin}^* (H) = 0,88 eV. In the case of a 193 nm photodissociation of HBr (Fig. 26(b)), the situation is more complicated. For peaks denoted by black lines holds the same as for Fig. 26(a), but in this KED (Fig. 26(d)) there are two more peaks originating from 193 nm photodissociation of HBr. The theoretical positions of the peak in KED corresponding to the two peaks of Br ground state (blue arrows) should be E_{kin} (H) = 2,67 eV, and for the peak in KED corresponding to Br^* excited state, the calculated position is E_{kin}^* (H) = 2,20 eV.

At a closer look at the spectrum in Fig. 26(c) exhibits a small peak with a somewhat higher kinetic energy than 1,36 eV, at approximately 1,7 eV. It follows from equation (0) that this extra energy has to originate from the excitation energy of the molecule HBr, E_{int} (HBr). And thus these faster H fragments have to originate from an internally excited HBr molecule.

The original explanation of this small peak in the KED spectra shown in Fig. 26(c) was as follows [32]: a hydrogen atom originating from dissociated HBr molecule, collides with another HBr molecule, transferring part of the H-atom kinetic energy into the internal (vibrational) excitation energy of the HBr molecule E_{int} (HBr). Then the excited molecule is dissociated resulting in H-atom with energy higher then 1,36 eV by a vibrational quanta of HBr, $E_{vibr} \approx 0,3$ eV.

However, after recent experiment with acetylene molecules [33], another possible scenario has been proposed. The dissociating HBr molecule is caged by the cluster and then recombines back to the original HBr^* molecule, which is, however, vibrationally excited. Again, if this molecule is dissociated by the next arriving photon, it results in an H atom with energy higher then 1,36 eV by some vibrational quanta. Clusters of acetylene were operating with this mechanism, where the above mentioned excitation of acetylene vibration by collision with escaping dissociated H-atom was not possible. Therefore, an analogical process seems to be more plausible also in the case of HBr clusters.

The shoulders in the peak at 1,2 eV in Fig. 26(b) and at 3,0 eV in Fig. 26(a) should have the same origin. All the mentioned small peaks are shifted from the main peaks denoted by numbered lines by approximately 0,33 eV, which correspond to the vibrational energy of the HBr molecule.

4.3 Mass spectrometry of pyrrole, imidazole and pyrazole clusters

The UV-absorption and photochemistry of pyrrole, imidazole and pyrazole molecules in the gas phase has been studied in great detail previously [34, 35, 36]. In nature, however, the photochemical processes occur in some environment, e.g. in a solvent or in a geometry dictated by a phosphate backbone of a protein molecule. Usually, the biomolecules are also solvated with the water molecules. The solvent can change the photochemistry significantly. Thus, as a further step towards the investigation of biologically relevant processes at the molecular level, the UV-photolysis and ionization of the above molecules were studied in various cluster environments in our laboratory some time ago [37, 38, 39].

In this section the mass spectrometry of various clusters of pyrrole, imidazole and pyrazole molecules will be introduced. Different ionization methods, namely electron and photon ionization described in the section 3.4, were used. The clusters were ionized by electrons with energy of 70 eV and their mass spectra were measured by the quadrupole mass spectrometer. Alternatively, ionization was also achieved by non-resonant multiphoton one-color ionization with 193 nm photons and the time – of – flight mass spectra were recorded. In this case, the time – of – flight spectrometer was used in the high-field mode described in section 3.3. The differences between the methods of cluster ionization, namely non-resonant multiphoton and single photon ionization, and electron impact ionization, are discussed. More importantly, we analyze the differences between the ionization of pyrrole clusters on one side, and imidazole and pyrazole clusters on the other, which point to different stabilization mechanisms in biomolecules bound by different types of hydrogen bonds.

Clusters of various sizes were produced under different expansion conditions, which are specified in the Tab.10. A range of reservoir T_R and nozzle T_N temperatures as well as expansion pressure p_0 were exploited. The coexpansion was done with two different carrier gases He and Ar. The expansions in Ar resulted in larger clusters, while smaller species were generated in He.

The mean neutral cluster sizes in He-expansion for pyrrole [38] and imidazole [39] clusters were determined in the scattering experiment with the He-atom beam. As for our expansion conditions it has been derived for both pyrrole and imidazole, as $\bar{n} \approx 3$. It has been argued that because of the similarity between the mass spectra of these three species, the mean neutral cluster size of pyrazole is also expected to be around $\bar{n} \approx 3$. It is worth noting that, because of the exponential character of the cluster size distribution, the population of trimers is only about 45% of the monomer population, and the monomers dominate in the molecular beam.

Table 10. Selected expansion conditions for producing the clusters: c is concentration of the molecules in the expansion mix with the carrier gas. T_R and T_N are the reservoir and nozzle temperature, respectively. p_0 is expansion pressure and $\bar{n}$ is the mean cluster size for conditions where it was determined.

Carrier gas	Molecule	c [%]	T_R [K]	T_N [K]	p_0 [bar]	$\bar{n}$
He	pyrrole	0,3	281	282	1,5	3
	imidazole	4,1	435	455	2,6	3
	pyrazole	0,3	333	353	2,0	3
Ar	pyrrole	0,2	281	282	3,0	Py_nAr_m $\bar{n} = 4$ $\bar{m} = 8$
	imidazole	0,1	377	393	2,5	
		5,4	435	455	2,0	≥ 6
	pyrazole	0,5	343	363	2,0	

The quadrupole mass spectra of pyrrole, imidazole and pyrazole clusters produced in He expansions are shown in Fig. 28. A common characteristic of both Ar and He coexpansion is that the pyrrole clusters are ionized into molecular Py_k^+ fragments, while the imidazole and pyrazole clusters fragment into protonated Im_kH^+ and Pz_kH^+ ions. The same fragments occur in the TOFMS spectra under multiphoton ionization. The spectra are dominated by these smallest molecular fragments, and peaks decrease exponentially towards larger fragment masses. However, it has to be mentioned that the character of the EI QMS spectra depends on the concentration of the molecules in the expansion mix with the carrier gas. At higher concentrations, the mass peak intensities exhibit a maximum for bigger clusters (it means higher k). Indeed, the TOFMS spectra exhibit a dependence on the expansion conditions and carrier gas too; nevertheless, they always assume an exponentially decaying character and never a maximum at some larger fragment size, which points to much stronger fragmentation of the clusters in the multiphoton ionization process.

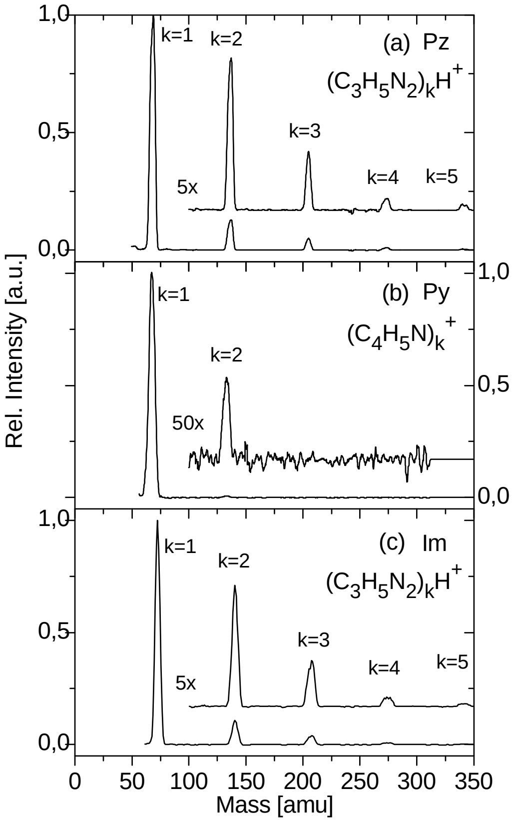

Figure 28. Quadrupole mass spectra of small pyrazole (a), pyrrole (b) and imidazole (c) clusters produced in He- expansion.

The presence of Py_k^+ fragments on one side, and protonated Im_kH^+ and Pz_kH^+ fragments on the other, is in agreement with the hydrogen or proton transfer channel in the photochemistry of imidazole and pyrazole clusters. This observation is also supported by ab-initio calculations and can be understood in terms of the different bonding motifs of these three species pointed out in section 2.3 and shown in Fig. 29. The pyrrole clusters are bound by the weak N-H···π bond, and upon ionization, an ionized core is generated, which is solvated by other pyrrole molecules [38]. Similar behavior can be also found for benzene clusters [40]. However, in the imidazole and pyrazole clusters the relatively strong hydrogen bonds N-H···N is present, which leads to the hydrogen or proton transfer between the cluster constituents upon excitation.

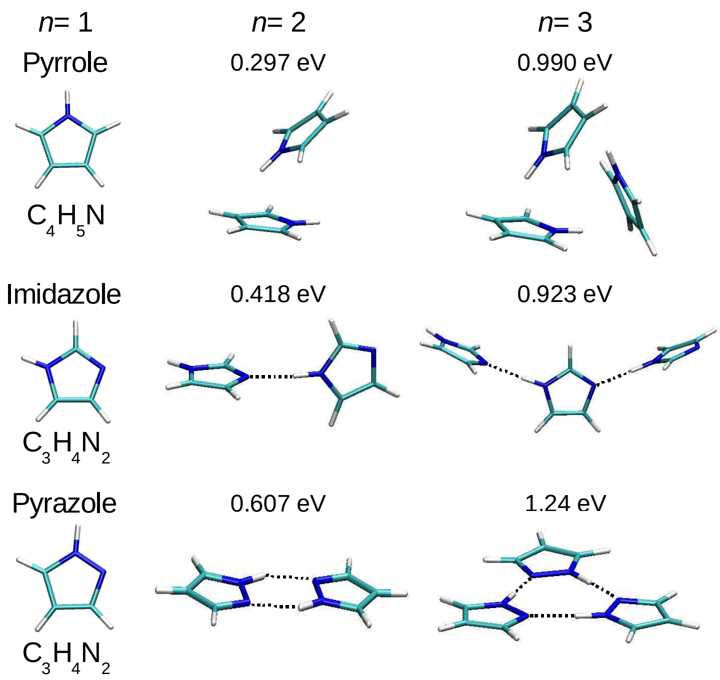

Figure 29. Different hydrogen bonding motifs of pyrrole, imidazole, and pyrazole dimers and trimers are shown. Hydrogen bonds are indicated by dashed lines. The structures and binding energies were calculated at the MP2 level.

Thus, in the hydrogen bonded clusters, the hydrogen or proton transfer process occurs upon multiphoton UV excitation, which leads to energy transfer and dissipation. In this way the protonated species are, indeed, stabilized by the cluster environment. The mass spectra also confirm this conclusion from the photodissociation studies. On the other hand, in the pyrrole clusters, the multiphoton excitation leads to a more intense decay of the cluster and molecule. The H atom bound to the π-electrons of the second unit does not bind to this unit after ionization.

The TOFMS spectra of pyrrole, imidazole and pyrazole clusters were also measured in both He and Ar expansions. The spectra corresponding to the larger clusters generated in the Ar expansions are shown in Fig. 30. The molecular parts of the spectra up to the mass of 75 amu are similar for both He and Ar expansions. However, in the case of He expansion no cluster fragments appeared at higher masses after the photoionization. In these spectra (not shown here) the peak at 69 amu in the imidazole and pyrazole spectra does not correspond to the parent molecule ion, which would be at 68 amu, but rather to the protonated species $\mathrm{Im}_k\mathrm{H}^+$ and $\mathrm{Pz}_k\mathrm{H}^+$ originating as the fragments of the larger clusters. These peaks gain intensity from the larger cluster decomposition that occurs for Ar expansions. The pyrrole clusters, where the hydrogen transfer process cannot occur, fragment completely, generating very few parent Py^+ ions (some Py_2^+ can also be seen upon large magnification), but mainly fragments smaller than the molecule occur.

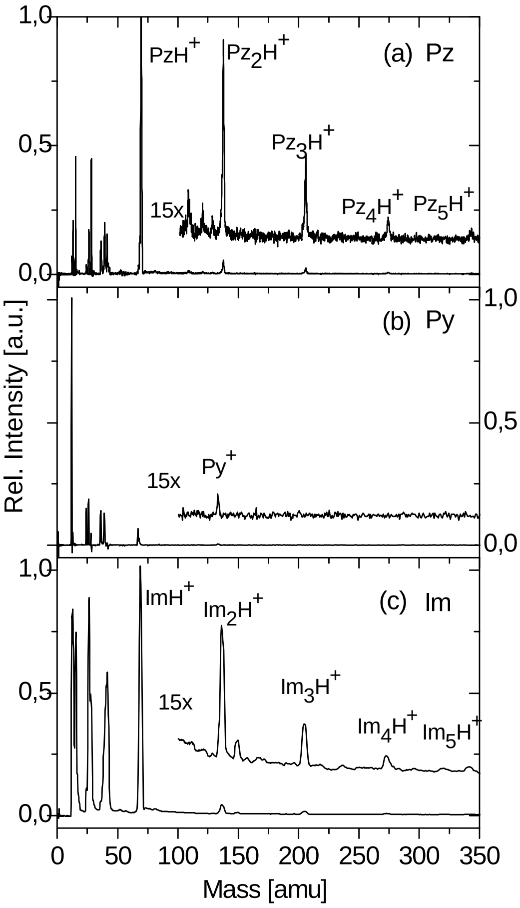

Figure 30. TOF mass spectra of the large pyrazole (a), pyrrole (b), and imidazole (c) clusters produced in Ar- expansion.

Here we focus on the differences between the successive multiphoton ionization with 193 nm photons (6,4 eV) and electron ionization with 70 eV electrons. Fig. 31 shows the TOF mass spectra after multiphoton ionization (black line) and QMS mass spectrum after electron ionization (red stick spectra). Since the resolution of our QMS is poor in this region, this spectrum comes from the NIST database [41]. This mass spectrum is dominated by a parent molecular ion and the group of peaks around 40 amu. On the other hand, the TOF mass spectra exhibit small peak of parent molecular ions in the case of pyrazole and imidazole, and in the case of pyrrole, the peak is even completely missing. The TOF mass spectra are dominated by a C^+ fragment and the group of peaks around 25 amu. Thus, the successive UV multiphoton ionization leads to a significantly higher degree of fragmentation than the electron ionization in all three molecules. The parent molecular ions, which dominate QMS spectra, are not at all present in the TOF spectra, thus the molecule is predominantly fragmented by the successive absorption of two or more photons. There are two main reasons for the higher degree of fragmentation in the non-resonant multiphoton ionization.

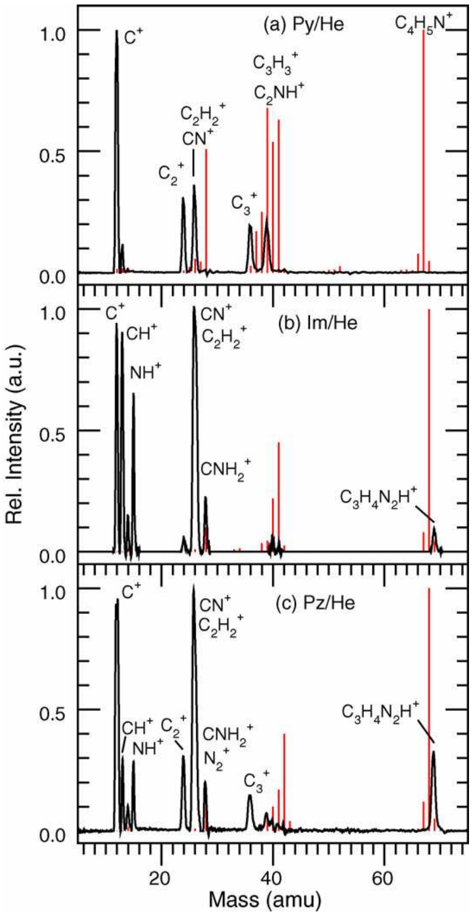

Figure 31. Photoionization TOF mass spectra of small pyrrole, imidazole and pyrazole clusters produced in coexpansion with He carrier gas (black line). The electron ionization QMS spectra of the corresponding molecules are shown for comparison (red stick spectra) [41]. The mass peak assignments in the TOF spectra are based on the photoionization spectra in the literature [42, 43, 44]. The photon flux was $\approx 10^{28}$ cm^{-2} s^{-1}.

Although, the 70 eV energy of the ionizing electrons is much larger than the 193 nm photon energy (6,4 eV per one photon), the energy deposited into the internal excitation of the molecule (cluster) is significantly smaller. From electron energy of 70 eV, remains only around 1 eV for the internal excitation in the molecule, and most of the energy is carried away by the kinetic energy of two escaping electrons [45, 46]. For example, the energy deposited into the internal excitation of the pyrrole cluster ion is around 1-2 eV

[38]. On the other hand, from the 12,8 eV deposited by the two-photon process, all the energy above the ionization potential of the molecule (cluster) can be available as the internal excitation, i.e. 4,6 eV in the case of pyrrole molecule. However, the photoelectron spectrum of pyrrole following one-color multiphoton excitation at 243 nm in Ref. [43] exhibits a maximum at 0 eV and extends to 2 eV. Thus, available energy for the internal excitation of pyrrole in two-photon ionization is from 2,6 to 4,6 eV. To conclude, in the photodissociation process more energy is deposited into the internal excitation of the ion even if photon energy is lower than the energy of electron.

Deposited energy alone cannot explain the differences, however, since the single-photon mass spectra from the literature [42] exhibited less fragmentation even at higher photon energies. Therefore, the second effect playing a role in the fragmentation after photoionization must be the fact that photoionization is also performed by the successively arriving photons. In other words, it is the delay between the subsequently arriving photons which leads to the large fragmentation. During this delay, the species excited with the previous photon can undergo some fragmentation, and the subsequent photon ionizes and/or further fragments the excited species.

To investigate the effect of the delay between the successively absorbed photons, the dependence on the photon flux, in the case of pyrazole, was measured and is shown in Fig. 32. Plotted there are ratios of various mass peaks to the protonated monomer PzH^+ for pyrazole as a function of the photon flux. At small photon fluxes the PzH^+ (originating from the clusters) is the major peak in the spectrum. The peaks at mass 12 amu (C^+) and 26 amu (CN^+ and $C_2H_2^+$) dominate the spectrum in Fig. 31(c). These peaks quickly rise with the photon flux. The ratio of the other peaks at 24amu (C_2^+/PzH^+) and 36 amu (C_3^+/PzH^+) also increase, but the increase is slower. The ratio of the fragments at 15 amu (NH^+/PzH^+) and 28 amu (CNH_2^+ and/or N_2/PzH^+) increases only very little with the photon flux. Some qualitative conclusions can be drawn from these dependencies.

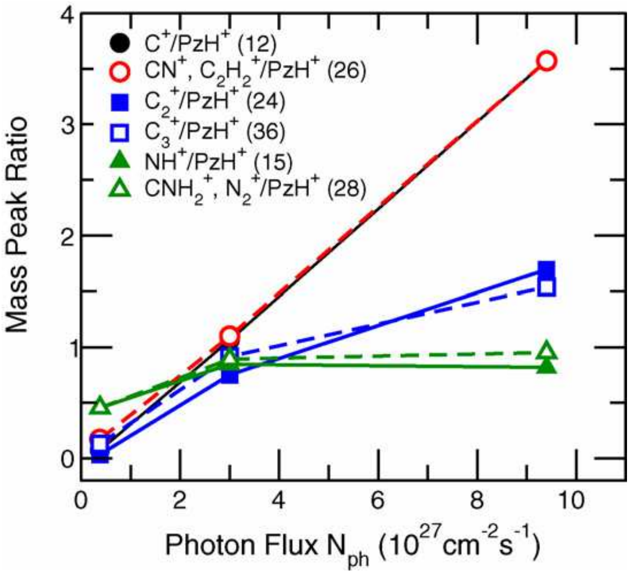

Figure 32. Intensity ratios between various indicated mass peaks and the PzH^+ peak in the TOFMS of pyrazole clusters as a function of the laser photon flux. Note that the black circles corresponding to the C^+/PzH^+ ratio are blanked out by the open red circles.

The C^+ ion is a product of the fragmentation caused by a large number of photons. More complex CN^+ and/or $C_2H_2^+$ fragments result from the same fragmentation. The creation of the C_2^+ and C_3^+ ions require somewhat less photons. Finally, the NH^+ and CNH_2^+ ions are a product of the fragmentation caused by the smallest number of photons, and their dependences on the photon flux is roughly the same as for PzH^+ ions. Thus, their generation requires about the same number of photons.

These results have already been published in the International Journal of Mass Spectrometry [1]. This publication can be also found in the appendix A.

5. Photodissociation

5.1 Photodissociation of HI on water clusters

Complexes of HBr and HCl molecules and water have attracted considerable attention because of two reasons. First, great efforts have been devoted to the explanation of the microscopic picture of acidic dissociation. Moreover, acid solvation on ice nanoparticles or liquid aerosols has been studied because of the great importance it has in atmospheric chemistry as remarked in section 2.2.

Photodissociation experiments with water clusters doped with HBr and HCl were performed in our laboratory some time ago [2, 3, 12]. These recent experiments have shown that the HX molecule (X = Br, Cl) undergoes acidic dissociation on a water cluster in the ground state, forming a zwitterionic system $H_3O^+(H_2O)_{n-1}X^-$. This system is excited by an ultraviolet laser pulse at 193 nm and an excited state is produced, which then relaxes to a neutral biradical $H_3O(H_2O)_{n-1}X$ state. There is still enough energy in the system to cause the hydronium molecule to decay into an H radical and water molecule, leaving an H-atom to be detected. Both experimental and theoretical evidence have been obtained for the proposed scenario in the previous studies of HBr and HCl molecules on ice nanoparticles.

An apparent extension of the previous studies is the investigation of photodissociation of large water clusters doped with HI molecules, introduced in this section. For comparison, the photodissociation of argon clusters $(Ar)_n$ ($\bar{n}$ =39) doped with HI molecules will also be discussed. Since HI is a stronger acid than the previously studied molecules, it is more prone to the acidic dissociation. Theoretical calculations suggest that HI undergoes acidic dissociation into zwitterionic structure in clusters with less H_2O molecules than HCl and HBr. Thus, if the evidence is found for H_3O radical generation in the $HI(H_2O)_n$ particles, it can provide further confirmation for the mechanism of its generation proceeding through the acidic dissociation in the ground state. Further, the HI, because of its acidic properties, may be expected to exhibit a lower lying CTTS state than the other hydrogen halides. Thus this state might be excited and the H_3O generated at even longer wavelengths in our experiment than 193 nm, for which it was observed with HBr and HCl molecules.

The experimental conditions are listed in the Tab. 12. Note, that photodissociaton of $HI(H_2O)_n$ and $HI(D_2O)_n$, as well as other measurements of $HI(H_2O)_n$ and $DI(H_2O)_n$, was performed at the same conditions. It enables us to compare these spectra. The reservoir temperature T_R is not listed for argon clusters, because a cluster source without a reservoir was used.

Table 12. The experimental conditions. The first column corresponds to measurement of both $HI(H_2O)_n$ and $HI(D_2O)_n$, and the TOF spectra are depicted in Fig. 33(a). There are the conditions for the measurements of $HI(H_2O)_n$ and $DI(H_2O)_n$ in the second column and spectra corresponding to this measurement are depicted in Fig. 33(b). Finally, the spectra corresponding to the conditions of $HI(Ar)_n$ photodissociation in the last column are shown in Fig. 35(b).

	$HI(H_2O)_n$	$HI(D_2O)_n$	$HI(H_2O)_n$	$DI(H_2O)_n$	$HI(Ar)_n$
Nozzle diameter d [μm]	75		75		50
Opening angle β [°]	30		30		30
Nozzle temperature T_N [K]	438		438		245
Reservoir temperature T_R [K]	427		428		-
Expansion pressure p_0 [bar]	4,5		4,5		2,3
Pick-up pressure p_0(HI) [mbar]	0,1		0,1		0,055
Laser intensity – 243nm [J/pulse]	2,8		1,2		2.7
Laser intensity – 193nm [J/pulse]	64		82		-
U_a/U_b [V]	50/ 41,40		50/ 41,34		50/ 41,40
MCP voltage [kV]	-1,65		-1,7		-1,60
WMTOF extraction field E_s [V.cm^{-1}]	7,8		7,9		7,8
Mean cluster size $\overline{n}$	434		454		29

Originally this experiment was designed to prove whether the hydrogen halide molecule was acidically dissociated or remained covalently bound on the water clusters. The essential idea was as follows: If the HX molecule was covalently bound, it could be photodissociated by an appropriate wavelength of the laser pulse and an H-fragment signal originating directly from the HX molecule would be expected. On the other hand, no H-fragment signal would be expected if this molecule was acidically dissociated on X^- and H_3O^+. In other words, the presence of detected H-fragment signal should prove that the

HX molecule is covalently bound on the cluster $(H_2O)_n$. However, it has already been shown in the previous investigations of HBr and HCl that the situation is more complicated, and a very careful and complete experiment proved just the opposite of the original expectation; the H-fragment signal observed experimentally was evidence that the HX was acidically dissociated on the water cluster.

Fig. 33(a) shows the TOF spectrum of H-fragments from the system $HI(H_2O)_n$. The clusters were produced by the pick-up process of HI molecules on the $(H_2O)_n$ clusters. The experimental conditions are further detailed in Tab. 12. It can be clearly seen from Fig. 33(a) that H-fragment signal was detected after photodissociation of the system $HI(H_2O)_n$. The photodissociation was performed with a 243 nm (Fig. 35(a)), as well as a 193 nm (Fig. 33(a)), laser pulse. The H-fragment signal originating from pure $(H_2O)_n$ clusters of the same size is about an order of magnitude lower than the signal detected when the HI molecules were embedded in clusters. The signal from the pure water clusters is subtracted as a background from the spectra depicted in Fig. 33. It suggests that the detected H-fragment signal originates from the HI molecule. To further verify this hypothesis and confirm that the H-fragment signal does not originate from H_2O, a photodissociation experiment of the HI molecule on the clusters of heavy water $(D_2O)_n$ was performed. The measured spectrum is shown in the same figure as those for the system $HI(H_2O)_n$ for comparison. It ought to be mentioned that deuterium was not detected. Since deuterium is twice as heavy as hydrogen, the peak in the time-of-flight spectrum would appear at the flight time of 5,65 μs, while the flight time for hydrogen is 4 μs (with the present extraction voltages). Also the wavelength 243,07 nm is not proper for REMPI of the deuterium, since it is outside the 0,04 nm bandwidth of our laser. Therefore, the photodissociation experiment of $HI(D_2O)_n$ still suggests that the H-fragment signal originates from the HI molecule, however, it is not clear why the measured H-signal should be smaller than from the $HI(H_2O)_n$ system under otherwise the same conditions.

Nevertheless, the photodissociation experiment with DI on water clusters $(H_2O)_n$ points to a different source of the H-fragment signal. In this system, no signal besides the weak one originating from the H_2O was expected. However, it appeared that the signal originating from $DI(H_2O)_n$ was even higher than the signal from $HI(D_2O)_n$.

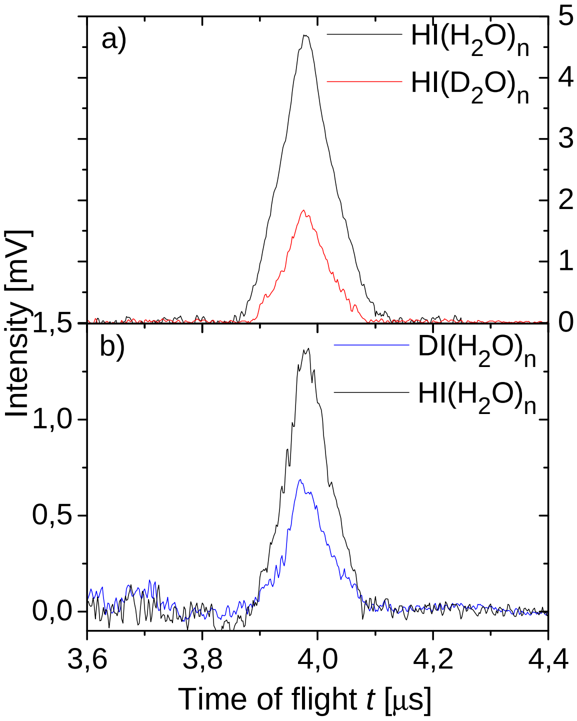

Figure 33. TOF distributions of H-atom fragments from $HI(H_2O)_n$ and $HI(D_2O)_n$ (a), and $HI(H_2O)_n$ and $DI(H_2O)_n$ (b) at the photodissociation wavelength 193 nm.

To summarize, the H-fragment signal was detected in the photodissociation of all three species, e.g. $HI(H_2O)_n$, $DI(H_2O)_n$ and $HI(D_2O)_n$. This fact proves that the H-fragment signal can originate directly neither from the HI molecule, nor from H_2O. These results can be understood by proposing that the H-fragment signal originates from the hydronium molecule H_3O. In other words, from H_3O, DH_2O, and D_2HO in the case of experiment with $HI(H_2O)_n$, $DI(H_2O)_n$, and $HI(D_2O)_n$, respectively. A strong piece of experimental evidence for this conclusion, found in the previous experiments with HBr, was the H-signal ratio from $HBr(H_2O)_n$, $DBr(H_2O)_n$ and $HBr(D_2O)_n$, which was almost exactly 3:2:1, i.e. corresponding to the ratio of H atoms in the corresponding H_3O, DH_2O, and D_2HO species (and similar was also true for HCl system) [2, 3]. In the present case, the ratio of the H-fragment signal intensities of $HI(H_2O)_n$ and $HI(D_2O)_n$ is 3:1,2 at 193 nm (Fig. 33(a)) and 3:0,8 at 243 nm (Fig. 35(a)). This ratio is again close (within experimental error) to the 3:1 ratio of H atoms in the hydronium molecules H_3O and D_2HO. Similarly, the intensity ratio for $HI(H_2O)_n$ and $DI(H_2O)_n$ (Fig. 33(b)) at the laser wavelength 193 nm is about 3:1,5. Since the ratio of H atoms in the hydronium molecules H_3O and DH_2O is 3:2, it can be seen that an agreement between these two ratios is not perfect, yet it falls within the experimental errors that the previous conclusions made for the other two hydrogen halide systems. [2, 3]. In support of these results, it can be concluded that our overall intensity ratio of $HI(H_2O)_n$, $DI(H_2O)_n$, and $HI(D_2O)_n$, about 3:1,5:1,2, corresponds within experimental error to the 3:2:1 ratio of H atoms in the hydronium molecules H_3O, DH_2O, and D_2HO.

The proposed mechanism of H_3O formation is schematically depicted in Fig. 34. The formation of the hydronium molecule H_3O was proposed in similar systems by Domcke and Sobolewski in several theoretical calculations [47, 48, 49, 50, 51]. In the first step, the HI molecule undergoes the acidic dissociation in the ground state on a water cluster, forming a zwitterionic structure with I^- and H_3O^+. The resulting system of $H_3O^+ I^- (H_2O)_{n-1}$ is excited by the ultraviolet laser pulse and an excited state $S_1^{'}$ is produced, which is of the charge-transfer-to-solvent (CTTS) character. The system then relaxes into a biradical minimum $S_k^{''}$ with an H_3O neutral molecule. There is still enough energy in the systemto allow the hydronium molecule to decay into an H radical and water. The resulting H atom is ionized by the REMPI process at 243,07 nm, and detected by the TOF spectrometer.

It has to be mentioned that there was a suggested second possible mechanism [2], which starts with exciting an intact HI molecule into the dissociative state. The high energy H atom penetrates into the water cluster, loses some kinetic energy and is slowed down by collisions, and recombines with a water molecule forming the hydronium molecule. However, if this was the case, at least some of the fast hydrogen atom would be detected from the direct photodissociation of the HI molecule. Since no such fast H atoms are detected, it seems that the mechanism discussed above is preferable. As already outlined in the introduction of this section, the HI molecule being a stronger acid, is expected to dissociate even more easily than HBr and HCl, and thus the previously proposed mechanism seems plausible here.

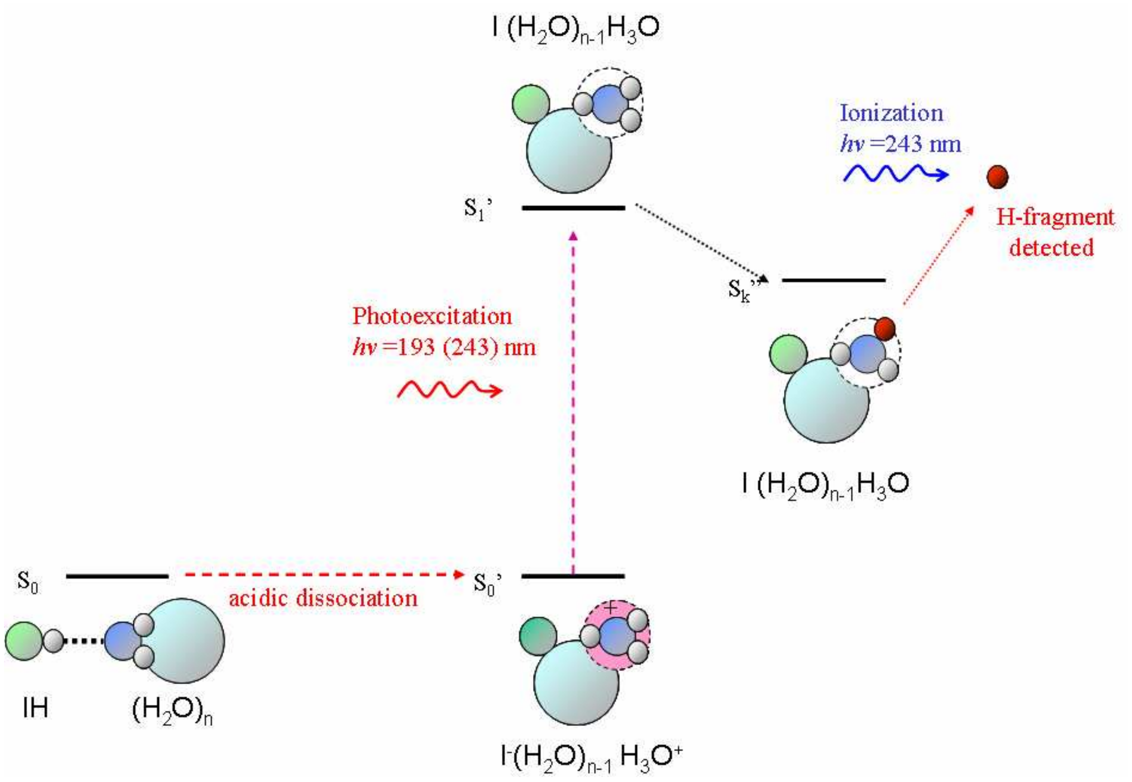

Figure 34. The outline of the mechanism for photolysis of water clusters $(H_2O)_n$ doped with HI.

The zwitterionic structure H_3O^+ I^- $(H_2O)_{n-1}$can be either of a contact ion type or the ions can be separated by water molecules in cluster. The latter possibility would lead to proton hopping and to a fast isotopic dilution in experiment with D_2O. From the intensity ratio it follows that isotopic dilution does not occur, therefore the formation of the contact ion pair is more probable.

It has to be mentioned, that there were no H-fragments detected in the one-color photodissociation experiment at 243 nm with water clusters doped with HCl and HBr molecules [2, 3]. It is in coincidence with the theoretical calculations [48] of the excited state $S_1^{'}$ energy for the molecule HCl on water clusters starting around 6 eV. Since this energy is higher than energy of the laser pulse at 243 nm (5,1 eV), no signal can be observed at this wavelength in the photodissocition experiment with HCl on water clusters. On the other hand, as can be seen from Fig. 35(a), there was an H-fragment signal detected in the case of the HI molecule at this wavelength. It can be understood through the fact that the excited CTTS state $S_1^{'}$ lies lower in energy for the HI molecule than for HBr and HCl molecules, and mainly below a 5,1 eV energy of the laser pulse. Preliminary theoretical calculations suggest that the excited state $S_1^{'}$ lies below 5,1 eV [52].

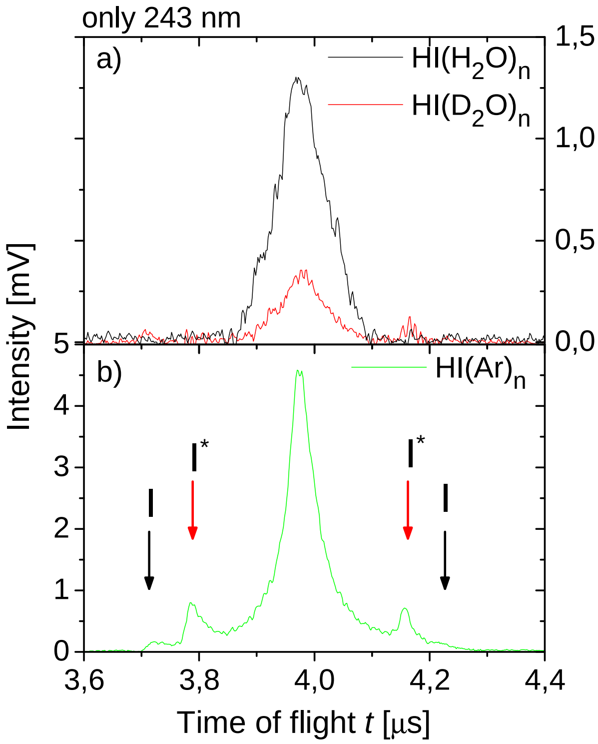

Figure 35. TOF distributions of H-atom fragments from $HI(H_2O)_n$ and $HI(D_2O)_n$ (a), and $HI(Ar)_n$ (b) at the photodissociation wavelength 243 nm. The (black) red arrows denote the peaks corresponding to the direct cage exit H-fragments leading to the I (I^*) molecule.

In addition, to support our hypothesis about the formation of the hydronium molecule H_3O, the photodissociation experiment of water clusters doped with the HI molecule can be compared with the photodissociation of HI on argon clusters $(Ar)_n$, where no acidic dissociation can happen. The H-fragments TOF spectra after photodissociation of $HI(H_2O)_n$ and $HI(Ar)_n$ at 243 nm are shown in Fig. 35(a) and (b), respectively. Note that these two spectra exhibit different shapes, and there are peaks corresponding to the direct cage exit in the spectrum of $HI(Ar)_n$. Such fragments are completely missing in the TOF spectra after photodissociation of water clusters doped with HI molecules (Fig. 35(a)). The positions of fragments from the direct photolysis of HI correspond to the formation of the iodine ground state I, and the excited state I^* are indicated by arrows. Thus the intensity at these positions clearly corresponds to the H-fragments from the direct photodissociation of an HI molecule on an Ar cluster. No such maxima are present in the spectra from the water system. Besides a zero kinetic energy peak in the TOF spectrum, the peak from Ar clusters is significantly sharper than the peak from the water system. This is again an indication that, in the case of $(Ar)_n$, clusters this peak corresponds to the H-fragments from HI molecule dissociation slowed down to near zero velocities by collisions with Ar atoms. In the case of water, this broader peak is of a different origin. These differences between both spectra can be understood by noting that the H-fragment signal originates from the hydronium molecule H_3O in the photodissocition of $HI(H_2O)_n$, while in the case of photodissociation of $HI(Ar)_n$, the H-fragment signal has to originate directly from the HI molecule.

These differences are further illustrated when the TOF spectra are converted to kinetic energy distributions (KEDs) in Fig. 36 and 37. Note that H-atom KEDs of $HI(H_2O)_n$ at the laser wavelength 193 nm (Fig. 36(a)) and 243 nm (Fig. 36(b)) exhibit similar characteristics. There are the low energy maxima close to zero, around 0,1 eV, and the spectrum extends to about 0,5 eV. The small peaks above 0,5 eV are due to poor background subtraction and data processing. Note also that there are larger error bars at higher energies. Thus, there are no fast H-fragments in the photodissociation of water clusters doped with the HI molecule.

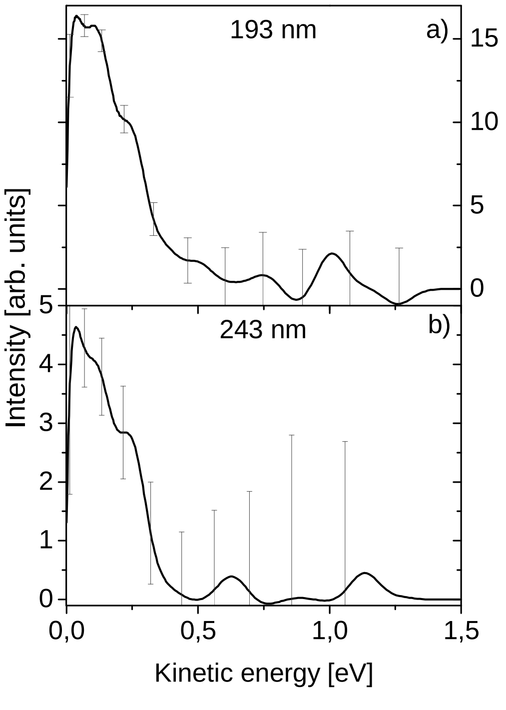

Figure 36. H-fragment kinetic energy distribution after photodissociation of $HI(H_2O)_n$ at 193 nm (a) and 243 nm (b).

On the other hand, there can be clearly distinguishable peaks corresponding to the direct cage exit in Fig. 37. The theoretical positions, calculated in Tab. 13, of these peaks are denoted by arrows. The total lack of these fast H-fragments in the KEDs from water clusters (Fig. 36) suggests that there was no direct photodissociation of HI on water clusters. Besides, it is worth noting, that these spectra fall within the experimental errors of the KEDs from HBr and HCl on water clusters measured previously. This is yet another piece of evidence that the H-fragments originate from the same species –i.e. H_3O- in the case of all three systems $HX(H_2O)_n$.

Note that the middle zero kinetic energy peak in the spectrum of $HI(Ar)_n$ (Fig. 35(b)) is narrower than those corresponding to H-fragments from $HI(H_2O)_n$. These peaks are transformed into the shoulder near the zero kinetic energy in KEDs. In the system $HI(Ar)_n$, the released H atom with some kinetic energy is generated by direct HI photodissociation. This fragment penetrates into the cluster and is slowed down by collisions to zero kinetic energy (cage effect) [53, 54]. Therefore most H atoms with zero kinetic energy are detected. However, the caging is not perfect, therefore there is a decreasing number of fragments with some higher kinetic energy up to the peak of the direct cage exit. On the other hand, H atoms originate from the hydronium molecule H_3O in the system $HI(H_2O)_n$. This hydronium molecule has excess energy from the laser pulse, which exceeds its dissociation limit. Consequently, the H_3O statistically decays over a small barrier, and it results in a statistical distribution of the fragment kinetic energies. This distribution will always be 0 at zero kinetic energy.

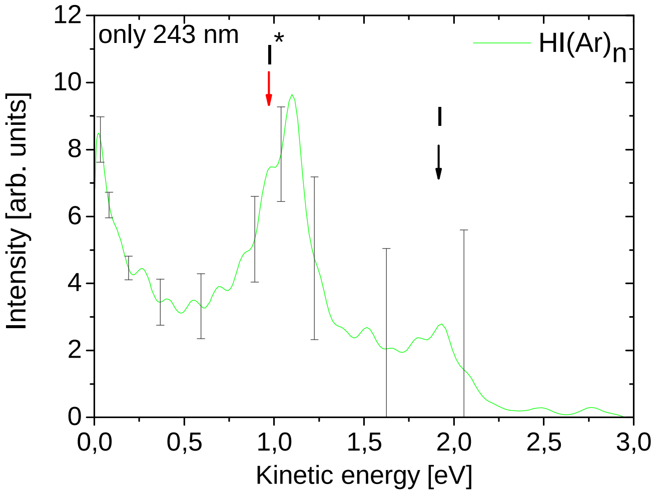

Figure 37. H-fragment kinetic energy distribution after photodissociation of $HI(Ar)_n$ at 243 nm. The (black) red arrows denote the theoretical positions of the peaks corresponding to the direct cage exit H-fragments leading to the I (I^*) molecule.

The hydronium molecule is a metastable radical molecule, whose dissociation energy into H_2O + H is about 0,2 – 0,3 eV. This dissociation process is exothermic with released energy of about 0,4 – 0,8 eV, depending on the environment. This is consistent with the H atom kinetic energy limiting value of ~0,5 eV (Fig.36).

Table 13. Calculated kinetic energy of H-fragments corresponding to the dissociation of HI to the iodine ground state E_{kin}(H) and to the iodine excited state E_{kin}^{*}(H) for the laser energy corresponding to a wavelength at 243 nm. The meaning of the symbols is clear from the text below the equation (2).

D_o (HI) = 3,194 eV	I (243 nm): E_{kin} (H) $= \hbar\omega_1 - D_o$ (HI) = **1,906** eV
E_{int} (I^*) = 0,943 eV	I^*(243 nm): E_{kin}^{*} (H) $= \hbar\omega_1 - D_o$ (HI) $- E_{int}$ (I^*) = **0,963** eV
$\hbar\omega_1$ (243,07 nm) = 5,100 eV	

It ought to be mentioned that there is also other proofs for the suggested mechanism of the hydronium molecule formation. They are based on the comparison of the KEDs of HBr and HCl on water and argon clusters [2, 3]. The KEDs reflect the energetics of the HBr and HCl molecules (and also HI) in the photodissociation experiment with argon clusters. In other words, the spectra exhibit different characteristics since they come from different molecules. On the other hand, the spectra corresponding to the photodissociation of the HBr and HCl molecules on water clusters exhibit very similar characteristics (also similar to our KED spectra of HI on water clusters- Fig. 36). It suggests that these spectra should originate from the common molecule – the hydronium molecule.

5.2 Photodissociation of HNO_3 on $(H_2O)_n$ clusters

As has been shown in the previous section 5.1 and also in Ref. [2, 3, 12], the HX (X = Cl, Br, I) molecule undergoes acidic dissociation on a water cluster in the ground state, forming a zwitterionic structure $H_3O^+(H_2O)_{n-1}X^-$. This system is excited by an ultraviolet laser pulse at 193 nm and an excited state is produced, which then relaxes to a neutral biradical $H_3O(H_2O)_{n-1}X$ state.

The question is if a similar process occurs with other acids present in the polar stratospheric clouds. Therefore, we measured the photodissociation of nitric acid on water clustrs. It is known that the photodissociation of hydrogen atom from HNO_3 without water clusters is very ineffective at 193 nm [55, 56, 57]. Hence, we had expected that if an H fragment signal was detected, it could originate from the generation of the hydronium molecule after the acidic dissociation in an analogy to the experiments discussed above.

First, fuming nitric acid with a purity ≥ 99% was used. It was degassed to remove air and traces of NO_2. It has to be noted that the colorless and thus pure nitric acid has never been achieved in our system, even after a very long degassing. The yellowish color indicated the presence of NO_2 and its dimer N_2O_4. However, the photodissociation experiment was performed but the H-fragment signal was never detected.

In addition, we tried other methods of preparing pure HNO_3. Nitric acid with a purity 65% was mixed with sulfuric acid in a ratio of 2:1 and kept at -15°C, in which the sulfuric acid acted as water trapping agent. This mixture was frozen at the temperature of liquid nitrogen and evacuated. Afterwards, it was slowly brought to room temperature, allowing the NO_2 to bubble out. This cycle was repeated five times. A colorless liquid was achieved, but the signal was never found.

However, the mass spectra of the water clusters with the background subtracted showed some indication of HNO_3 related peaks (i.e. 81 amu $HNO_3.H_2O^+$ in Fig. 38). From that it could be concluded that some nitric acid molecules landed on our $(H_2O)_n$ clusters.

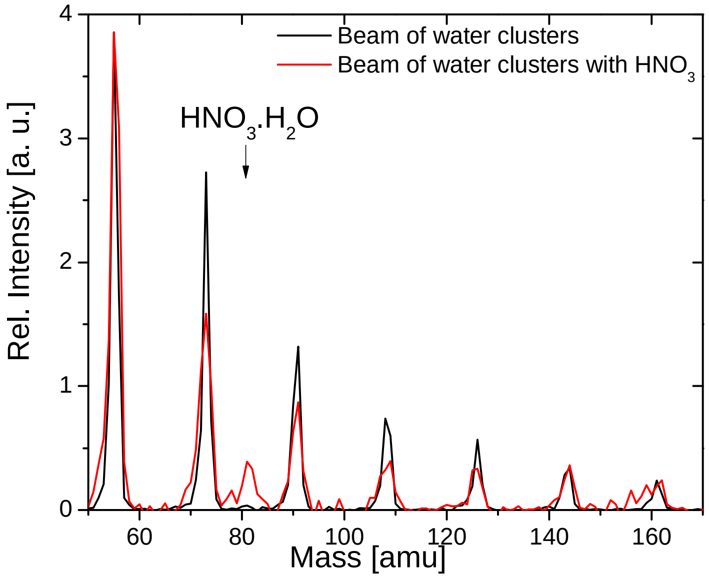

Figure 38. The quadrupole mass spectrum of nitric acid on the water clusters

It has to be noted that the experiment was performed many times, under various experimental conditions, using different techniques of nitric acid purifying and even with two different samples of nitric acid, but a signal was never detected. However, it is very difficult to prove that the total lack of the signal means that the process similar to HX (X= Br, Cl, I) on water clusters described above does not occur with HNO3.

6. Conclusion

Several experiments with various clusters were performed on the molecular beam apparatus described in this Thesis.

(1) The beam velocities for rare gases and water clusters, under various expansion conditions, were measured and compared with the theoretical values, which were calculated from the equation (30). This equation was, in fact, derived for an ideal gas, since the assumption of a temperature independent heat capacity c_p was used. Moreover, it was provided that the initial stagnation enthalpy H_0 of the expanding gas is completely converted into the directed translational motion. It follows that the theoretical velocities should form an upper limit for the experimental velocities if the condensation energy would be negligible. On the other hand, the energy balance (24) does not take into account the condensation energy which is released during cluster condensation. This condensation energy could raise the experimental velocities above the theoretical values. In spite of these facts, or due to their mutual cancellation, the equation (30) gives the velocities of rare gases correctly within 0,7 – 7 % of the experimental values. Moreover, it even describes the velocity of water clusters within 1- 4 % despite of the fact that water can be hardly considered as an ideal gas.

The experimental velocities of neon, argon and krypton produced from a rare gas cluster source lie below the theoretical velocities within the entire temperature range. It is in agreement with the assumption that the initial stagnation enthalpy H_0 of the gas is completely converted into directed translational motion, which was used for deriving the equation (30). This assumption is not satisfied, since there always remains some residual temperature T.

The experimental velocities of the water clusters are higher than the theoretical ones predominantly because the condensation energy is deposited into the forward velocity of the clusters. This condensation energy is not taken into account in the derivation of equation (30). The velocity of the water clusters also depends on the temperature of reservoir T_R because of the pressure p_0 dependence on this temperature, and if larger clusters are produced consequently more condensation energy is released leading to a faster beam.

It was shown that the measured maximum value of the velocity distribution for supersonic expansion $u_{\max}$ is shifted to twice as high a velocity as the theoretical maximum of the Maxwell – Boltzmann distribution v_{MB} for water vapor expansion. The full width at half maximum (FWHM) for the supersonic expansion at the given conditions was $\Delta v =$ 180 m.s^{-1}, much narrower than the FWHM for Maxwell – Boltzmann distribution, which was around 700 m.s^{-1}.

(2) The photodissociation of $(HBr)_n$ clusters was previously studied on our apparatus in a great detail [12, 13, 31]. However, it was measured within this Thesis for calibration purposes, which mainly consists of laser alignment to intersect the molecular beam in the right position with the two laser beams and for overall verification of the correct function of the apparatus. Besides, the principle of the photodissociation experiment can be well understood and nicely explained with the example of $(HBr)_n$ cluster photodissociation. The typical spectra are shown and explained here.

(3) Clusters of imidazole, pyrazole and pyrrole were produced and ionized by electron ionization and non-resonant subsequent multiphoton processes with a 193 nm laser pulse. In the former ionization method, fragments were detected by the quadrupole mass spectrometer, while in the latter, by the WMTOF spectrometer. Two major issues are investigated: (I) the differences between subsequent multiphoton, single photon and electron ionization. (II) The differences between the ionization of imidazole and pyrazole clusters on one hand, and pyrrole clusters on the other. It has been shown that subsequent multiphoton ionization leads to a significantly higher degree of fragmentation than the electron or single photon ionization. There are two main reasons for the higher degree of fragmentation in the non-resonant multiphoton ionization. (A) More energy is deposited into the internal excitation of the ion in the photoionization process even if the photon energy (6,4 eV) is lower than the electron energy (70 eV). However, the deposited energy cannot explain the differences alone, since the single-photon mass spectra from the literature [42] exhibited less fragmentation even at higher photon energies. (B) The second effect playing a role in the fragmentation after photoionization is the delay between the subsequently arriving photons, which leads to the large fragmentation. During this delay the species excited by a photon can undergo some fragmentation, and the subsequent photon ionizes and/or fragments the excited species further.

In addition, pyrrole clusters are ionized into molecular Py_k^+ fragments, while imidazole and pyrazole clusters fragment into protonated Im_kH^+ and Pz_kH^+ ions. It can be understood in the view of the different hydrogen bonding motifs of these three molecules in clusters. The pyrrole clusters are bound by the weak N-H···π bond, and upon ionization the ionized core is generated, which is solvated by other pyrrole molecules [38]. On the other hand, in the imidazole and pyrazole clusters the relatively strong hydrogen bond N-H···N is present, which leads to the hydrogen or proton transfer between the cluster constituents upon excitation. It points to the interesting issue of photostability of the hydrogen bonding imidazole and pyrazole clusters, where the hydrogen or proton transfer process occur upon multiphoton UV excitation, which leads to the energy transfer and dissipation. In this way, the protonated species are stabilized by the cluster environment. On the other hand, in the pyrrole clusters the multiphoton excitation leads to an almost complete decay of the cluster and also of the molecule.

(4) Photodissociation of an HI molecule on water clusters $(H_2O)_n$ was studied and compared to the photodissociation on $(Ar)_n$ clusters ($\bar{n}=39$). It was shown that HI molecules acidically dissociate on $(H_2O)_n$ and zwitterionic species $H_3O^+ I^- (H_2O)_{n-1}$ are generated, which are then excited into biradical states with the neutral hydronium molecule H_3O. There is still enough energy in the system to allow the hydronium molecule to decay into H radical and water. The resulting H atom is ionized by the REMPI process at 243,07 nm, and detected by the TOF spectrometer. To verify this mechanism, photodissociation of the HI molecules on heavy water clusters $(D_2O)_n$, and also photodissociation of the DI on the water clusters was performed. The H-fragment signal was detected in the photodissociation of all three species, e.g. $HI(H_2O)_n$, $DI(H_2O)_n$ and $HI(D_2O)_n$. This fact proves that an H-fragment signal cannot originate directly from the HI molecule or from H_2O. It rather suggests that our hypothesis about the formation of H_3O is correct. Moreover, our overall intensity ratio of $HI(H_2O)_n$, $DI(H_2O)_n$, and $HI(D_2O)_n$, about 3:1,5:1,2, corresponds (within experimental error) to the 3:2:1 ratio of H atoms in the hydronium molecules H_3O, DH_2O, and D_2HO.

It ought to be mentioned that there were no H-fragment detected in the one-color photodissociation experiment at 243 nm with water clusters doped with HCl and HBr molecules [2, 3]. However, the opposite holds true in the case of the HI molecule at this wavelength. It can be understood through the fact, that the excited CTTS state $S_1^{'}$ lies lower in energy for the HI molecule than for HBr and HCl molecules, below the energy of the laser pulse 5,1 eV.

(5) Finally, the photodissociation of HNO_3 on the water clusters was exploited. We wanted to find out if a similar process occurs with other acids present in the polar stratospheric clouds, such as HX (X = Cl, Br, I) discussed in the paragraph (4) and Sec. 5.1. However,

the H-fragment signal was never found. Since it is hard to claim that the lack of the signal proves, that no formation of hydronium molecules occurs in the photodissociation process with the system $HNO_3(H_2O)_n$, this topic remains open for future studies.

References

[1] Poterya, V.; Tkáč, O.; Fedor, J.; Fárník, M.; Slavíček, P.; Buck, U. *International Journal of Mass Spectrometry* **290** (2010), 85.

[2] Poterya, V.; Fárník, M.; Slavíček, P.; Buck, U.; and Kresin, V. *J. Chem. Phys.* **126** (2007), 071101.

[3] Ončák, M, Slavíček, P. Poterya, V.; Fárník, M.; Buck, U. *J. Phys. Chem.* **112** (2008), 5344.

[4] Dunoyer, L.: *Le Radium* **8** (1911), 142.

[5] Stern, O.: *Z. Phys.* **2** (1920), 417.

[6] Gerlach, W.; Stern, O.: *Z. Phys.* **9** (1922), 349.

[7] Stern, O.: *Z. Phys.* **39** (1926), 751.

[8] Becker, E.W.: *Z. Phys.* D **3** (1986), 1.

[9] Hartmann, M.; Miller, R.E.; Toennies, P.J.; Vilesov A.F.: *Science* **272** (1996), 1631.

[10] Finlayson-Pitts, B. J. and J. N. Pitts, J., *Chemistry of the Upper and Lower Atmosphere, Academic Press*, San Diego, 2000.

[11] Peter, T.: *Annu. Rev. Phys. Chem.* **48** (1997), 785.

[12] Fárník, M.; Buck, U.: *Physica Scripta* **76** (2007), C73.

[13] Baumfalk, R.; Buck, U.; Frischkorn, C.; Gandhi, S.R.; Lauenstein, C.: *Ber. Bunsenges. Phys. Chem.* **101** (1997), 606.

[14] Buck, U.; Meyer, H. *Phys. Rev. Lett.* **52** (1984), 109.

[15] Gough, T.E.; Mengel, M.; Rowntree, P. A.; Scoles, G.: *J. Chem. Phys.* **83** (1985), 4958.

[16] Auerbach, D.J.: *Atomic and Molecular Beam Methods*, Oxford University Press, New York, 1988.

[17] Wiley, W.C.; McLaren, I.H.: *Rev. Sci. Instrum.* **26** (1955), 1150.

[18] Pauly, H.; *Atom, Molecule and Cluster Beams I, Springer, New York, 2000.*

[19] Yamada, H.; Taniguchi, N.; Kawasaki, M.; Matsumi, Y.; Gordon, R. J. *J. Chem. Phys.* **117** (2002), 1130.

[20] http://ael.gsfc.nasa.gov/saturnGCMSMass.shtml (July 2009)

[21] Pedder, R.E.: Extrel Application Note RA 2010A (2001).

[22] McCarty, R. D.; Arp, V. D.: *Advances in Cryogenic Engineering* **35** (1990), 1465.

[23] Christen, W.; Rademann, K. *Phys. Rew. A* **77** (2008), 012702.

[24] Christen, W.; Rademann, K.; Even, U. *J. Chem. Phys* **125** (2006), 174307.

[25] Hillenkamp, M.; Keinan, S.; Even, U. *J. Chem. Phys* **118** (2002), 8699.

[26] Bruch, L.W.; Schollkopf, W.; Toennies, J.P. *J. Chem. Phys*, **117** (2002), 1544.

[27] Lubman, D. M.; Rettner, C. T.; Zare, R. N. *J. Phys. Chem.* **86** (1982), 1129.

[28] Hagena, O. F. *Surf. Sci* **106** (1981), 101.

[29] Bobbert, C.; Schutte, S.; Steinbach C.; Buck, U. *Eur. Phys. J.* **D 19** (2002), 183.

[30] Christen, W.; Krause, T.; Rademann, K. *Rev. Scient. Instrum.* **78** (2007), 073106

[31] Baumfalk, R.; Buck, U.; Frischkorn, C.; Gandhi, S.R.; Lauenstein, C. *Chem. Phys. Lett.* **269** (1997), 321.

[32] Baumfalk, R.; Nahler, N.H.; Buck, U. *Phys. Chem. Chem. Phys.* **3** (2001), 2372.

[33] Fárník, M.; Poterya, V.; Votava, O.;147Ončák, M.; Slavíček, P.; Dauster, I.; Buck, U. *J. Phys. Chem. A* **113** (2009), 7322.

[34] Ashfold, M.N.R.; Cronin, B.; Devin, A.L.; Dixon, R.N.; Nix, M.G.D.; *Science* **312** (2006), 1637.

[35] Van den Brom, A.J.; Kapelios, M.; Kitsopoulos, T.N.; Nahler, N.H.; Cronin, B.; Ashfold, M.N.R. *Phys. Chem. Chem. Phys.* **7** (2005), 892.

[36] Papadakis, V.; Kitsopoulos, T.N. *Rev. Sci. Instrum.* **77** (2006), 083101.

[37] V. Poterya, V. Profant, M. Fárník, P. Slavíček, U. Buck, *J. Chem. Phys.* **127** (2007), 064307.

[38] V. Profant, V. Poterya, M. Fárník, P. Slavíček, U. Buck, *J. Phys. Chem. A* **111** (2007), 12477.

[39] Poterya, V.; Profant, V.; Fárník, M.; Šištík, L.; Slavíček, P.; Buck, U. *J. Phys. Chem.* A **113** (2009), 14583

[40] Rusyniak, M. J.; Ibrahim, Y. M.; Wright, D. L.; Khanna, S. N.; El-Shall, *M. S.* **125** (2003), 12001.

[41] In NIST Mass Spec Data Center, S.E. Stein, director, “Mass Spectra” in NIST 670 Chemistry WebBook, NIST Standard Reference Database Number 69; P.J. Linstrom, W.G. Mallard (Eds.), National Institute of Standards and Technology, Gaithersburg, MD, 20899 (http://webbook.nist.gov), June 2005

[42] Rennie, E. E.; Johnson, C. A. F.; Parker, J. E.; Holland, R. F. D. M. P.; Shaw, D. A. *Chem. Phys.* **250** (1999), 217.

[43] van den Brom, A. J.; Kapelios, M.; Kitsopoulos, T. N.; Nahler, N. H.; Cronin, B.; Ashfold, M. N. R. *Phys. Chem. Chem. Phys.* **7** (2005), 892.

[44] Schwell, M.; Jochims, H.-W.; Baumg¨artel, H.; Leach, S. *Chem. Phys.* **353** (2008), 145.

[45] Lohbrandt, P.; Galonska, R.; Kim, H. J.; Lauenstein, M. S. C.; Buck, U. In *Atomic and Molecular Beams. The State of the Art 2000*; Campargue, R., Ed.; Springer: Berlin, 2001; page 623.

[46] Poterya, V.; Fárník, M.; Buck, U.; Bonhommeau, D.; Halberstadt, N. *Int. J. Mass Spectrom.* **280** (2009), 78.

[47] Sobolewski, A. L.; Domcke, W. *Phys. Chem. Chem. Phys.* **4** (2002), 4.

[48] Sobolewski, A. L.; Domcke, W. *J. Phys. Chem. A* **107** (2003), 1557.

[49] Sobolewski, A. L.; Domcke, W. *Phys. Chem. Chem. Phys.* **7** (2005), 970.

[50] Sobolewski, A. L.; Domcke, W. *J. Chem. Phys.* **122** (2005), 184320.

[51] Sobolewski, A. L.; Domcke, W. *Phys. Chem. Chem. Phys.* **9** (2007), 3818.

[52] Ončák, M.; private communication

[53] Fárník, M.; Nahler, N. H.; Buck, U.; Slavíček, P.; Jungwirth, P. *Chem. Phys.* **315** (2005), 161.

[54] Slavíček, P.; Jungwirth, P.; Lewerenz, M.; Nahler, N. H.; Fárník, M.; Buck, U. *J. Chem. Phys.* **120** (2004), 4498.

[55] Li, Q.; Huber, J.R. *Chem. Phys. Lett.* **345** (2001), 415.

[56] Li, Q.; Carter, R.T.; Huber, J.R. *Chem. Phys. Lett.* **334** (2001), 39.¨

[57] Felder, P.; Yang, X.; Huber, J.R. *Chem. Phys. Lett.* **215** (1993), number 1,2,3.

Appendix A